

**EXPLORING THE INTERACTION BETWEEN FUNCTIONAL  
CARBOHYDRATE POLYMERS AND SMALL-MOLECULE ACTIVE  
COMPOUNDS**

by

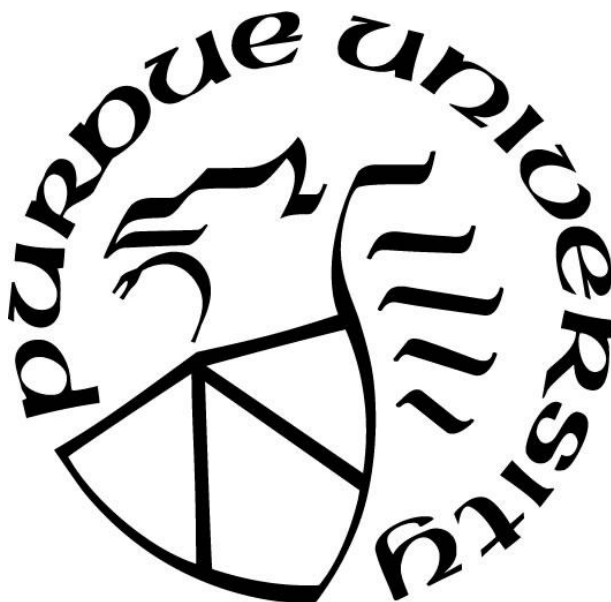
**Jingfan Chen**

**A Dissertation**

*Submitted to the Faculty of Purdue University*

*In Partial Fulfillment of the Requirements for the degree of*

**Doctor of Philosophy**



Department of Food Science

West Lafayette, Indiana

May 2021

**THE PURDUE UNIVERSITY GRADUATE SCHOOL**  
**STATEMENT OF COMMITTEE APPROVAL**

**Dr. Yuan Yao, Chair**

Department of Food Science

**Dr. Arun K. Bhunia**

Department of Food Science

**Dr. Harm HogenEsch**

College of Veterinary Medicine

**Dr. Owen Jones**

Department of Food Science

**Approved by:**

Dr. Arun K. Bhunia

*Dedicated to My Parents*

## ACKNOWLEDGMENTS

I would first like to thank my academic advisor, Dr. Yuan Yao for supporting me along my PHD journey. I joined Dr. Yao's as an undergraduate research assistant in 2013. Since then, I was blessed to have a mentor who is creative, enthusiastic, and thoughtful. His immense knowledge, motivation and patience has inspired me to become an independent researcher. Meanwhile, I also would like to thank Dr. Yao's family, for their caring support throughout the past seven years.

I wish to show my gratitude to Dr. Arun K. Bhunia, Dr. Owen Jones, and Dr. Harm HogenEsch for serving as my committee members even at the hard time, who have been very patient and thoughtful for improving my study and research. I would like to thank Dr. Huaping Mo for his time and guidance in NMR analysis. I am also grateful to have Laurie Mueller and Robert Seiler helping me in obtaining SEM and TEM images. Also, I'd show my gratitude to Dr. Jozef Kokini and Dr. Bruce Copper for their help in fluorescence measurement and HPLC analysis.

I would like to extend my sincere thanks to my labmates. To Dr. Ying Xie, Dr. Xingyun Peng, Dr. Yezhi Fu, Dr. Randol Jose Rodriguez Rosales, Dr. Weili Fan and Miguel A. Alvarez Gonzales, for their time, patience, practical help, and valuable suggestions.

I would especially like to thank the food science department at Purdue University. Without their support and funding, this project could not have reached its goal.

Finally, I would like to recognize the invaluable assistance of my parents. They kept me going on and believing myself. This journey would not have been possible without their input and unconditional love.

# TABLE OF CONTENTS

LIST OF TABLES.....	9
LIST OF FIGURES .....	10
LIST OF ABBREVIATION.....	15
ABSTRACT.....	17
CHAPTER 1. LITERATURE REVIEW .....	19
1.1 Delivery system .....	19
1.1.1 Solid dispersions.....	19
1.1.2 Inclusion complexes .....	20
1.1.3 Particle Size Reduction.....	21
1.1.4 Crystal Modification.....	21
1.1.5 Emulsions .....	22
1.1.6 Characterization of Emulsifier at Oil-water Interface Using Molecular Rotor .....	23
1.2 Phytoglycogen Based Delivery System (Solid Dispersion).....	26
1.2.1 Phytoglycogen .....	26
1.2.2 Review of octenylsuccinate hydroxypropyl phytoglycogen (OHPP).....	27
1.3 Active Ingredients.....	27
1.3.1 Resveratrol.....	28
1.3.2 Griseofulvin.....	29
1.4 Reference .....	31
CHAPTER 2. PHYTOGLYCOGEN TO ENHANCE THE SOLUBLE AMOUNT AND <i>IN-VITRO</i> EFFICIENCY OF RESVERATROL .....	43
2.1 Abstract.....	43
2.2 Introduction.....	43
2.3 Materials and methods .....	45
2.3.1 Materials .....	45
2.3.2 Extraction of phytoglycogen (PG).....	45
2.3.3 Characterization of PG .....	45
2.3.4 Preparation of PG-RES formulations .....	46
2.3.5 Soluble amount of RES .....	47
2.3.6 High performance liquid chromatography (HPLC) quantification of RES.....	47

2.3.7	Phase solubility .....	48
2.3.8	X-ray powder diffraction .....	48
2.3.9	FT-IR .....	48
2.3.10	RES Caco-2 cell monolayer permeation analysis .....	48
2.3.11	Statistical analysis .....	50
2.4	Results and discussion .....	51
2.4.1	Phytoglycogen (PG) Characterization .....	51
2.4.2	Phase solubility of RES enhanced by PG .....	51
2.4.3	Reduction of crystalline structure of RES in PG-RES SD .....	52
2.4.4	Intermolecular Interaction between RES molecule and PG particulate .....	54
2.4.5	Soluble amount of resveratrol (RES) enhanced by phytoglycogen (PG) .....	56
2.4.6	RES Caco-2 cell permeation enhanced by PG .....	58
2.5	Conclusion .....	62
2.6	Reference .....	63
CHAPTER 3. OCTENYLSUCCINATE HYDROXYPROPYL PHYTOGLYCOGEN TO ENHANCE THE SOLUBILITY AND <i>IN-VITRO</i> EFFICACIES OF GRISEOFULVIN .....		69
3.1	Abstract .....	69
3.2	Introduction .....	69
3.3	Materials and Methods .....	70
3.3.1	Chemicals .....	70
3.3.2	Preparation and characterization of octenylsuccinate hydroxypropyl phytoglycogen (OHPP) and Gris-OHPP solid dispersion (SD) .....	70
3.3.3	<i>In-vitro</i> efficacy tests of Gris-OHPP SD (separate the tests) .....	71
3.3.4	Statistical Analysis .....	72
3.4	Results and Discussion .....	72
3.4.1	Characterization of OHPP and Gris-OHPP solid dispersion .....	72
3.4.2	<i>In-vitro</i> efficacies of Gris in Gris-OHPP SD (separate the test) .....	74
3.5	Conclusion .....	76
3.6	Reference .....	77
CHAPTER 4. OCTENYLSUCCINATE HYDROXYPROPYL PHYTOGLYCOGEN (OHPP) TO ENHANCE THE SOLUBILITY AND <i>IN-VITRO</i> EFFICACIES OF RESVERATROL .....		79
4.1	Abstract .....	79
4.2	Introduction .....	79

4.3	Materials and Methods.....	81
4.3.1	Chemicals .....	81
4.3.2	Preparation of hydroxypropyl phytoglycogen (HPP) and octenylsuccinate hydroxypropyl phytoglycogen (OHPP).....	81
4.3.3	Characterization of PG, HPP and OHPP particulates.....	82
4.3.4	Preparation of RES Physical Mixture (PM) and Solid Dispersions (SD) .....	82
4.3.5	Phase solubility of RES in each of HPP and OHPP .....	83
4.3.6	X-ray powder diffraction .....	83
4.3.7	FT-IR .....	84
4.3.8	Soluble RES amount determination.....	84
4.3.9	Dissolution test .....	84
4.3.10	RES Caco-2 cell permeation analysis .....	85
4.3.11	Statistical Analysis .....	86
4.4	Results.....	87
4.4.1	HPP and OHPP characterization .....	87
4.4.2	Phase solubility of RES in each of HPP and OHPP .....	88
4.4.3	Intermolecular Interaction between RES molecule and each of HPP and OHPP particulates.....	90
4.4.4	Crystallinity of RES in RES containing solid dispersions and physical mixtures ....	92
4.4.5	RES soluble amount .....	93
4.4.6	Dissolution test .....	96
4.4.7	Caco-2 permeation of RES .....	97
4.5	Conclusion .....	101
4.6	Reference .....	101
CHAPTER 5. PARTITIONING OF CCVJ IN OIL-WATER TWO-LAYER SYSTEM CONTAINING AMPHIPHILIC BIOPOLYMERS .....		107
5.1	Abstract.....	107
5.2	Introduction.....	107
5.3	Materials and Methods.....	109
5.3.1	Chemicals .....	109
5.3.2	Extraction of PG .....	109
5.3.3	Preparation of Octenylsuccinate Phytoglycogen (PG-OS).....	109
5.3.4	Preparation of Biopolymer Dispersions.....	109

5.3.5	Preparation of Biopolymer-CCVJ Dispersions .....	109
5.3.6	Preparation of Oil-water Two-layer System Containing CCVJ .....	110
5.3.7	Fluorescence Measurement .....	111
5.3.8	Statistical Analysis.....	112
5.4	Results and Discussions.....	112
5.4.1	CCVJ fluorescence emission in oil and aqueous phases .....	112
5.4.2	CCVJ partitioning in oil-water two-layer system.....	114
5.4.3	Impact of biopolymer on the spectra of CCVJ fluorescence emission.....	116
5.4.4	Impact of biopolymer on the spectra of CCVJ fluorescence emission in oil-water two-layer system .....	121
5.5	Conclusion .....	124
5.6	Reference .....	125
CHAPTER 6. MOLECULAR ROTOR IN THE CHARACTERIZATION OF AMPHIPHILIC BIOPOLYMER IN EMULSIONS .....		129
6.1	Abstract.....	129
6.2	Introduction.....	129
6.3	Materials and Methods.....	131
6.3.1	Materials .....	131
6.3.2	Preparation of CCVJ Stock Solution .....	131
6.3.3	Preparation of PBS solution of CCVJ and Oil solution of CCVJ.....	131
6.3.4	Preparation of Biopolymer Dispersions and Emulsions dosed with CCVJ.....	132
6.3.5	Emulsion Particle Size Measurement .....	133
6.3.6	Fluorescence Spectra Scan .....	133
6.3.7	Statistical Analysis.....	133
6.4	Results and Discussions.....	134
6.4.1	Emulsion Particle Size.....	134
6.4.2	CCVJ fluorescence emission in oil and PBS buffer .....	135
6.4.3	CCVJ fluorescence spectra of biopolymer aqueous dispersions .....	136
6.4.4	CCVJ fluorescence spectra of biopolymer emulsions .....	140
6.5	Conclusion .....	145
6.6	Reference .....	145

## LIST OF TABLES

Table 2.1 The stability of RES-containing working solutions in cell-free HBSS media after a 2 h incubation. *	58
Table 2.2 Cell viability results of RES alone and PG-RES (50:1) SD with Caco-2 cells determined using the LDH assay.	59
Table 3.1 The MIC range of Gris against <i>Trichophyton rubrum</i> .	76
Table 4.1 Molecular weight ( $M_w$ , g/mol), particle size ( $R_z$ , nm), $\zeta$ -potential (mV), molecular density ( $\rho$ , g/mol $\cdot$ nm <sup>3</sup> ), and molar substitution (MS) of HP and OS groups of PG, HPP and OHPP <sup>a</sup> .	88
Table 4.2 The stability of RES-containing working dispersions in cell-free HBSS media after a 2-h incubation. *	98
Table 4.3 Cell viability results of OHPP and HPP with Caco-2 cells determined using the LDH assay. *	99
Table 4.4 Cell viability results of RES (0.5% DMSO), OHPP-RES SD, and HPP-RES SD with Caco-2 cells determined using the LDH assay.	99
Table 6.1 Droplet size of OSA-starch (1% w/v), gum Arabic (1% w/v) and sodium caseinate (0.5% w/v) emulsions with different oil concentrations.	134
Table 6.2 Normalized fluorescence intensity measured at $\lambda_{max}$ of OSA-starch (1% w/v), gum arabic (1% w/v) and sodium caseinate (0.5% w/v) emulsions. <sup>a</sup>	144

## LIST OF FIGURES

- Figure 1.1 Basic structure of a cyclodextrin molecule and the mode of complexation with “guest” compounds. A). the chemical structure of a  $\beta$ -cyclodextrin, depicting the eight  $\alpha$ -(1 $\rightarrow$ 4)-linked glucopyranose units (left); schematic representation of  $\beta$ -cyclodextrin (right); B) Schematic of “host–guest” molecular encapsulation, where non-polar “guest” molecule is incorporate into the hydrophobic interior of the cyclodextrin hollow structure.  $\beta$ -CD monomer and dimers can encapsulate one “guest” molecule (noted in light orange)..... 20
- Figure 1.2 Schematic of molecular rotor and its fluorescent emission affected by spatial restriction. The transitions among ground state ( $S_0$ ), locally excited state ( $S_1$ ), and twisted intramolecular charge transfer (TICT) state. In the presence of high spatial restriction, the relaxation from  $S_1$  to  $S_0$  does not go through TICT state, leading to photon emission (left). Micro-environment with low spatial restriction, molecular rotor relaxed through TICT state, resulting in low photon emission intensity (right)..... 24
- Figure 1.3 Schematic of molecular rotor and its fluorescent emission affected by solvent polarity. The transitions among ground state ( $S_0$ ), locally excited state ( $S_1$ ), and twisted intramolecular charge transfer (TICT) state. In polar solvent (right), TICT state with higher energy is stabilized by polar solvents, lessening the energy gap between  $S_0$  and  $S_1$ ..... 25
- Figure 2.1 Transmission electron microscopy (TEM) image of PG (scale bar represents 100 nm) ..... 51
- Figure 2.2 Phase solubility diagram of RES in the presence PG at 25°C. Data are expressed as mean  $\pm$  SD (n = 3)..... 52
- Figure 2.3 X-ray powder diffraction spectra of RES alone, PG, PG-RES (4:1) SD and PG-RES (50:1) SD, and PG:RES (4:1) PM and PG:RES (50:1) PM..... 53
- Figure 2.4 FT-IR spectra of resveratrol (RES alone), phytyglycogen (PG), PG-RES solid dispersions at PG:RES ratios of 4:1 and 50:1 (PG-RES (4:1) SD and PG-RES (50:1) SD), and PG/RES physical mixtures at PG:RES ratios of 4:1 and 50:1 (PG/RES (4:1) PM and PG/RES (50:1) PM). A, B, C and D demonstrate the spectra of 800-4500  $\text{cm}^{-1}$ , 2800-3800  $\text{cm}^{-1}$ , 1280-1430  $\text{cm}^{-1}$ , and 1527-1650  $\text{cm}^{-1}$ , respectively..... 55
- Figure 2.5 Soluble amount of RES in RES alone, PG-RES solid dispersion (SD) and PG:RES physical mixture (PM) at various PG:RES mass ratios (4:1, 10:1, 20:1 and 50:1). Soluble RES amount was determined by dispersing RES-containing solid (RES content 500  $\mu\text{g}$ ) in 1 mL DI water, the supernatant was collected and the soluble amount of RES was determined after centrifugation (16,000  $\times$  g, 5 min.). For each type of formulation, different letters indicate statistical differences ( $p < 0.05$ ) between the mean values of RES soluble amount. Data are expressed as mean  $\pm$  SD (n = 3)..... 56
- Figure 2.6 Cumulative RES permeations across the Caco-2 monolayers of RES alone and PG-RES (50:1) SD at different apical RES loading concentrations over 2-hour incubation. Blue and green lines represented the permeation of loading amount of RES  $C_{\text{RES}} = 15 \mu\text{g/mL}$  (7.5  $\mu\text{g}/\text{well}$  of RES), and 30  $\mu\text{g/mL}$  (15  $\mu\text{g}/\text{well}$  of RES), respectively; red line represents the permeation of loading

amount of RES  $C_{RES}=150 \mu\text{g/mL}$  ( $75 \mu\text{g/well}$  of RES). Solid line represents PG-RES (50:1) SD, and dashed line represents RES alone. Data was expressed as mean  $\pm$  SD ( $n = 3$ )..... 60

Figure 2.7 Schematic of RES alone (left) and PG-RES SD (right) Caco-2 monolayer permeation mechanisms at low RES loading amount (below intrinsic solubility of RES, upper) and high RES loading amount (lower). Only ‘free’ RES molecules (soluble and unbounded RES) can permeate the cell monolayer. After ‘free’ RES is depleted from the donor chamber, the adsorbed RES molecules are desorbed to replenish the depleted ‘free’ RES continuously to achieve a gradual permeation over time ..... 62

Figure 3.1 FT-IR spectra of pure Gris, OHPP, and Gris-OHPP SD. The results were vertically displayed by arbitrary amounts. .... 73

Figure 3.2 Gris solubility after equilibrating at  $25 \text{ }^\circ\text{C}$  for 24 h. Values were represented as the amount of Gris remained soluble after 24 h. Data are expressed as mean  $\pm$  SD ( $n = 3$ ). .... 74

Figure 3.3 Cumulative Gris permeations across the Caco-2 monolayers, with apical loading of Gris total amount of: A)  $m_{gris}=10 \mu\text{g}$  and B)  $m_{gris}=17 \mu\text{g}$ . The ‘Gris Permeation (%)’ was calculated by dividing the amount of Gris in basolateral compartment by the initial amount of Gris in the donor compartment. Data expressed as mean  $\pm$  SD ( $n = 3$ ), significant differences between Gris and Gris-OHPP SD were denoted by different letters ( $p < 0.05$ ). .... 75

Figure 4.1 Transmission electron microscopy (TEM) images of native phytyglycogen (A), hydroxypropyl phytyglycogen (B) and octenylsuccinate hydroxypropyl phytyglycogen (C). The scale bar represented 100 nm. .... 87

Figure 4.2 Phase solubility profiles of RES in the presence of OHPP/HPP in DI water at  $25 \text{ }^\circ\text{C}$  for 24 hours. Data are expressed as mean  $\pm$  standard deviation (SD) ( $n = 3$ ). .... 89

Figure 4.3 FTIR spectra of RES alone, HPP, OHPP and RES-containing formulations. OHPP, solid dispersions of RES with OHPP (OHPP-RES SD), and physical mixtures of RES with OHPP (OHPP/RES PM) were displayed in graph A; HPP, solid dispersion of RES with HPP (HPP-RES SD), and physical mixtures of RES with HPP (HPP/RES PM) were displayed in graph B. RES alone (RES alone) was included in both graphs, denoted as black curve on top..... 91

Figure 4.4 XRD crystallograms of RES alone, OHPP, HPP, solid dispersions of RES with OHPP (OHPP-RES SD), HPP (HPP-RES SD), and physical mixtures of RES with OHPP (OHPP-RES PM), HPP (HPP-RES PM). .... 92

Figure 4.5 Soluble amount of RES in RES alone, OHPP-RES solid dispersion (SD) and physical mixture (PM) at OHPP:RES ratio of 4:1, HPP-RES SD solid dispersion (SD) and physical mixture (PM) at HPP:RES ratio of 4:1. The instant soluble RES amount (on the left) was determined by dispersing RES-containing samples in 1 mL DI water (RES content:  $2500 \mu\text{g/mL}$ ), the supernatant was collected after centrifugation ( $16,000 \times g$ , 5 min). All experiments were carried out at room temperature and performed in triplicates. Data are expressed as mean  $\pm$  SD ( $n = 3$ )..... 94

Figure 4.6 Dissolution profiles of RES alone, OHPP-RES SD and HPP-RES SD. Accurately weighed RES-containing solids (RES content of 50 mg) were dispersed into 500 mL phosphate buffer (pH 6.8, 58 mM), and stirred with rotating paddles at 100 rpm ( $37 \text{ }^\circ\text{C}$ ). 1 mL aliquot was collected at pre-determined time points to determine the soluble amount of RES. Data are expressed as mean  $\pm$  SD ( $n = 3$ )..... 96

Figure 4.7 Cumulative RES permeations across the Caco-2 monolayers of RES (0.5% DMSO), OHPP-RES SD, or HPP-RES SD at different apical RES loading concentrations over 2-hour incubation. Red, green, and black lines represented the permeation of OHPP-RES SD, HPP-RES SD, and RES (0.5% DMSO), respectively. Solid, and dotted lines represented the permeation of loading amount of RES  $C_{RES}=30 \mu\text{g/mL}$  (15  $\mu\text{g/well}$  of RES), and RES  $C_{RES}=15 \mu\text{g/mL}$  (7.5  $\mu\text{g/well}$  of RES), respectively. Data was expressed as mean  $\pm$  SD (n = 3). ..... 100

Figure 5.1 Schematic showing the preparation of CCVJ containing oil-water two-layer systems. Oil phase was on the top of the aqueous layer. For the first group (CCVJ delivered from the oil phase), the final concentration of CCVJ in working CCVJ oil solution on top (42 mg) was 21.88  $\mu\text{M}$  (0.268  $\mu\text{g/well}$ ) in oil. For the second group (CCVJ delivered from the oil phase), the final concentration of CCVJ in working CCVJ PBS solution was 5  $\mu\text{M}$  (0.268  $\mu\text{g/well}$ ) in PBS. .... 111

Figure 5.2 The observed fluorescence emission spectra of CCVJ at concentrations from 2.5 to 15  $\mu\text{M}$  in oil (A) and PBS (B) are shown. The embedded graph in B shows the OFE intensity of CCVJ in PBS at CCVJ concentration of 2.5, 5, 10, and 15  $\mu\text{M}$ , and the fitted curves were shown in dotted lines. .... 113

Figure 5.3 The change of observed fluorescence emission spectra of CCVJ in the oil-water two-layer system over 24 h. CCVJ was delivered from PBS (A<sub>1,2,3,4</sub>) or oil (B<sub>1,2,3,4</sub>) to the two-layer system (the total amount of CCVJ delivered to the system were the same in both delivery approaches). In the group that CCVJ was delivered from PBS, the concentrations of CCVJ in the aqueous phase for A<sub>1</sub>, A<sub>2</sub>, A<sub>3</sub>, and A<sub>4</sub> were 2.5 (0.134  $\mu\text{g/well}$ ), 5 (0.268  $\mu\text{g/well}$ ), 10 (0.537  $\mu\text{g/well}$ ), and 15  $\mu\text{M}$  (0.537  $\mu\text{g/well}$ ), respectively. In the group that CCVJ was delivered from oil, the concentrations of CCVJ in the oil phase for B<sub>1</sub>, B<sub>2</sub>, B<sub>3</sub>, and B<sub>4</sub> were 10.94 (0.134  $\mu\text{g/well}$ ), 21.88 (0.268  $\mu\text{g/well}$ ), 43.76 (0.537  $\mu\text{g/well}$ ) and 65.64  $\mu\text{M}$  (0.537  $\mu\text{g/well}$ ), respectively. .... 115

Figure 5.4 The observed fluorescence emission spectra of CCVJ in OSA-starch, PG-OS, gum arabic, and sodium caseinate aqueous dispersions. For each biopolymer, only emission spectra within detectable emission intensity range are displayed in the figure. In each group, from bottom to top, the concentrations of biopolymer were: (1) 1.25, 2.5, 3.75, 5, 10, and 20 mg/mL for OSA-starch, (2) 1.25, 2.5, 3.75, 5, 10, and 20 mg/mL for PG-OS, (3) 1.25, 2.5, 3.75, 5, 10, 20, and 50 mg/mL for gum arabic, and (4) 1.25, and 2.5 mg/mL for sodium caseinate. The red-shaded area indicates the change of the peak maximum ( $\lambda_{em \max}$ ), with its value provided at the bottom of graph for each biopolymer. .... 117

Figure 5.5 The emission intensity (OFEs were obtained at  $\lambda_{em \max}$  of biopolymer dispersions) as a function of biopolymer concentration (mg/mL) in aqueous dispersion. For each biopolymer, the concentrations of ranges were: (1) 1.25~ 20 mg/mL for OSA-starch and PG-OS; (2) 1.25~ 50 mg/mL for gum arabic, and (3) 1.25~ 2.5 mg/mL for sodium caseinate. The embedded figure showed the observed fluorescence emission intensity (OFE were obtained at  $\lambda_{em \max}=494 \text{ nm}$  for OSA-starch, PG-OS and gum arabic dispersions, and  $\lambda_{em \max}=488 \text{ nm}$  for sodium caseinate dispersions) at biopolymer concentration of 0~5.0 mg/mL, and the fitted curves were shown in dotted lines. .... 118

Figure 5.6 Wavelength of emission peak location ( $\lambda_{em \max}$ ) as a function of biopolymer concentration (mg/mL) in aqueous dispersion. For each biopolymer, the concentrations of ranges were: (1) 1.25~ 20 mg/mL for OSA-starch and PG-OS; (2) 1.25~ 50 mg/mL for gum arabic, and (3) 1.25~ 2.5 mg/mL for sodium caseinate. .... 120

Figure 5.7 The observed fluorescence emission (OFE) spectra ( $\lambda_{\text{ex}} = 420 \text{ nm}$ ,  $\lambda_{\text{em}} = 450 \sim 650 \text{ nm}$ ) of CCVJ in oil-water two-layer system in the presence of biopolymers with concentration ranges of 2.5 ~ 5 mg/mL for OSA-starch, PG-OS, gum arabic, and sodium caseinate. The schematic on top showed the experiment setup which was composed of oil phase (on top) and aqueous phase with biopolymer (on the bottom). Two experimental conditions were tested: 1) CCVJ was delivered from water phase (left column), and 2) CCVJ was delivered from oil phase (middle column). Emission spectra of 0.5-h stabilization (dashed lines), and 24-h stabilization (solid lines) were recorded. Red shaded area indicated that the fluorescence was observed as emission intensity over a band of wavelengths instead of a peak..... 123

Figure 6.1 Schematic diagram showing the preparation of CCVJ containing aqueous and oil controls, biopolymer working dispersions, and emulsions. .... 132

Figure 6.2 The observed fluorescence emission spectra of CCVJ at concentrations of 5  $\mu\text{M}$  in oil (A) and PBS (B) are shown. Each well of 96 plate contained 100  $\mu\text{L}$  of oil or PBS. .... 135

Figure 6.3 The observed fluorescence emission spectra of CCVJ in OSA-starch, gum arabic, and sodium caseinate aqueous dispersions. For each biopolymer, only emission spectra within detectable emission intensity range are displayed in the figure. In each group, from bottom to top, the concentrations of biopolymer were: (1) 1.25, 2.5, 3.75, 5, 10, 20, and 50 mg/mL for OSA-starch, (2) 1.25, 2.5, 3.75, 5, 10, 20, 50, and 100 mg/mL for gum arabic, and (3) 1.25, 2.5, 3.75, 5, and 10 mg/mL for sodium caseinate. Arrow indicates the direction of increasing concentration of biopolymer. The red shaded area/line indicates the change of the peak maximum ( $\lambda_{\text{max}}$ ), with its value provided at the bottom of graph for each biopolymer..... 137

Figure 6.4 The observed emission intensity (OFEs were obtained at  $\lambda_{\text{max}}$  of each biopolymer) as a function of biopolymer concentration (mg/mL) in aqueous dispersion. For each biopolymer, the concentrations of ranges were: (1) 1.25~ 50 mg/mL for OSA-starch; (2) 1.25~ 100 mg/mL for gum arabic, and (3) 1.25~ 10 mg/mL for sodium caseinate. The embedded figure displayed the observed fluorescence emission intensity (OFE were obtained at  $\lambda_{\text{max}} = 494 \text{ nm}$  for OSA-starch, and gum arabic dispersions, and  $\lambda_{\text{max}} = 488 \text{ nm}$  for sodium caseinate dispersions) at biopolymer concentration of 0~5.0 mg/mL, and the fitted curves were shown in dotted lines. .... 138

Figure 6.5 Wavelength of emission peak location ( $\lambda_{\text{max}}$ ) as a function of biopolymer concentration (mg/mL) in aqueous dispersion. For each biopolymer dispersion, the concentrations of ranges were: (1) 1.25~ 50 mg/mL for OSA-starch; (2) 1.25~ 100 mg/mL for gum arabic, and (3) 1.25~ 10 mg/mL for sodium caseinate..... 139

Figure 6.6 Fluorescence emission spectra of: A. gum arabic, B. sodium caseinate, and C. OSA-starch aqueous dispersions and their corresponding emulsions at oil-to-polymer ratios of 1:2, and 1:1. Emission spectra were shown in solid lines, polymer aqueous dispersion (dotted lines), and high pressure homogenization (HPH) processed polymer aqueous dispersion (dashed lines).  $\lambda_{\text{max}}$  of polymers dispersions and their corresponding emulsions were highlighted in red dashed lines. Spectra are measured in triplicates. The impact of oil-to-polymer ratio on the fluorescence emission peak ( $\lambda_{\text{max}}$ ) of emulsion were shown in the embedded table in each graph. .... 141

Figure 6.7 The impact of oil concentration on oil-water interface-adsorbed biopolymer/total biopolymer ratio (AP%) in emulsions. Biopolymer adsorption percentage (AP%) was calculated as:  $\text{AP} (\%) = \frac{\text{interface adsorbed biopolymer}}{\text{total biopolymer}}$ . Blue tail represented the

hydrophobic region and the dark red circle represented the hydrophilic region of the biopolymer.  
..... 143

## LIST OF ABBREVIATION

ACN	acetonitrile
AI	active ingredient
API	active pharmaceutical ingredient
BSC	Biopharmaceutical Classification System $\beta$ -cyclodextrin
$\beta$ -CD	$\beta$ -cyclodextrin
CD	cyclodextrin
D <sub>2</sub> O	deuterium oxide
DCM	dichloromethane
DI	deionized
DMSO	dimethyl sulfoxide
DMEM	Dulbecco's Modified Eagle's Medium
DS	degree of substitution
FBS	Fetal Bovine Serum
FTIR	Fourier Transform-Infrared gastrointestinal
GI	gastrointestinal
Gris	griseofulvin
<sup>1</sup> H NMR	proton nuclear magnetic resonance
HBSS	Hank's Balanced Salt Solution
HP	hydroxypropyl
HPLC	high performance liquid chromatography
HPMC	hydroxypropylmethylcellulose
HPMCAS	hydroxypropylmethylcellulose Acetate Succinate
HPP	hydroxypropyl phytoglycogen
HPSEC	High Performance Size Exclusion Chromatography
LDH	Lactic Acid Dehydrogenase
MALLs	multi-angle laser-light scattering detector
MIC	minimum inhibitory concentration
MS	molar substitution

Mw	molecular weight
MWCO	molecular weight cut-off
RES	resveratrol
XRD	X-ray diffraction
OHPP	octenylsuccinate hydroxypropyl phytoglycogen
OS	octenylsuccinate
PG	phytoglycogen
PG-OS	phytoglycogen octenylsuccinate
SD	solid dispersion
su 1	sugary-1
TEER	Transepithelial electrical resistance

## ABSTRACT

Naturally occurring carbohydrates polymers and their functional derivatives play important roles in the research and technology development in the food, nutrition, and pharmaceutical areas. A major property of these polymeric materials is to associate, enable, enhance, and/or deliver small-molecule active compound such as phytochemicals, nutraceuticals, and active pharmaceutical ingredients (APIs). The goal of this project was to synthesize and characterize phytoglycogen-based materials and study their structure-function relationships in association with selected small-molecule active compounds, including resveratrol, a food-related poorly water-soluble phenolic compound, griseofulvin, an insoluble API, and CCVJ (9-(2-carboxy-2-cyanovinyl) julolidine) a molecular rotor used as a structural probe of polymeric materials.

In this study, phytoglycogen (PG) was derivatives to phytoglycogen octenyl succinate (PG-OS), hydroxypropyl phytoglycogen (HPP), and octenylsuccinate hydroxypropyl phytoglycogen (OHPP). PG, HPP, and OHPP were evaluated for their efficacy in improving the solubility and Caco-2 permeation of resveratrol and griseofulvin, and using CCVJ, PG-OS was evaluated on its performance at oil-water interface in comparison with OSA-starch, acacia gum, and sodium caseinate. The results showed that: 1) PG, HPP, and OHPP substantially improved the soluble amount and Caco-2 monolayer permeation of resveratrol and griseofulvin, and anti-fungal efficacy of griseofulvin in the aqueous system were significantly enhanced; suggesting that the active ingredients were effective solubilized and released to become bioavailable, 2) among all PG-based biopolymers, OHPP showed superior performance in solubilizing resveratrol and griseofulvin, and 3) in the oil-water two-layer model system, PG-OS, OSA-starch, acacia gum, and sodium caseinate all affected the transferring of CCVJ from oil to aqueous phase, and the effect was monitored and interpreted by the emission spectra of molecular rotor; in the emulsion system, the emission peak wavelength of CCVJ was correlated with the amount of biopolymer adsorbed at the interface of emulsion droplets, and the molecular rotor-based method can be used to characterize the interfacial adsorption of biopolymer at the interface in oil-in-water emulsion.

This study provides information on the interactions between phytoglycogen-based biopolymers and poorly water-soluble active ingredients, and may potentially supports the study of new functional ingredients interaction with phytoglycogen-based biopolymers in aqueous

system. Furthermore, this work allowed us to advance the use of molecular rotor as new analytical tool to study the physicochemical properties of biopolymer.

## CHAPTER 1. LITERATURE REVIEW

### 1.1 Delivery system

#### 1.1.1 Solid dispersions

Solid dispersion is a hydrophilic carrier-drugs complex/mixture, where drug molecules are dispersed in a polymer matrix. Solid dispersion is one of the major advancement to increase dissolution rate and bioavailability of poorly water-soluble drugs, such as, Biopharmaceutical Classification System (BCS) class II and class IV drugs, where their solubility and dissolution rate are the major obstacle in drug formulation.

The mechanisms for solid dispersion technology to improve drug aqueous solubility and bioavailability includes, 1) reducing drug solids into fine particles for enlarged surface area, which accelerated the drug dissolution rate (Chiou & Riegelman, 1969); 2) breaking drug crystal lattice to generate amorphous particles, which enhanced the drug wettability (Habib, 2000); 3) increase drug porosity to provide high surface and volume properties, which facilitated the drug release (Jiang et al., 2019).

Methods to prepare solid dispersions include:

1) hot-melt extrusion, a solvent free process, is principally used for drugs that have lower melting point. In this preparation, dispersion consisted of polymer carrier and drug was melted (above glass transition temperature) and extruded to realize effect mixing at molecular level;

2) spray-drying, one-step process to generate fine powders, is an economical processing method that is heavily used in formulating small molecule drugs. The process was initiated by atomizing suspension into tiny droplets followed by a drying process;

3) lyophilization (freeze-drying), a low temperature method, is often reserved for materials that are heat-sensitive. The solution that contains both drug and carrier was frozen and vacuumed, followed with sublimation to obtain a lyophilized molecular dispersion (Wang., 2000);

4) co-grinding, an easy and economical approach, achieves amorphization of drug by milling it with polymer (e.g. indomethacin and polyvinylpyrrolidone or silica) (Bahl et al., 2006);

5) Supercritical fluid process facilitates the formulation of solvent-free, thermal labile and easily oxidized drugs into micron-size solid dispersions for their enhancement solubility. In this

preparation, a solution of drug and carrier (e.g. carotenoids/lutein and poly-ethylene glycol (PEG) in DCM) was expanded with supercritical CO<sub>2</sub> to produce solid particles (Martín et al., 2007).

Solid dispersions in water usually undergo rapid drug re-crystallization and precipitation. For these reasons, other formulation techniques have been proposed as alternatives to solid dispersion.

### 1.1.2 Inclusion complexes

Inclusion complexation is prepared by inserting drug molecules (usually non-polar, known as “guest”) into the hydrophobic cavity of “host” molecule (e.g. cyclodextrin).

“Host-Guest” inclusion complexes interactions are stabilized by non-covalent interactions. One of the representative “host” molecules is cyclodextrin ( $\alpha$ -CD,  $\beta$ -CD,  $\gamma$ -CD), which is well-known for its inclusion complexation capacity.

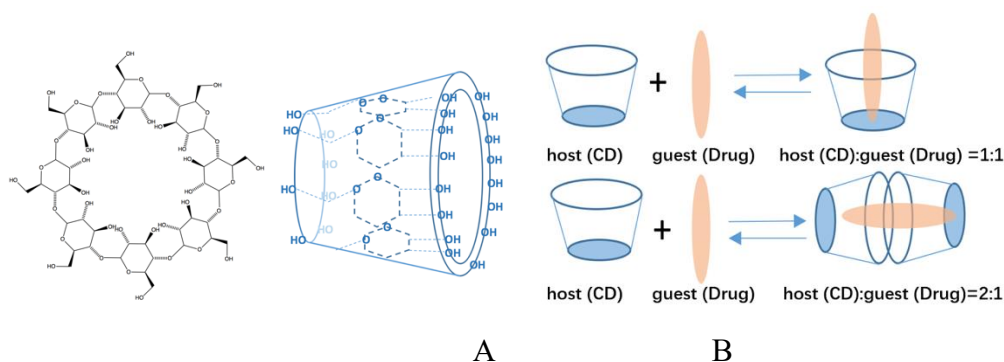


Figure 1.1 Basic structure of a cyclodextrin molecule and the mode of complexation with “guest” compounds. A). the chemical structure of a  $\beta$ -cyclodextrin, depicting the eight  $\alpha$ -(1 $\rightarrow$ 4)-linked glucopyranose units (left); schematic representation of  $\beta$ -cyclodextrin (right); B) Schematic of “host–guest” molecular encapsulation, where non-polar “guest” molecule is incorporate into the hydrophobic interior of the cyclodextrin hollow structure.  $\beta$ -CD monomer and dimers can encapsulate one “guest” molecule (noted in light orange).

Cyclodextrin (CD) was produced from starch by the enzymatic conversion. The hollow structure of CD is composed of six, seven and eight numbers of glucopyranose units respectively, that form ring structures with a hydrophobic internal cavity and a hydrophilic external region (Santos et al., 2019). Hydrophobic “guest” molecules (e.g. polyphenols, protein, amino acids) are commonly encapsulated by the cyclodextrin ring.

Three naturally occurring CD are  $\alpha$ ,  $\beta$  and  $\gamma$ -cyclodextrin. Among which,  $\beta$ -cyclodextrin is most economical and widely used, even though it's the least soluble in aqueous.  $\alpha$ -cyclodextrin forms complexes with few, small size molecules due to its small cavity size. In contrast,  $\gamma$ -cyclodextrin has the largest cavity that allows complexation with large size molecules.

Methods used to prepare solid inclusion complexes include co-precipitation, neutralization precipitation, milling, co-grinding, spray drying, freeze-drying and microwave irradiation (Badr-Eldin et al., 2013).

The limitations of CD are associated with its high dose required for parenteral administration, toxicity at high concentration, prolonged process, limited loading capacity, poor lipophilic membrane permeation, and delayed-release (Mognetti et al., 2012).

### **1.1.3 Particle Size Reduction**

Particle size reduction of drug particles is a promising approach to increase the dissolution rate of drug. Technically, reduction of particle size does not affect intrinsic solubility of drug. Instead, such processing method increases the surface area of drug particles with enhanced dissolution profile. Higher dissolving rate generates higher concentration gradient between intestinal lumen and systemic circulation, which promotes drug permeation and bioavailability (Wu & Sarsfield, 2018).

Traditional methods to reduce size of drug particles include jet mill, grinding, ball mill, high pressure homogenization, spray-drying, freeze-drying, etc. Recent findings show that the rapid expansion of supercritical solutions produced particles in submicron size (Pessi et al., 2016; Tuerk & Bolten., 2016); sonocrystallization control the particle size and distribution through triggering nucleation at a low supersaturation using ultrasound (Gielen, 2017; Yang et al., 2018). Major limitation associated with particle size reduction is the potential chemical degradation of drugs caused by the thermal and physical stress.

### **1.1.4 Crystal Modification**

Controlling drug crystals or spherical crystal agglomeration is important in pre-formulation study. Crystal habits (external structure of crystals) and polymorphic states (internal structure of crystals) of drug crystals have a great influence on the cohesive interactions, physical stability, and

mechanical properties (compaction, flowability, and packing) of dosage forms. Many factors are known to influence the crystal forms, for example, solutes saturation state, rate of cooling, temperature of crystallization solvent, and presence of ions (Tiwary, 2001). It has been reported cyclodextrins can be used as additives for controlling drug crystallization (Iohara et al., 2019). Polymorphism is known to convert unstable polymorphs to stable forms that possess different melting point and solubility (Porter et al., 2008).

### 1.1.5 Emulsions

Emulsion is an ideal delivery systems for encapsulating water insoluble and easily degraded/metabolized bioactive compounds (*e.g.* carotenoids, tocopherol,  $\omega$ -3 fatty acids, orange oil, and polyphenols). In food and pharmaceutical industries, sensitive, lipophilic bioactive compounds and insoluble drugs dissolved in the oil phase are protected and delivered by the interfacial layer of emulsifiers (McClements et al., 2007).

Emulsifiers, biopolymers or synthetic polymers, facilitate the formation and stabilization of emulsion droplets by reducing the interfacial tension (McClements, 2007). Their interfacial behaviors (*e.g.* diffusion/adsorption, rearrangement and aggregation at the interface, etc.), and the number of emulsifiers adsorbed at interface have significant influence on emulsion properties and stability. However, emulsifier interfacial behavior can be quite different. Such differences are attributed to their distinct structural properties. Therefore, it is of great importance to explore and characterize emulsifier structure and interfacial behavior in emulsion (Cabezas et al., 2019).

Various analytical techniques and methodologies that have been developed to characterize emulsifier in emulsions. Traditional methods, such as, particle size analysis, interfacial rheology measurement, gravitational separation, opacity measurement, etc. have been predominately used for the characterization of emulsions. Various limitations are associated with these methods, for example, emulsion disruption, lacking structure or interfacial behavior characterization, applicable to limited number of emulsifiers, time consuming (Wilde et al., 2004; Dickinson., 1998). Over the past few decades, fluorescence spectroscopy has been extensively used as a non-invasive and non-disruptive technique to study the oil-water interface performance of surfactants. Prior work showed that fluorescence was used to evaluate lecithin effects on egg yolk granular aggregation thus affecting granular protein emulsifying properties (Ohtsuru & Kito,1983). It was reported that the interaction between polarity-sensitive fluorescent dyes (*e.g.* pyrene fluorescent probe) and

emulsifiers can be used to determine critical micelle concentration (Mohr et al., 2007; Zhang et al., 1996). Further study showed that fluorescence spectrophotometer/ spectroscopy can be utilized to monitor surfactant at oil-water interface at molecule structure level by analyzing emission of fluorophore (*e.g.* tryptophan) residues in emulsifier. However, these studies were only applicable to protein surfactants (Shen et al., 2020; Miriani et al., 2012). High-performance thin-layer chromatography with fluorescence detection (HPTLC-FLD) allowed the characterization and analysis of the composition of emulsifier directly, however, failed to detect interfacial behaviors and structure changes (Oellig et al., 2020).

### **1.1.6 Characterization of Emulsifier at Oil-water Interface Using Molecular Rotor**

#### ***Molecular rotor***

Molecular rotors are utilized as non-disruptive, non-invasive, and highly sensitive approach to measure fluid viscosity and environmental polarity. Molecular rotor is strongly affected by its micro-environment. It's composed by a group of fluorophores that react to change in local spatial restriction (confinement restriction) with emission intensity change, and to change in solvent polarity with red/blue peak shift (Akers & Haidekker, 2004).

Among various molecular rotors, CCVJ (9-(2-carboxy-2-cyanovinyl)-julolidine) is particularly appealing because it's sensitivity to solvent polarity and spatial restriction, which can be interpreted by fluorescence emission  $\lambda_{\max}$  and intensity in spectra, respectively (Akers & Haidekker, 2004). CCVJ was synthesized in 1992, its hydrophilicity made it suitable for research associated with aqueous system (Sawada et al., 1992).

CCVJ is most widely used to study: 1) supramolecular (*e.g.* starches, polysaccharides, proteins), for example, characterizing polysorbate-containing IgG formulations, examining dynamic structures of antigen-antibody interactions, probing starch colloidal solution and gelation, 2) real-time phospholipids formation and movement, 3) *in-situ* polymerization processes, and other biopolymers (Akers & Haidekker, 2004; Mustafic et al., 2010; Haidekker et al., 2001; Lai et al., 2015; Hawe et al., 2010; Yu et al., 2016).

### ***Molecular rotor micro-viscosity sensitivity***

The use of fluorescent molecular rotors enabled the characterization of the micro-environment viscosity.

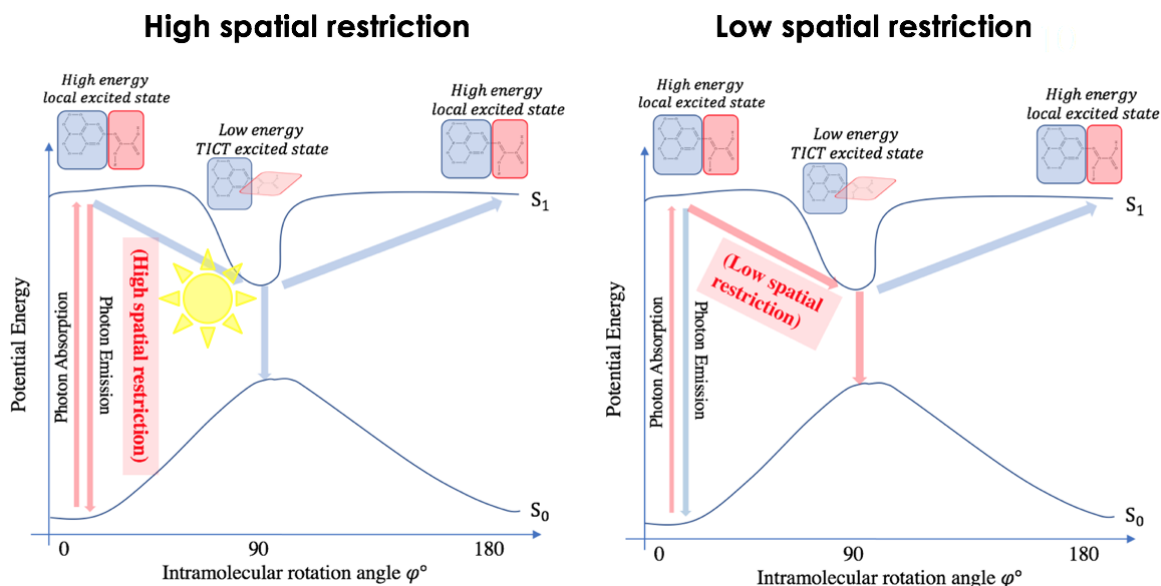


Figure 1.2 The effect of spatial restriction on the fluorescent emission of molecular rotor. The schematic shows the transitions among ground state ( $S_0$ ), locally excited state ( $S_1$ ), and twisted intramolecular charge transfer (TICT) state. In low spatial restricted micro-environment, molecular rotor relaxed through TICT state, resulting in low photon emission intensity (right). In high spatial restricted micro-environment, the relaxation from  $S_1$  to  $S_0$  does not go through TICT state, leading to photon emission (left).

CCVJ is sensitive to local spatial restriction of its microenvironment (Haidekker et al., 2005). Under high spatial restriction, the inhibition of CCVJ intramolecular rotation leads to an increase in fluorescence intensity, whereas under low or no spatial restriction, CCVJ undergoes relaxation through TICT state without photon emission. Therefore, the emission intensity can be used to monitor the local spatial restriction of CCVJ micro-environment.

### ***Molecular rotor polarity sensitivity***

The use of fluorescent molecular rotors enabled the characterization of the polarity of the environment.

CCVJ was found to be sensitive to the polarity of the environment (Hawe et al., 2010; Haidekker et al., 2005). As shown in Figure 1.3, CCVJ's transition from ground state to excited state generates a dipole moment, the energy expended for polar solvent molecule to re-align themselves with the dipole moment between  $S_0$  and  $S_1$  state, will lead to a red-shift (lower energy state) of emission peak. Hence, the emission peak shift can be used to identify the local polarity of CCVJ microenvironment (cell membrane, emulsion, etc.) (Yang et al., 2014).

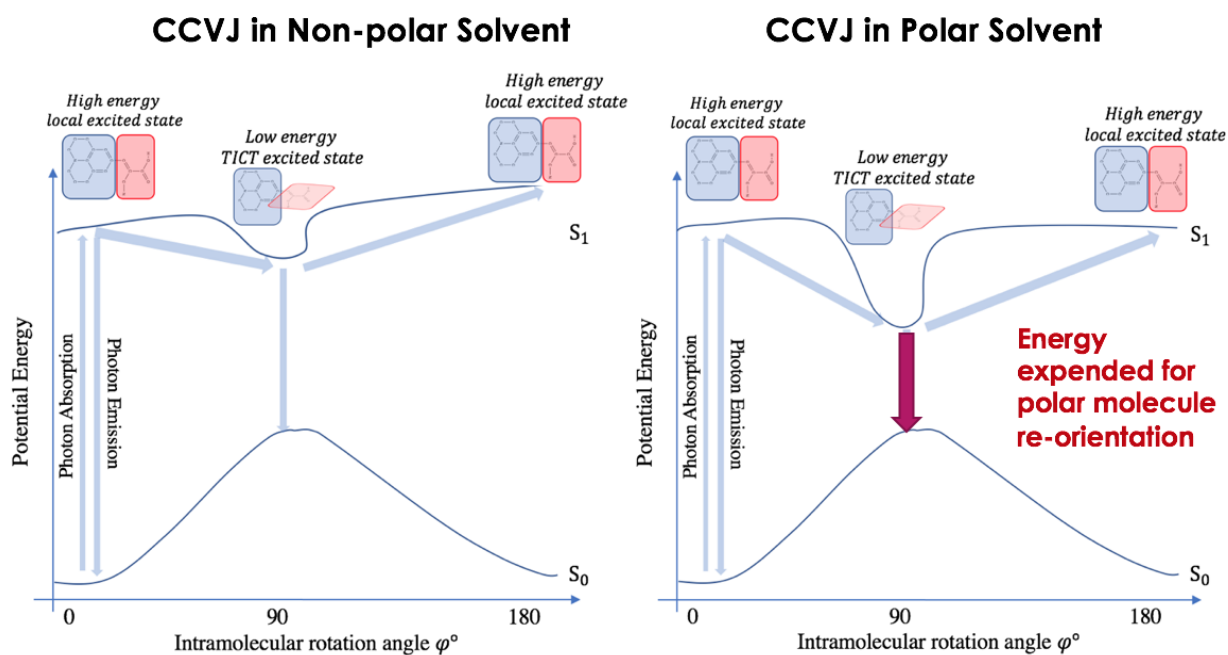


Figure 1.3 The effect of solvent polarity on the fluorescent emission of molecular rotor. The schematic shows the transitions among ground state ( $S_0$ ), locally excited state ( $S_1$ ), and twisted intramolecular charge transfer (TICT) state. In polar solvent (right), TICT state with higher energy is stabilized by polar solvents, lessening the energy gap between  $S_0$  and  $S_1$ .

### ***Characterization of emulsion and interface using molecular rotor***

Molecular rotor can be utilized as probe for interface in biological system. Molecular rotor's exposure to various degree polarity of solvents and molecule aggregate will change the fluorescence emission spectra.

It was reported that CCVJ lipophilized derivatives (CCVJ-C12 and CCVJ-Chol) have been utilized as probe to monitor their rotation at air–water interface (Mori et al., 2018). Furthermore, study showed that it was possible to use molecular rotor as a promising non-invasive approach to monitor the kinetics of mini-emulsion polymerization reaction *in situ* at oil-water interface

(Frochot et al., 2011; Bracco et al., 2017) properly engineered molecular rotor (p-phenylene rotor) in the walls of porous structure to achieve modulation of CO<sub>2</sub> dynamics at gas–solid interfaces in porous material, which provided a platform to mimic CO<sub>2</sub> involved chemical and biological processes. However, the results from both studies were not representative and the application of molecular rotor was limited as complex chemical modification and special engineering of molecular rotor were required to locate the rotor at the interface.

Dent et al. (2015) demonstrated that fluorescence probe BODIPY was found to display preferential partitioning into liquid-disordered L<sub>d</sub> phase instead of liquid-ordered L<sub>o</sub> phase in lipid membrane. The partitioning between different phases can be interpreted from fluorescence emission intensity and peak wavelength. Characterization of molecular rotor partitioning preferences, trajectories or migration path within a complex system improve the understanding and application of molecular rotor.

## **1.2 Phytoglycogen Based Delivery System (Solid Dispersion)**

### **1.2.1 Phytoglycogen**

Dendrimer particles are emerging polymers that are known for their highly-branched structure and multifunctionality. Over the past 20 years, dendrimer particles have shown promising capacity for the delivery of gene, hydrophobic active ingredients, development of vaccines, antibacterial and anticancer therapies (Gillies & Frechet, 2005). Among various dendrimers, phytoglycogen (PG) has gained much attention in food industry. PG is extracted from the kernel of maize mutant *sugary-1 (su 1)*. The deficiency of an isoamylase-type debranching enzyme in the mutant strain reduced the trimming of glucan chains, which resulted in highly branched PG (Wattebled et al., 2005). PG has been considered as great delivery agent for active ingredients due to its all natural, highly branched, glucan structure with an increasing molecular density toward outer layers. Active ingredient molecules are physically entrapped within the branched structure through non-covalent interactions. Moreover, numerous reactive surface ending groups allowed for particle functionalization through chemical modifications.

It was reported that PG has shown its superior performance in the delivery of many water insoluble polyphenols, such as, curcumin, quercetin and lutein (Rodriguez-Rosales & Yao, 2020; Chen and Yao, 2017b, Chen and Yao, 2017a). The non-covalent interaction between polyphenol molecules and functional groups at the branches encouraged the incorporation and dispersion of

active ingredient in aqueous system. Meanwhile, the highly-branched glucan chains inhibited the dissociation and recrystallization of polyphenol molecules through steric hindrance, which facilitated the maintenance of supersaturated state of polyphenols.

Our lab has been leading the research on the functionalization of PG nanoparticles for its food and pharmaceutical application. Scheffler et al. (2010a) reported phytyglycogen octenylsuccinate (PG-OS), generated by esterification of PG with octenylsuccinic anhydride (OSA), was prepared as surfactant for the formation and stabilization of fish oil emulsion, and the delivery of antimicrobial agents nisin and  $\epsilon$ -polylysine (EPL) (Scheffler et al., 2010b; Bi et al., 2011a; Bi et al., 2011b; Bi et al., 2016). Later work explored the potential of PG derivatives application in pharmaceutical industry, PG-OS was further reacted with (3-chloro-2-hydroxypropyl)-trimethylammonium chloride (CHPTAC) to form cationic nanoparticle PG-OS-CHPTAC, which is utilized as effective adjuvant (Lu et al., 2015).

### **1.2.2 Review of octenylsuccinate hydroxypropyl phytyglycogen (OHPP)**

OHPP, as a highly potent new solubilizer, was used to improve solubility and bioavailability of many poorly water soluble active ingredients, such as, celecoxib, griseofulvin, docetaxel, fenofibrate, curcumin, niclosamide and paclitaxel, by 39 to over 14000 times (Xie & Yao, 2018; Xie & Yao, 2018a; Xie & Yao, 2018b; Xie & Yao, 2019).

OHPP is an amphiphilic particulate prepared by grafting phytyglycogen (PG) with hydroxypropyl group and octenylsuccinate (OS) group (Xie & Yao, 2018b). Functional groups hydroxypropyl and octenylsuccinate substituted at the surface of PG particulate incorporate pharmaceutical ingredients in the solid dispersion form through hydrogen bonds and hydrophobic interactions (Xie & Yao, 2018b). The results showed that OHPP associated active ingredients were amorphinized and showed enhanced solubility, dissolution rate and bioavailability (Xie & Yao, 2018a; Xie & Yao, 2018b; Xie & Yao, 2019).

### **1.3 Active Ingredients**

Nutraceuticals are food-containing nutrients that provide therapeutic benefits, including the prevention and treatment of disease (Nasri et al., 2014, Defelice, 1995). Recent research have

shown promising clinical outcomes of nutraceuticals in the treatment of diabetes, cancers, cardiovascular disease, cancers, etc. (Nasri et al., 2014).

Among numerous nutraceuticals, polyphenols, secondary metabolites of plants, are of particular importance due to their roles as nutrients, anti-inflammatory, antioxidant, anti-protozoal, anti-mutagenic and anti-cancer properties. Some common polyphenols include quercetin, curcumin, lutein, resveratrol, rutin, and etc.

The market of nutraceuticals has expanded and reached \$250 billion by 2018 (Hardy., 2000), among which the global market of polyphenol was valued at \$1.8 billion. The market was anticipated to be driven by the significant growth of global functional food and beverages industry, and the rising awareness of all natural ingredients.

However, there have been considerable challenges in the clinical application of polyphenols, which are mostly associated with their poor target delivery, inconsistent controlled release and high susceptibility to physical and chemical.

### **1.3.1 Resveratrol**

Resveratrol (RES) is a naturally-occurring dietary polyphenol, which has received much attention for its nutritional benefits and potential preventive actions in human disease (Espinoza et al., 2019; Chatterjee et al., 2019; Fraga et al., 2019). Red grapes and wines are the most commonly consumed food products that contain high RES content.

Renaud and De Lorgeril were the first to relate regular moderate wine consumption to the potential health benefits (“French Paradox”), such as, protective effects against coronary heart disease (Renaud & de Lorgeril,1992). In pharmaceutical industry, RES has been suggested to possess many therapeutic effects, including anti-inflammatory, anti-cancer, neuroprotective, cardio-protective, and hepatoprotective effects (De La Lastra & Villegas, 2007; Zhang et al., 2010; Shukla & Singh, 2011; Albani et al., 2010; Bishayee., 2009; Nessa et al., 2012; Baur et al., 2006). Moreover, RES has proven to have the therapeutic potential for Alzheimer’s disease (Ma et al., 2014). In food industry, RES has been extensively used as dietary supplements (doses 10±20 mg). Prior work showed that RES supplement containing diet increased the life span of mice (Porquet et al., 2013).

Challenge found in RES clinical applications is its low bioavailability. RES has shown to be incompletely absorbed after oral administration. Low RES *in-vivo* bioavailability could be

mainly attributed to its poor solubility and rapid metabolism (Amri et al., 2012). It was reported that when RES given orally the bioavailability was less than 1% due to extensive metabolism in liver (Walle, 2011; Walle et al., 2004).

In food and nutrition products, RES is widely used as daily supplement due to its high antioxidant and free radical scavenging activities. However, the high cost and low aqueous solubility limited the application of RES in food industry. Furthermore, RES is chemically instable in solution, the sensitive *trans*-RES form can be isomerized to *cis* form when being exposed to UV light, therefore, RES-containing products suffered from poor storage stability issue.

To overcome RES poor solubility issue, particle size reduction, such as nanosizing, has proven to be an effective approach to improve RES topical delivery (Shrotriya et al., 2017). Furthermore, novel delivery systems have been designed to increase RES delivery efficiency by incorporating it into nano-carriers, including liposomes, cyclodextrins, solid lipid nanoparticles and polymeric micelles (Coimbra et al., 2011; Soo et al., 2016; Kumar et al., 2017; Borah et al., 2020; Loureiro et al., 2017; Li et al., 2017).

Co-crystals have emerged as a useful method to modulate physicochemical properties of RES without changing molecular structure (Rosa et al., 2019).

Lipid-based formulations, such as, nano/micro-emulsions, micellar solutions of bile acids, solid liquid nanoparticles, liposomes-based systems have been developed for oral delivery of RES. Such delivery systems improved RES solubility and bioavailability through creating mixed micelles to solubilize RES in small intestine (Davidov-Pardo & McClements, 2014).

Moreover, Ca/zinc-pectinate microparticles, HPMCAS and HPMC were applied to protect RES from chemical degradation and rapid metabolism (la Porte, et al., 2010; Liu et al., 2018).

### 1.3.2 Griseofulvin

Griseofulvin (Gris, C<sub>17</sub>H<sub>17</sub>ClO<sub>6</sub>, log P 2.17, Mw: 352.77 g/mol) is an antifungal drug isolated from *Penicillium spp's metabolites* (Aggarwal et al., 2013). Gris was the first available oral agent for the treatment of mold infections caused by *Microsporum*, *Epidermophyton* and *Trichophyton*. In history, Gris has been utilized to treat dermatophytosis, such as, ringworm, athlete's foot, jock itch, and fungal infections of the scalp or fingernails, in humans for over half century (Scholz & Meinhof, 1991).

Gris, according to the Biopharmaceutics Classification System (BCS), is BCS class II drug, which is low in solubility and high in permeability) (Fujioka et al., 2007). The poor water-solubility reduced the bioavailability of Gris. Therefore, its oral administration has been typically challenging as much higher amount Gris was required to formulate oral dosage forms.

Numerous delivery systems have been applied to improve the bioavailability Gris through enhancing its solubility. Micronization, nanosization and supercritical fluid technologies were employed to realize the enhanced solubility and absorption of Gris (Reverchon et al., 2004; Lee, 2017).

Self-emulsifying system, liposomes, Pickering emulsion and microemulsions have been regarded as the most promising delivery system for lipophilic drugs like Gris (Sy et al., 2018; Kumar, 2019; Zadeha et al., 2017).

Crystal modifications, such as, polymorphs and co-crystals have proven to improve aqueous solubility by changing Gris crystal forms (Su et al., 2018; Yang et al., 2016)

Solid dispersions of Gris with polymers, such as, cyclodextrin, microcrystalline cellulose, mesoporous silicas, or HPMCAS can substantially improve the solubility of Gris (Omar et al., 2020; Al-Obaidi et al., 2019; Juère et al., 2017).

Commercially available Gris includes: microsize Gris in oral suspension form; Gris-PEG as a solid dispersion of Gris in PEG 400 and PEG 8000. Polymers like PEG 400 and PEG 8000 prohibit crystal growth of active ingredients, and encourage hydrogen-bonds formed between Gris and polymer carriers (Yang et al., 2016; Dickinson, 2008).

Compared to oral dosage form, topical applied Gris is usually in low amount. However, slow absorption rate of Gris creates therapeutic challenge for topical formulations. Therefore, to improve topical administration efficiency, stable and sustained-release form of dosage is to be developed. Supramolecular gels were formulated with Gris to realize sustained release and enhanced transdermal permeation, through establishing high drug concentration gradient across membrane (Al-Obaidi et al., 2019). Vesicular carriers achieved an enhanced and sustained transdermal delivery of Gris to overcome skin and membrane barriers (Mbah et al., 2019; Marto et al., 2016).

Around 20-25% of the population are affect by fungal associated skin infections. Pathogens responsible for skin mycoses are primarily dermatophytes, such as *Trichophyton*, *Microsporum* and *Epidermophyton* (Havlickova et al., 2008). *Trichophyton rubrum*, among dermatophytes, is

the most common dermatophyte associated with skin onychomycosis, tinea pedis, tinea cruris, tinea corporis and is known to account for more than half of all dermatophyte infections (Havlickova et al., 2008). Dermatophytes usually cause benign and common infections; however, they may lead to invasive and aggressive form of infections in immunocompromised patients (Rouzaud et al., 2016), such as, Majocchi's granuloma, disseminated infections and deep dermatophytosis (Nir-Paz et al., 2003).

Prior work has proved that terbinafine, griseofulvin, terbinafine, ketoconazole, fluconazole and itraconazole can fight against dermatophytes effectively *in-vitro* (Gupta et al., 2005). Griseofulvin, terbinafine and itraconazole are very widely used as therapeutic treatments for systemic fungal infections (Mukherjee et al., 2003). They are administrated both orally and topically.

Griseofulvin is one of the most commonly used anti-fungal medicine to treat *Trichophyton rubrum* associated dermatophytosis, the antimicrobial mechanism by which it inhibits the fungal cell division process through disrupting mitotic spindles (Griffiths, 1999).

Dermatophytes such as *T. rubrum*, keratinolytic, saprophytic fungi, were known to form biofilm and commonly implicated as a common cause for athlete's foot and fungal infection. Recent studies suggested that Gris could be considered as great candidate for the inhibition of fungal biofilm formation (Al-Obaidi et al., 2019). Gris oral tablet was used to treat fungal infections of your hair, nails, and skin, however, its oral administration is limited by poor bioavailability.

#### 1.4 Reference

- Aggarwal, N., Goindi, S., & Khurana, R. (2013). Formulation, characterization and evaluation of an optimized microemulsion formulation of griseofulvin for topical application. *Colloids and Surfaces B: Biointerfaces*, 105, 158-166.
- Akers, W., & Haidekker, M. A. (2004). A molecular rotor as viscosity sensor in aqueous colloid solutions. *J. Biomech. Eng.*, 126(3), 340-345.
- Al-Obaidi, H., Kowalczyk, R. M., Kalgudi, R., & Zariwala, M. G. (2019). Griseofulvin solvate solid dispersions with synergistic effect against fungal biofilms. *Colloids and Surfaces B: Biointerfaces*, 184, 110540.
- Albani, D., Polito, L., Signorini, A., & Forloni, G. (2010). Neuroprotective properties of resveratrol in different neurodegenerative disorders. *Biofactors*, 36(5), 370-376.

- Amri, A., Chaumeil, J. C., Sfar, S., & Charrueau, C. (2012). Administration of resveratrol: what formulation solutions to bioavailability limitations? *Journal of controlled release*, *158*(2), 182-193.
- Badr-Eldin, S. M., Ahmed, T. A., & Ismail, H. R. (2013). Aripiprazole-cyclodextrin binary systems for dissolution enhancement: effect of preparation technique, cyclodextrin type and molar ratio. *Iranian journal of basic medical sciences*, *16*(12), 1223.
- Bahl, D., & Bogner, R. H. (2006). Amorphization of indomethacin by co-grinding with Neusilin US2: amorphization kinetics, physical stability and mechanism. *Pharmaceutical research*, *23*(10), 2317-2325.
- Baur, J. A., Pearson, K. J., Price, N. L., Jamieson, H. A., Lerin, C., Kalra, A., ... & Pistell, P. J. (2006). Resveratrol improves health and survival of mice on a high-calorie diet. *Nature*, *444*(7117), 337-342.
- Bi, L., Yang, L., Bhunia, A. K., & Yao, Y. (2011a). Carbohydrate nanoparticle-mediated colloidal assembly for prolonged efficacy of bacteriocin against food pathogen. *Biotechnology and bioengineering*, *108*(7), 1529-1536.
- Bi, L., Yang, L., Bhunia, A. K., & Yao, Y. (2016). Emulsion stabilized with phytoglycogen octenyl succinate prolongs the antimicrobial efficacy of  $\epsilon$ -poly-l-lysine against *Escherichia coli* O157: H7. *LWT*, *70*, 245-251.
- Bi, L., Yang, L., Narsimhan, G., Bhunia, A. K., & Yao, Y. (2011b). Designing carbohydrate nanoparticles for prolonged efficacy of antimicrobial peptide. *Journal of Controlled Release*, *150*(2), 150-156.
- Bishayee, A. (2009). Cancer prevention and treatment with resveratrol: from rodent studies to clinical trials. *Cancer prevention research*, *2*(5), 409-418.
- Borah, H. J., Gogoi, M., Das, D. B., & Hazarika, S. (2020). Cyclodextrine-glutaraldehyde cross-linked nanofiltration membrane for recovery of resveratrol from plant extract. *Journal of Environmental Chemical Engineering*, *8*(1), 103620.
- Bracco, S., Miyano, T., Negroni, M., Bassanetti, I., Marchio, L., Sozzani, P., ... & Comotti, A. (2017). CO<sub>2</sub> regulates molecular rotor dynamics in porous materials. *Chemical Communications*, *53*(55), 7776-7779.

- Cabezas, D. M., Pascual, G. N., Wagner, J. R., & Palazolo, G. G. (2019). Nanoparticles assembled from mixtures of whey protein isolate and soluble soybean polysaccharides. Structure, interfacial behavior and application on emulsions subjected to freeze-thawing. *Food Hydrocolloids*, *95*, 445-453.
- Chatterjee, K., Mukherjee, S., Vanmanen, J., Banerjee, P., & Fata, J. E. (2019). Dietary polyphenols, resveratrol and pterostilbene exhibit antitumor activity on an HPV E6-positive cervical cancer model An in vitro and in vivo analysis. *Frontiers in oncology*, *9*, 352.
- Chen, H., & Yao, Y. (2017a). Phytoglycogen to increase lutein solubility and its permeation through Caco-2 monolayer. *Food Research International*, *97*, 258-264.
- Chen, H., & Yao, Y. (2017b). Phytoglycogen improves the water solubility and Caco-2 monolayer permeation of quercetin. *Food chemistry*, *221*, 248-257.
- Chiou, W. L., & Riegelman, S. (1969). Preparation and dissolution characteristics of several fast-release solid dispersions of griseofulvin. *Journal of pharmaceutical sciences*, *58*(12), 1505-1510.
- Coimbra, M., Isacchi, B., van Bloois, L., Torano, J. S., Ket, A., Wu, X., ... & Bilia, R. (2011). Improving solubility and chemical stability of natural compounds for medicinal use by incorporation into liposomes. *International journal of pharmaceutics*, *416*(2), 433-442.
- Davidov-Pardo, G., & McClements, D. J. (2014). Resveratrol encapsulation: designing delivery systems to overcome solubility, stability and bioavailability issues. *Trends in Food Science & Technology*, *38*(2), 88-103.
- De La Lastra, C. A., & Villegas, I. (2007). Resveratrol as an antioxidant and pro-oxidant agent: mechanisms and clinical implications.
- De, R., Kundu, P., Swarnakar, S., Ramamurthy, T., Chowdhury, A., Nair, G. B., & Mukhopadhyay, A. K. (2009). Antimicrobial activity of curcumin against *Helicobacter pylori* isolates from India and during infections in mice. *Antimicrobial agents and chemotherapy*, *53*(4), 1592-1597.
- DeFelice, S. L. (1995). The nutraceutical revolution: its impact on food industry R&D. *Trends in Food Science & Technology*, *6*(2), 59-61.

- Dent, M. R., López-Duarte, I., Dickson, C. J., Geoghegan, N. D., Cooper, J. M., Gould, I. R., ... & Kuimova, M. K. (2015). Imaging phase separation in model lipid membranes through the use of BODIPY based molecular rotors. *Physical Chemistry Chemical Physics*, *17*(28), 18393-18402.
- Dickinson, C. (2008). Antimicrobials: Use judiciously to avoid potential adverse events. *Infectious Diseases in Children*, *21*(1), 26.
- Dickinson, E. (1998). Proteins at interfaces and in emulsions stability, rheology and interactions. *Journal of the Chemical Society, Faraday Transactions*, *94*(12), 1657-1669.
- Espinoza, J. L., Kurokawa, Y., & Takami, A. (2019). Rationale for assessing the therapeutic potential of resveratrol in hematological malignancies. *Blood reviews*, *33*, 43-52.
- Fraga, C. G., Croft, K. D., Kennedy, D. O., & Tomás-Barberán, F. A. (2019). The effects of polyphenols and other bioactives on human health. *Food & function*, *10*(2), 514-528.
- Frochot, C., Mascherin, M., Haumont, A., Viriot, M. L., & Marie, E. (2011). Fluorescence spectroscopy as a non invasive tool to follow in situ the polymerization in miniemulsion. *Journal of Applied Polymer Science*, *119*(1), 219-224.
- Fujioka, Y., Kadono, K., Fujie, Y., Metsugi, Y., Ogawara, K. I., Higaki, K., & Kimura, T. (2007). Prediction of oral absorption of griseofulvin, a BCS class II drug, based on GITA model: utilization of a more suitable medium for in-vitro dissolution study. *Journal of controlled release*, *119*(2), 222-228.
- Gielen, B. (2017). Particle Engineering by Sonocrystallization: Controlling particle size and shape by a targeted application of ultrasound.
- Gillies, E. R., & Frechet, J. M. (2005). Dendrimers and dendritic polymers in drug delivery. *Drug discovery today*, *10*(1), 35-43.
- Griffiths, W. A. D. (1999). WHO model prescribing information-drugs used in skin diseases. *Clinical & Experimental Dermatology*, *24*(1).
- Gupta, A. K., Kohli, Y., & Batra, R. (2005). In vitro activities of posaconazole, ravuconazole, terbinafine, itraconazole and fluconazole against dermatophyte, yeast and non-dermatophyte species. *Medical mycology*, *43*(2), 179-185.
- Habib, M. J. (2000). *Pharmaceutical solid dispersion technology*. CRC Press.

- Haidekker, M. A., Brady, T. P., Lichlyter, D., & Theodorakis, E. A. (2005). Effects of solvent polarity and solvent viscosity on the fluorescent properties of molecular rotors and related probes. *Bioorganic chemistry*, 33(6), 415-425.
- Haidekker, M. A., Ling, T., Anglo, M., Stevens, H. Y., Frangos, J. A., & Theodorakis, E. A. (2001). New fluorescent probes for the measurement of cell membrane viscosity. *Chemistry & biology*, 8(2), 123-131.
- Haidekker, M. A., Nipper, M., Mustafic, A., Lichlyter, D., Dakanali, M., & Theodorakis, E. A. (2010). Dyes with segmental mobility: molecular rotors. In *Advanced Fluorescence Reporters in Chemistry and Biology I* (pp. 267-308). Springer, Berlin, Heidelberg.
- Hardy, G. (2000). Nutraceuticals and functional foods: introduction and meaning. *Nutrition (Burbank, Los Angeles County, Calif.)*, 16(7-8), 688-689.
- Havlickova, B., Czaika, V. A., & Friedrich, M. (2008). Epidemiological trends in skin mycoses worldwide. *Mycoses*, 51, 2-15.
- Hawe, A., Filipe, V., & Jiskoot, W. (2010). Fluorescent molecular rotors as dyes to characterize polysorbate-containing IgG formulations. *Pharmaceutical research*, 27(2), 314-326.
- Iohara, D., Anraku, M., Uekama, K., & Hirayama, F. (2019). Modification of Drug Crystallization by Cyclodextrins in Pre-formulation Study. *Chemical and Pharmaceutical Bulletin*, 67(9), 915-920.
- Jiang, N., Wang, S., Cheng, Z., & Liu, W. (2019). In vitro and in vivo evaluation of porous lactose/mannitol carriers for solubility enhancement of poorly water-soluble drugs. *Drying Technology*, 1-14.
- Jiang, X., & Doyle, M. P. (2002). Optimizing enrichment culture conditions for detecting *Helicobacter pylori* in foods. *Journal of food protection*, 65(12), 1949-1954.
- Juère, E., Florek, J., Bouchoucha, M., Jambhrunkar, S., Wong, K. Y., Popat, A., & Kleitz, F. (2017). In vitro dissolution, cellular membrane permeability, and anti-inflammatory response of resveratrol-encapsulated mesoporous silica nanoparticles. *Molecular pharmaceutics*, 14(12), 4431-4441.
- Kumar, R. (2019). Nanotechnology based approaches to enhance aqueous solubility and bioavailability of griseofulvin: A literature survey. *Journal of Drug Delivery Science and Technology*, 101221.

- Kumar, R., Kaur, K., Uppal, S., & Mehta, S. K. (2017). Ultrasound processed nanoemulsion: A comparative approach between resveratrol and resveratrol cyclodextrin inclusion complex to study its binding interactions, antioxidant activity and UV light stability. *Ultrasonics sonochemistry*, *37*, 478-489.
- la Porte, C., Voduc, N., Zhang, G., Seguin, I., Tardiff, D., Singhal, N., & Cameron, D. W. (2010). Steady-state pharmacokinetics and tolerability of trans-RES 2000mg twice daily with food, quercetin and alcohol (ethanol) in healthy human subjects. *Clinical pharmacokinetics*, *49*(7), 449-454.
- Lai, H. P., Gao, R. C., Huang, C. L., Chen, I. C., & Tan, K. T. (2015). Fluorescence switchable probes based on a molecular rotor for selective detection of proteins and small molecules. *Chemical Communications*, *51*(90), 16197-16200.
- Lee, B. J. (2017, June). Controlled Nanonization of Poorly Water-Soluble Drugs for Reliable Bioavailability. In *International Conference on the Development of Biomedical Engineering in Vietnam* (pp. 827-830). Springer, Singapore.
- Li, T. P., Wong, W. P., Chen, L. C., Su, C. Y., Chen, L. G., Liu, D. Z., ... & Sheu, M. T. (2017). Physical and pharmacokinetic characterizations of trans-resveratrol (t-Rev) encapsulated with self-assembling lecithin-based mixed polymeric micelles (sa LMPMs). *Scientific reports*, *7*(1), 1-10.
- Liu, T., Müller, R. H., & Möschwitzer, J. P. (2018). Consideration of the solid state for resveratrol nanocrystal production. *Powder technology*, *332*, 63-69.
- Loureiro, J. A., Andrade, S., Duarte, A., Neves, A. R., Queiroz, J. F., Nunes, C., ... & Pereira, M. C. (2017). Resveratrol and grape extract-loaded solid lipid nanoparticles for the treatment of Alzheimer's disease. *Molecules*, *22*(2), 277.
- Lu, F., Mencia, A., Bi, L., Taylor, A., Yao, Y., & HogenEsch, H. (2015). Dendrimer-like alpha-d-glucan nanoparticles activate dendritic cells and are effective vaccine adjuvants. *Journal of Controlled Release*, *204*, 51-59.
- Ma, T., Tan, M. S., Yu, J. T., & Tan, L. (2014). Resveratrol as a therapeutic agent for Alzheimer's disease. *BioMed research international*, *2014*.
- Martín, A., Mattea, F., Gutiérrez, L., Miguel, F., & Cocero, M. J. (2007). Co-precipitation of carotenoids and bio-polymers with the supercritical anti-solvent process. *The Journal of Supercritical Fluids*, *41*(1), 138-147.

- Marto, J., Vitor, C., Guerreiro, A., Severino, C., Eleutério, C., Ascenso, A., & Simões, S. (2016). Ethosomes for enhanced skin delivery of griseofulvin. *Colloids and Surfaces B: Biointerfaces*, 146, 616-623.
- Mbah, C. C., Builders, P. F., Agubata, C. O., & Attama, A. A. (2019). Development of ethosomal vesicular carrier for topical application of griseofulvin: effect of ethanol concentration. *Journal of pharmaceutical investigation*, 49(1), 27-36.
- McClements, D. J. (2007). Critical review of techniques and methodologies for characterization of emulsion stability. *Critical reviews in food science and nutrition*, 47(7), 611-649.
- McClements, D. J., Decker, E. A., & Weiss, J. (2007). Emulsion-based delivery systems for lipophilic bioactive components. *Journal of Food Science*, 72(8), R109-R124.
- Miriani, M., Iametti, S., Bonomi, F., & Corredig, M. (2012). Structural changes of soy proteins at the oil–water interface studied by fluorescence spectroscopy. *Colloids and Surfaces B: Biointerfaces*, 93, 41-48.
- Mognetti, B., Barberis, A., Marino, S., Berta, G., De Francia, S., Trotta, F., & Cavalli, R. (2012). In vitro enhancement of anticancer activity of paclitaxel by a Cremophor free cyclodextrin-based nanosponge formulation. *Journal of Inclusion Phenomena and Macrocyclic Chemistry*, 74(1-4), 201-210.
- Mohr, A., Talbiersky, P., Korth, H. G., Sustmann, R., Boese, R., Bläser, D., & Rehage, H. (2007). A new pyrene-based fluorescent probe for the determination of critical micelle concentrations. *The Journal of Physical Chemistry B*, 111(45), 12985-12992.
- Mori, T., Komatsu, H., Sakamoto, N., Suzuki, K., Hill, J. P., Matsumoto, M., ... & Nakanishi, W. (2018). Molecular rotors confined at an ordered 2D interface. *Physical Chemistry Chemical Physics*, 20(5), 3073-3078.
- Mukherjee, P. K., Leidich, S. D., Isham, N., Leitner, I., Ryder, N. S., & Ghannoum, M. A. (2003). Clinical *Trichophyton rubrum* strain exhibiting primary resistance to terbinafine. *Antimicrobial agents and Chemotherapy*, 47(1), 82-86.
- Mustafic, A., Huang, H. M., Theodorakis, E. A., & Haidekker, M. A. (2010). Imaging of flow patterns with fluorescent molecular rotors. *Journal of fluorescence*, 20(5), 1087-1098.
- Nasri, H., A. Baradaran, H. Shirzad & M. Rafieian-Kopaei (2014). New Concepts in Nutraceuticals as Alternative for Pharmaceuticals. *International Journal of Preventive Medicine*, 5, 1487-1499.

- Nessa, M. U., Beale, P., Chan, C., Yu, J. Q., & Huq, F. (2012). Combinations of resveratrol, cisplatin and oxaliplatin applied to human ovarian cancer cells. *Anticancer research*, 32(1), 53-59.
- Nir-Paz, R., Elinav, H., Pierard, G. E., Walker, D., Maly, A., Shapiro, M., ... & Polacheck, I. (2003). Deep infection by *Trichophyton rubrum* in an immunocompromised patient. *Journal of clinical microbiology*, 41(11), 5298-5301.
- Oellig, C., Link, K., & Schwack, W. (2020). Characterization of E 472 food emulsifiers by high-performance thin-layer chromatography with fluorescence detection and mass spectrometry. *Journal of Chromatography A*, 460874.
- Ohtsuru, M., & Kito, M. (1983). Association of phosphatidylcholine with soybean 11S globulin. *Agricultural and Biological Chemistry*, 47(8), 1907-1908.
- Omar, S. M., Ibrahim, F., & Ismail, A. (2020). Formulation and Evaluation of Cyclodextrin-Based Nanosponges of Griseofulvin as Pediatric Oral Liquid Dosage Form for Enhancing Bioavailability and Masking Bitter Taste. *Saudi Pharmaceutical Journal*.
- Pessi, J., Lassila, I., Meriläinen, A., Räikkönen, H., Hæggström, E., & Yliruusi, J. (2016). Controlled expansion of supercritical solution: a robust method to produce pure drug nanoparticles with narrow size-distribution. *Journal of pharmaceutical sciences*, 105(8), 2293-2297.
- Poms, R. E., & Tatini, S. R. (2001). Survival of *Helicobacter pylori* in ready-to-eat foods at 4 C. *International journal of food microbiology*, 63(3), 281-286.
- Porquet, D., Casadesús, G., Bayod, S., Vicente, A., Canudas, A. M., Vilaplana, J., ... & Del Valle, J. (2013). Dietary resveratrol prevents Alzheimer's markers and increases life span in SAMP8. *Age*, 35(5), 1851-1865.
- Porter Iii, W. W., Elie, S. C., & Matzger, A. J. (2008). Polymorphism in carbamazepine cocrystals. *Crystal Growth and Design*, 8(1), 14-16.
- Renaud, S. D., & de Lorgeril, M. (1992). Wine, alcohol, platelets, and the French paradox for coronary heart disease. *The Lancet*, 339(8808), 1523-1526.
- Reverchon, E., Porta, G. D., Spada, A., & Antonacci, A. (2004). Griseofulvin micronization and dissolution rate improvement by supercritical assisted atomization. *Journal of pharmacy and pharmacology*, 56(11), 1379-1387.

- Rodriguez-Rosales, R. J., & Yao, Y. (2020). Phytoglycogen, a natural dendrimer-like glucan, improves the soluble amount and Caco-2 monolayer permeation of curcumin and enhances its efficacy to reduce HeLa cell viability. *Food Hydrocolloids*, *100*, 105442.
- Rosa, J., Machado, T. C., da Silva, A. K., Kuminek, G., Bortolluzzi, A. J., Caon, T., & Cardoso, S. G. (2019). Isoniazid-resveratrol cocrystal: a novel alternative for topical treatment of cutaneous tuberculosis. *Crystal Growth & Design*, *19*(9), 5029-5036.
- Rouzaud, C., Hay, R., Chosidow, O., Dupin, N., Puel, A., Lortholary, O., & Lanternier, F. (2016). Severe dermatophytosis and acquired or innate immunodeficiency: a review. *Journal of Fungi*, *2*(1), 4.
- Santos, A. M., Lopes, T., Oleastro, M., Gato, I. V., Floch, P., Benejat, L., ... & Guerreiro, A. S. (2015). Curcumin inhibits gastric inflammation induced by Helicobacter pylori infection in a mouse model. *Nutrients*, *7*(1), 306-320.
- Santos, C. I., Ribeiro, A. C., & Estes, M. A. (2019). Drug delivery systems: study of inclusion complex formation between Methylxanthines and Cyclodextrins and their Thermodynamic and Transport properties. *Biomolecules*, *9*(5), 196.
- Sawada, S., Iio, T., Hayashi, Y., & Takahashi, S. (1992). Fluorescent rotors and their applications to the study of GF transformation of Actin. *Analytical biochemistry*, *204*(1), 110-117.
- Scheffler, S. L., Huang, L., Bi, L., & Yao, Y. (2010a). In vitro digestibility and emulsification properties of phytoglycogen octenyl succinate. *Journal of agricultural and food chemistry*, *58*(8), 5140-5146.
- Scheffler, S. L., Wang, X., Huang, L., San-Martin Gonzalez, F., & Yao, Y. (2010b). Phytoglycogen octenyl succinate, an amphiphilic carbohydrate nanoparticle, and  $\epsilon$ -polylysine to improve lipid oxidative stability of emulsions. *Journal of agricultural and food chemistry*, *58*(1), 660-667.
- Scholz, R., & Meinhof, W. (1991). Susceptibility of *Trichophyton rubrum* to griseofulvin: Die Empfindlichkeit von *Trichophyton rubrum* gegenüber Griseofulvin. *Mycoses*, *34*(9-10), 411-414.
- Shen, Y., Chang, C., Shi, M., Su, Y., Gu, L., Li, J., & Yang, Y. (2020). Interactions between lecithin and yolk granule and their influence on the emulsifying properties. *Food Hydrocolloids*, *101*, 105510.

- Shrotriya, S. N., Ranpise, N. S., & Vidhate, B. V. (2017). Skin targeting of resveratrol utilizing solid lipid nanoparticle-engrossed gel for chemically induced irritant contact dermatitis. *Drug delivery and translational research*, 7(1), 37-52.
- Shukla, Y., & Singh, R. (2011). Resveratrol and cellular mechanisms of cancer prevention. *Annals of the New York Academy of Sciences*, 1215(1), 1-8.
- Soo, E., Thakur, S., Qu, Z., Jambhrunkar, S., Parekh, H. S., & Popat, A. (2016). Enhancing delivery and cytotoxicity of resveratrol through a dual nanoencapsulation approach. *Journal of colloid and interface science*, 462, 368-374.
- Su, Y., Xu, J., Shi, Q., Yu, L., & Cai, T. (2018). Polymorphism of griseofulvin: concomitant crystallization from the melt and a single crystal structure of a metastable polymorph with anomalously large thermal expansion. *Chemical communications*, 54(4), 358-361.
- Sy, P. M., Djiboune, A. R., Diouf, L. A. D., Soumboundou, M., Ndong, B., Ndiaye, A., ... & Faye, M. (2018). Water/Oil Pickering Emulsion Stabilized by Magnesium Oxide Particles: A Potential System with Two Active Substances (Paracetamol and Griseofulvin). *Open Journal of Biophysics*, 8(02), 68.
- Tiwary, A. K. (2001). Modification of crystal habit and its role in dosage form performance. *Drug development and industrial pharmacy*, 27(7), 699-709.
- Tuerk, M., & Bolten, D. (2016). Polymorphic properties of micronized mefenamic acid, nabumetone, paracetamol and tolbutamide produced by rapid expansion of supercritical solutions (RESS). *The Journal of Supercritical Fluids*, 116, 239-250.
- Walle, T. (2011). Bioavailability of resveratrol. *Annals of the new York Academy of Sciences*, 1215(1), 9-15.
- Walle, T., Hsieh, F., DeLegge, M. H., Oatis, J. E., & Walle, U. K. (2004). High absorption but very low bioavailability of oral resveratrol in humans. *Drug metabolism and disposition*, 32(12), 1377-1382.
- Wang, W. (2000). Lyophilization and development of solid protein pharmaceuticals. *International journal of pharmaceutics*, 203(1-2), 1-60.
- Wattebled, F., Dong, Y., Dumez, S., Delvallé, D., Planchot, V., Berbezy, P., ... & d'Hulst, C. (2005). Mutants of Arabidopsis lacking a chloroplastic isoamylase accumulate phytylglycogen and an abnormal form of amylopectin. *Plant Physiology*, 138(1), 184-195.

- Wilde, P., Mackie, A., Husband, F., Gunning, P., & Morris, V. (2004). Proteins and emulsifiers at liquid interfaces. *Advances in colloid and interface Science*, 108, 63-71.
- Wu, D., & Sarsfield, B. A. (2018). Particle Size Reduction: From Microsizing to Nanosizing. *Early Drug Development: Bringing a Preclinical Candidate to the Clinic*, 1, 271-304.
- Xie, Y., & Yao, Y. (2018). Octenylsuccinate hydroxypropyl phytyglycogen, a dendrimer-like biopolymer, solubilizes poorly water-soluble active pharmaceutical ingredients. *Carbohydrate Polymers*, 180, 29-37.
- Xie, Y., & Yao, Y. (2018a). Octenylsuccinate hydroxypropyl phytyglycogen enhances the solubility and in-vitro antitumor efficacy of niclosamide. *International journal of pharmaceutics*, 535(1-2), 157-163.
- Xie, Y., & Yao, Y. (2018b). Octenylsuccinate hydroxypropyl phytyglycogen, a dendrimer-like biopolymer, solubilizes poorly water-soluble active pharmaceutical ingredients. *Carbohydrate polymers*, 180, 29-37.
- Xie, Y., & Yao, Y. (2019). Incorporation with Dendrimer-Like Biopolymer Leads to Improved Soluble Amount and In Vitro Anticancer Efficacy of Paclitaxel. *Journal of pharmaceutical sciences*, 108(6), 1984-1990.
- Yang, R., Zhang, S., Kong, D., Gao, X., Zhao, Y., & Wang, Z. (2012). Biodegradable polymer-curcumin conjugate micelles enhance the loading and delivery of low-potency curcumin. *Pharmaceutical research*, 29(12), 3512-3525.
- Yang, X., Zhong, Z., & Huang, Y. (2016). The effect of PEG molecular weights on the thermal stability and dissolution behaviors of griseofulvin-PEG crystalline inclusion complexes. *International journal of pharmaceutics*, 508(1-2), 51-60.
- Yang, Z. Y., Yen, S. K., Hu, W. S., Huang, Y. Z., Yang, T. M., & Su, C. S. (2018). Sonocrystallization—Case studies of salicylamide particle size reduction and isoniazid derivative synthesis and crystallization. *Crystals*, 8(6), 249.
- Yang, Z., Cao, J., He, Y., Yang, J. H., Kim, T., Peng, X., & Kim, J. S. (2014). Macro-/micro-environment-sensitive chemosensing and biological imaging. *Chemical Society Reviews*, 43(13), 4563-4601

- Yu, W. T., Wu, T. W., Huang, C. L., Chen, I. C., & Tan, K. T. (2016). Protein sensing in living cells by molecular rotor-based fluorescence-switchable chemical probes. *Chemical science*, 7(1), 301-307.
- Zadeha, B. S. M., Salimi, A., & Aminib, R. (2017). Novel Super Saturated Self-Emulsifying System for Oral Delivery of Griseofulvin: Design, Preparation and ex-vivo Intestinal Permeability. *Journal of Reports in Pharmaceutical Sciences*, 6(2), 180-190.
- Zhang, F., Liu, J., & Shi, J. S. (2010). Anti-inflammatory activities of resveratrol in the brain: role of resveratrol in microglial activation. *European Journal of Pharmacology*, 636(1-3), 1-7.
- Zhang, X., Jackson, J. K., & Burt, H. M. (1996). Determination of surfactant critical micelle concentration by a novel fluorescence depolarization technique. *Journal of biochemical and biophysical methods*, 31(3-4), 145-150.

## CHAPTER 2. PHYTOGLYCOGEN TO ENHANCE THE SOLUBLE AMOUNT AND *IN-VITRO* EFFICIENCY OF RESVERATROL

### 2.1 Abstract

Resveratrol (RES) poor solubility leads to incomplete absorption and low bioavailability. The aim of this study was to investigate the capability of phytoglycogen (PG), a naturally occurring and biodegradable dendrimer-like biopolymer, to improve RES water soluble amount and bioavailability. RES and PG were incorporated through co-solvent mixing followed with spray-drying at PG:RES ratios ranging from 4/1 to 50/1. The obtained PG-RES solid dispersions were evaluated for RES in-vitro performances. Results showed that the soluble amount of RES reached 289.6  $\mu\text{g/mL}$  at PG:RES of 50:1 compared with 45.6  $\mu\text{g/mL}$  at RES alone. X-ray diffraction patterns suggested a significant reduction of RES crystallinity in PG-RES solid dispersion. FT-IR spectra indicated the formation of hydrogen bond between RES and PG. The Caco-2 monolayer permeation of RES from PG-RES solid dispersion was 1.28 to 1.8 times that of RES alone, which was associated with the improved soluble amount of RES.

### 2.2 Introduction

Resveratrol (RES, trans-3, 4', 5-trihydroxystilbene), a natural polyphenol, displays diverse biochemical and physiological functions. RES was first identified as medicinal component abundant in grapes, peanut, berries and plants (Shi et al., 2008; Devi et al., 2019). During the past decades, over 250 clinical trials have demonstrated the therapeutic and pharmacological functions of RES (Singh et al., 2019), including, antioxidant (Sessa et al., 2014), anti-cancer, anti-inflammatory, anti-carcinogenic (la Porte et al., 2010), anti-obesity (Davidov-Pardo & McClements, 2014), and cardiovascular preventative activities (Bradamante et al., 2004). Furthermore, other studies suggested that RES played an important role in the defense against various fungal and bacterial infections, ultraviolet radiation (UV) and water deprivation (Das & Maulik, 2006; Murcia & Martinez-Tome, 2001). Recently, report showed that resveratrol exhibited potent antiviral activities against SARS-CoV-2 in-vitro through interfering the post-entry steps of virus replication (ter Ellen et al., 2020), and more clinical trials are to be conducted.

Due to the wide spectrum of health and therapeutic benefits, RES received a great amount of attention for its applications as food additive and active pharmaceutical ingredient.

However, RES low water solubility ( $< 0.05$  mg/mL), photosensitivity, short half-life (Gambini et al., 2015), chemical instability and high metabolism rate led to poor oral bioavailability, and impeded its application in aqueous-based food products. An increasing number of studies aimed at preparing novel delivery system for enhanced RES bioavailability through improving its solubility, stability and dissolution rate. Nano-emulsions (Sessa et al., 2006), micro-emulsions (Tang et al., 2019), double emulsions (Hemar et al., 2010), micellar solutions of bile acids (Atanacković et al., 2009), solid lipid nanoparticles (Gumireddy et al., 2019), liposomes-based systems (Huang et al., 2019) were all designed to improve RES in-vitro efficacies (Davidov-Pardo & McClements, 2014). Polymer-based delivery systems, including cyclodextrin complexation (Lu et al., 2009; Lucas-Abellán et al., 2007), Ca/zinc-pectinate microparticles (Gadalla et al., 2016), hydroxypropylmethyl cellulose (Wegiel et al., 2013) were reported for their potential to protect RES from chemical degradation and rapid metabolization (la Porte et al., 2010). However, these processing methods have been associated with numerous issues, such as expensive/non-biodegradable material, lengthy process, cytotoxic or non-FDA approvable. As a result, there is a pressing need for all natural, food-grade and cost-effective carriers to achieve high dose delivery of RES for food application.

Phytoglycogen (PG) is a natural dendrimer-like polysaccharides extracted from the kernel of maize mutant sugary-1(su 1) (James et al., 1995; Huang & Yao, 2011). The sugary-1 mutation leads to the deficiency of isoamylase-type starch debranching enzyme (DBE), which subsequently resulted in the accumulation of the highly branched phytoglycogen (Chen & Yao, 2017). The dendritic and extensive branching structure, high water solubility and low viscosity have made PG an ideal candidate for the delivery of hydrophobic molecules. Recent studies showed that PG was employed to enhance the solubility and bioavailability of poorly water-soluble polyphenols, such as curcumin, quercetin, and lutein (Rodriguez-Rosales & Yao, 2019; Chen & Yao, 2017; Chen & Yao, 2017a).

In this study, our hypothesis was that PG was able to enhance the in-vitro efficacies of resveratrol through increasing its aqueous soluble amount. To test the hypothesis, RES was incorporated through co-solvent mixing followed with spray-drying, and the solid collected was subjected to FTIR, XRD, phase solubility, aqueous soluble amount and Caco-2 monolayer

permeation tests. We found that PG particulates interacted with RES molecules through hydrogen bonding, and acted as physical barriers that prohibited the crystallization of amorphous RES molecules. For RES-PG solid dispersion, the soluble amount of RES was increased by 1.04-5.35 folds, depending on the ratio of PG/RES, which led to the increase of Caco-2 monolayer permeation. PG is a naturally occurring and abundant crop-based polysaccharide, and its capability to increase RES solubility may have important implication for enhancing the nutritional benefits of RES-containing foods.

## **2.3 Materials and methods**

### **2.3.1 Materials**

Resveratrol was purchased from TCI Chemicals Pvt. Ltd. The Caco-2 BBE cell was purchased from ATCC (Rockville, MD). Lactate dehydrogenase (LDH) kit assay was obtained from Thermo Fisher Scientific. All other chemicals were of reagent grade. Double-distilled water was freshly prepared whenever required.

### **2.3.2 Extraction of phytoglycogen (PG)**

PG was prepared according to the method described by Chen et al. (2015). Firstly, Silver Queen corn kernels were grounded into grits and homogenized with five weights of cold deionized water using a high-speed blender (model). The homogenized dispersion was subjected to a 270-mesh sieve, and the filtrate was centrifuged at  $16,000 \times g$  for 15 min. The supernatant was collected and adjusted to pH 4.6, followed by centrifugation ( $16,000 \times g$  for 15 min) to remove the flocculates. The supernatant was adjusted to pH 6.5, autoclaved ( $121^\circ\text{C}$ , 45 min), and centrifuged ( $16,000 \times g$  for 15 min) to remove denatured proteinaceous materials. To the supernatant, three volumes of ethanol was added and the mixture was centrifuged. The obtained solid was dispersed with ethanol and the dispersion was vacuum filtrated to collect the cake. Residual solvent in the loosened filtration cake was removed in a fume hood.

### **2.3.3 Characterization of PG**

The weight average molecular weight ( $M_w$ ), z-average root means square radius ( $R_z$ ), and dispersed molecular density ( $\rho$ ) were determined. The  $M_w$  and  $R_z$  values of PG was determined

according to the method of Scheffler et al. (2010), using a high-performance size-exclusion chromatography (HPSEC) connected to a multi-angle laser-light scattering detector (MALLS) and a refractive index detector (RI) (Wyatt Technology, Santa Barbara, CA). Two connected columns (PL Aquagel-pH 40 and 60, Polymer Laboratories, Varian) with a guard column were used. Deionized water (pH 6.8, containing 0.02% sodium azide) was used as the mobile phase with a flow rate of 0.7 mL/min. For sample preparation, PG dispersion was prepared by dispersing 5.0 mg solid in 1 mL DI water, followed with heating at 80°C for 10 min with agitation. The dispersion was filtered through a 0.45 µm polypropylene filter, and the injection volume was 20-µL.  $M_w$  and  $R_z$  were determined using Software Astra (Version 5.3.4.14, Wyatt Technology) according to the first-order Berry model with virial coefficient  $A_2$  of zero. The index increment value ( $dn/dc$ ) was set as 0.146. Dispersed molecular density ( $\rho$ ) was calculated as  $\rho = M_w/(R_z)^3$ . The measurements were conducted in triplicate. The  $\zeta$ -potential of PG particulate was measured by a Zetasizer Nano (ZS90, Malvern Instruments Ltd., UK) at room temperature, using PG dispersion prepared in 20 mM sodium acetate buffer (pH 5.5) at concentration of 0.1 mg/mL.

The shape and size of PG particulates were observed by TEM according to Scheffler et al. (2010). Carbon-coated 400 mesh grid (FCF 400-Cu, EMS, PA) was glow discharged before use. Droplets of 0.1 mg/mL PG dispersion prepared in 0.02 M sodium acetate buffer (pH 5.5) was dried on the grid, followed by staining with 2% aqueous uranyl acetate. The PG particulates were imaged using a Tecnai G2 20 TEM (FEI company, OR) operated at 200 kV.

#### **2.3.4 Preparation of PG-RES formulations**

The PG-RES solid dispersions (PG-RES SDs) were prepared by incorporating RES and PG through co-solvent mixing according to Rodríguez-Rosales et al. (2019). PG of 2.0 g was added into 55 mL of DI water, the dispersion was sonicated (Model 505, Fisher Scientific) at 39% amplitude with 20 kHz ultrasonic frequency, and a pulse ratio on/off 25/5 (s/s). Thereafter, 45 mL of RES ethanol solution was gradually added to PG solution based on the RES:PG mass ratios of 1:4, 1:10, 1:20 and 1:50 while maintaining PG continuously sonicated. The ethanol/water dispersion was homogenized before being subjected to spray-dry using a Büchi Mini-spray dryer B-290 (Büchi Labortechnik AG, Switzerland) equipped with nitrogen purge. Operating conditions were: inlet temperature was 90 °C, outlet temperature was 57–60 °C, 6 mL/min feed rate, and

nitrogen flow was 350 L/h. The solvent in the nitrogen gas from the outlet was condensed and collected in a Büchi Inert Loop B-295.

PG:RES physical mixtures (PG/RES PMs) were prepared by physical mixing RES and PG at weight ratios of 1:4, 1:10, 1:20 and 1:50 using a mortar and pestle. All solid dispersions and physical mixtures were stored at -20°C until use.

### **2.3.5 Soluble amount of RES**

RES alone, PG-RES SDs and PG/RES PMs were determined for their RES soluble amount. Briefly, RES-containing solid that contained 500 µg RES was dispersed in 1.0 mL DI water, followed by vortexing for 5 min. The dispersion was centrifuged ( $16,000 \times g$ , 5 min) to remove any insolubles. Thereafter, 0.2 mL of supernatant was withdrawn and added to 0.8 mL ethanol, followed by centrifugation ( $5,000 \times g$ , 3 min) to precipitate any insoluble PG. The RES soluble amount in the supernatant was determined using HPLC assisted with RES standard curve. The measurements were performed in triplicate.

### **2.3.6 High performance liquid chromatography (HPLC) quantification of RES**

To quantify RES amount using HPLC, a standard curve was created. Concentrated stock solution of RES (1.0 mg/mL) was prepared in ethanol: HBSS (80:20, v/v), and further diluted to working standard solutions with concentrations ranging from 0.10 to 80.0 µg/mL. An aliquot of 50.0 µL RES-containing solution was injected into the HPLC system for concentration analysis. The mobile phases consisted of A (H<sub>2</sub>O + 0.1% formic acid) and B (acetonitrile + 0.1% formic acid) with a flow rate of 1.0 mL/min. The chromatographic separation was carried out by gradient elution using an analytical column (5 µm ZORBAX Eclipse XDB-C18, 4.6 × 150 mm; Agilent, Santa Clara, CA) column, where the initial mobile phase composition was maintained at 65% solvent A for 1 min, changed linearly to 30% (1~4 min) and held 1 min (4~5 min), then followed by a return to the initial conditions within 2 min (5~7 min), and kept for another 6 min (7~13 min) for the column equilibrium. The detector was UV-DAD (Diode Array Detector, model G1315B, Santa Clara, CA) set at 306 nm.

### **2.3.7 Phase solubility**

To evaluate the solubilizing capacity of PG, phase solubility measurement was carried out according to the method of Higuchi and Connors (1965). Excess amount of RES was suspended to DI water containing increasing amounts of PG (0~100 mg/mL). All dispersions were shaken for 24 h in a water bath (Ws27 SHEL LAB, VWR Scientific, PA) at 25 °C, followed by centrifugation (16,000× g, 5 min) to remove insoluble RES. The soluble amount of RES in supernatant was determined by HPLC. The measurements were carried out in triplicate.

### **2.3.8 X-ray powder diffraction**

To evaluate the crystallinity of PG and RES in RES-containing solids, x-ray powder diffraction pattern was recorded by an x-ray powder diffractometer (XRD-6000, Shimadzu, North America) equipped with a Bragg-Brentano optical setup. Nickel filtered Cu K $\alpha$  radiation ( $\lambda = 1.5406 \text{ \AA}$ ) was used with a long fine focus x-ray tube. All solid powders were scanned at  $2\theta^\circ$  of  $10^\circ \sim 35^\circ$ , with a scanning speed of  $8^\circ(2\theta)/\text{min}$  at 40 kV and 30 mA. The diffraction patterns of PG, RES alone, PG:RES physical mixtures, and PG-RES solid dispersions were recorded.

### **2.3.9 FT-IR**

The FT-IR spectra were recorded using a Thermo-Nicolet Nexus 470 FT-IR spectrometer (Nicolet, Thermo, USA) equipped with a Smart OMNI-sampler. The scanning range was  $800 \sim 4000 \text{ cm}^{-1}$ , with a resolution of  $4 \text{ cm}^{-1}$  and 40 accumulations. FT-IR spectra of PG, RES alone, PG:RES physical mixtures, and PG-RES solid dispersions were obtained.

### **2.3.10 RES Caco-2 cell monolayer permeation analysis**

#### ***Cell Culture***

The Caco-2 BBE cell line (ATCC, Rockville, MD) was cultured in Dulbecco's Modified Eagle Medium (DMEM) supplemented with 10% fetal bovine serum (FBS), 1% L-glutamine, 100 units/mL penicillin, and 100  $\mu\text{g/mL}$  of streptomycin (Sigma-Aldrich). Cells were grown and incubated at  $37^\circ\text{C}$  under an atmosphere of 5%  $\text{CO}_2$ , at 95% relative humidity. Monolayers were sub-cultured every 3 days after reaching 80–90% confluence. The detached cells were diluted and

re-suspended in new DMEM (10 mL) at a density of  $5.0 \times 10^3$  cells/cm<sup>2</sup>. The passages of Caco-2 cells were in the range of 90-102.

### ***Permeation working dispersions preparation and stability tests***

Working dispersions of RES alone and PG-RES (50:1) SD were used for Caco-2 permeation and cell viability tests. To prepare RES-containing working dispersion, a stock RES dispersion (3000 µg/mL) was firstly prepared by dissolving RES alone and PG-RES (50:1) SD that contained 3 mg of RES in 1 mL of HBSS (pH 6.5, adjusted using 10 mM methanesulfonic acid), then further diluted to RES contents of 15 µg/mL, 30 µg/mL, 150 µg/mL and 300 µg/mL using HBSS (pH 6.5). RES alone working dispersions of high RES concentrations (150 and 300 µg/mL) were not included in further tests as white precipitates were formed at room temperature.

Caco-2 cell permeation test required the incubation of Caco-2 cells with working dispersions for 2 hours, therefore, the stability of RES in RES alone and PG-RES (50:1) SD working dispersions under incubation condition were evaluated. The prepared working dispersion was incubated in a 24 well plate at 37 °C. Aliquots of 0.5 mL were withdrawn from the wells at time 0 min, 60 min and 120 min, and subjected to centrifugation at  $5,000 \times g$  for 3 min. Supernatant (0.2 mL) was collected and immediately transferred into 0.8 mL ethanol for RES soluble amount determination using HPLC.

### ***Caco-2 cell monolayer viability test***

The impact of RES alone and PG-RES SD working dispersions on the viability of Caco-2 cells was evaluated by the LDH assay. Firstly, Caco-2 cells were seeded in 24-well plates (Corning, NY) at a density of  $6 \times 10^5$  cells/mL. Each well was filled with 500 µL of cell dispersion cultured in DMEM supplemented with 10% FBS. The cells were incubated to allow for attachment and differentiate for 21~23 days. The fully differentiated cell layers were incubated with 500 µL selected RES alone and PG-RES (50:1) SD working dispersions for 2 hours. In addition, the wells treated with 500 µL HBSS (pH 6.5) served as negative (100% cell viability) control, whereas the wells incubated with 500 µL lysis buffer (10×) for 45 min served as positive control (0% cell viability). Thereafter, the plates were centrifuged ( $250 \times g$ , 3min), and supernatants (50 µL) were collected and transferred to a 96-well plate. To each well, LDH reaction mixture (50.0 µL/well)

diluted from the kit (Pierce LDH Cytotoxicity Assay Kit, Thermo Scientific) was added and mixed. The plates were further incubated in dark for another 30 min to allow for the formation of colored formazan before adding the stop solution (50.0  $\mu$ L/well). The absorbance values were measured at 490 and 680 nm by microplate reader. Percentage of cell viability was calculated from the following equation:

$$\text{Cell viability (\%)} = \left(1 - \frac{(\text{Test Solution Treatment}_{490-680} - \text{Negative Control}_{490-680})}{(\text{Positive Control}_{490-680} - \text{Negative Control}_{490-680})}\right) \times 100\%$$

Each test was performed in triplicate.

### ***Trans-epithelial permeation of RES***

For permeation study, Caco-2 cells were seeded at a density of  $6.0 \times 10^5$  cells/cm<sup>2</sup> on 12 mm i.d. transwell permeable filter inserts (polycarbonate membrane, 0.4  $\mu$ m pore size, 1.12 cm<sup>2</sup> insert membrane growth area, Corning Costar Corp. NY, USA). Experiments were conducted on the fully differentiated cells (after 21-23 days of culture). The integrity of the monolayer was routinely evaluated using transepithelial electric resistance (TEER) using a Millicell-ERS equipment (Millipore, USA).

To perform the permeation test, the culture medium of the trans-well plates was changed 12-24 h before the experiment. The filter supports and the basolateral chambers were gently rinsed twice with warm HBSS (pH 7.4, 37  $^{\circ}$ C). Thereafter, selected PG-RES SD (50:1) and RES alone working dispersions (0.5 mL/well) were added to the apical chamber, and pre-warmed HBSS (pH 7.4, 37  $^{\circ}$ C) (1.5 mL/well) was added to the basolateral compartment. The plates were incubated for 2 hours at 37  $^{\circ}$ C (95% RH, 5% CO<sub>2</sub>). Aliquots of 0.75 mL were collected from the basolateral compartment at time points of 0, 0.5, 1, 1.5 and 2 h, and replaced with equal amount of fresh HBSS buffer medium. The aliquot obtained from basolateral compartment was subjected to HPLC analysis. Each test was performed in triplicate.

#### **2.3.11 Statistical analysis**

All results were expressed as mean  $\pm$  standard deviation (n  $\geq$  3). One-way ANOVA was performed for significant difference analysis. P-value  $\leq$  0.05 was used to identify significant

differences between results using SPSS for Windows (version rel. 10.0.5, 1999, SPSS Inc., Chicago, IL, USA).

## 2.4 Results and discussion

### 2.4.1 Phytoglycogen (PG) Characterization

Figure 2.1 shows a TEM image of the phytoglycogen (PG) used in this study. The nanoparticle PG exhibited spherical and cauliflower shape with diameters ranging from 30-100 nm. Specifically, the hydrodynamic diameter of PG was  $56.40 \pm 1.51$  nm with the polydispersity index (PDI) of  $0.2 \pm 0.03$ . The weight-average molecular weight (MW) was  $1.98 \pm 0.1 \times 10^7$  g/mol, the z-average radius of gyration (RZ) value of PG was  $18.5 \pm 2.2$  nm, the dispersed molecular density ( $\rho$ ) in aqueous solution was  $3127.1 \pm 505.1$  g/mol $\cdot$ nm<sup>3</sup>, and the  $\zeta$ -potential of PG was  $-3.27 \pm 0.25$  mV.

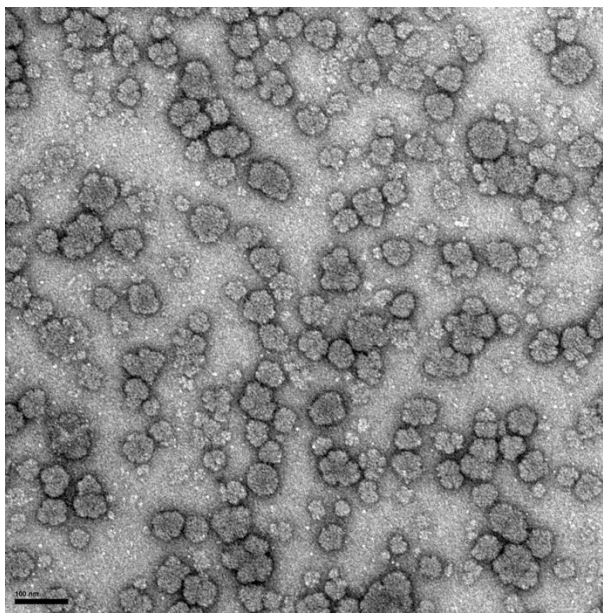


Figure 2.1 Transmission electron microscopy (TEM) image of PG (scale bar represents 100 nm)

### 2.4.2 Phase solubility of RES enhanced by PG

The phase solubility method (Higuchi & Connors, 1965) was used to quantitatively evaluate the ability of PG to dissolve RES, and the results were shown in Figure 2.3. Our findings indicated that PG significantly enhanced the RES solubility in aqueous system.

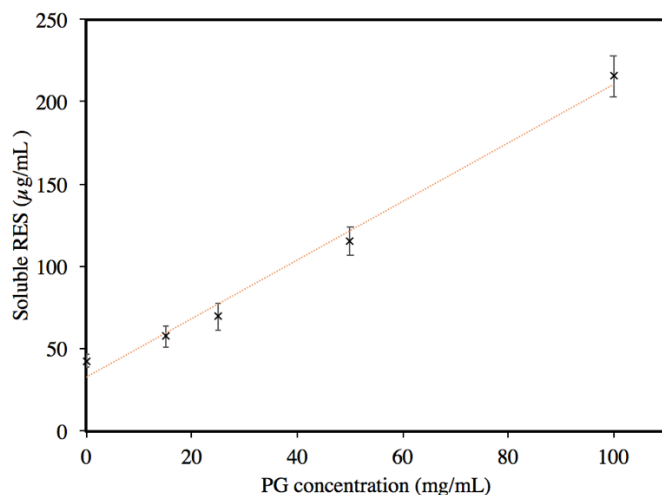


Figure 2.2 Phase solubility diagram of RES in the presence PG at 25°C. Data are expressed as mean  $\pm$  SD (n = 3)

In Figure 2.3, RES soluble amount is plotted against the PG concentration. The solubilized RES reached  $42.7 \pm 4.0$ ,  $57.6 \pm 6.6$ ,  $69.7 \pm 8.2$ ,  $115.4 \pm 8.3$  and  $215.5 \pm 12.7$   $\mu\text{g/mL}$  at PG concentration of 0, 15, 25, 50 and 100 mg/mL, respectively. The phase-solubility diagrams of RES with PG showed a linear relationship between the amount of RES solubilized and the concentration of PG, which can be classified as AL-type phase-diagram according to the definition of Higuchi and Connors (1965), indicating that PG has a strong solubilizing effect on RES. At PG concentration of 100 mg/mL, the soluble amount of RES reached 215.5  $\mu\text{g/mL}$ , which was 5.05 times that of RES alone (42.7  $\mu\text{g/mL}$ ).

### 2.4.3 Reduction of crystalline structure of RES in PG-RES SD

Figure 2.4 shows the crystallograms of RES alone, PG, PG-RES (4:1) SD, PG-RES (50:1) SD, PG:RES (4:1) PM and PG:RES (50:1) PM. For RES, intense characteristic peaks are shown at  $2\theta^\circ$  values of  $13.20^\circ$ ,  $16.40^\circ$ ,  $19.24^\circ$ ,  $20.32^\circ$ ,  $22.40^\circ$ ,  $23.60^\circ$ ,  $25.28^\circ$ , and  $28.32^\circ$ , indicating the highly crystalline nature of RES (Huang et al., 2017). In contrast, PG shows an amorphous structure due to a lack of diffraction peaks.

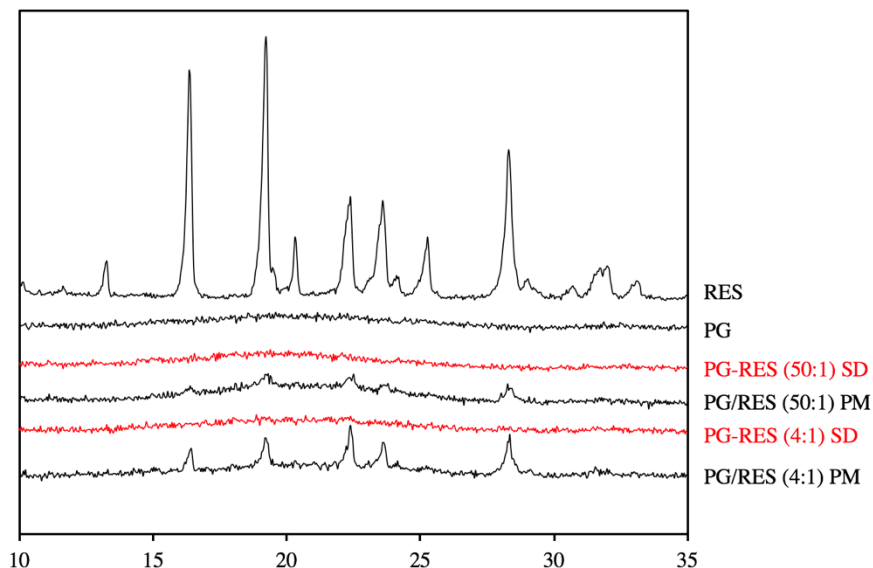


Figure 2.3 X-ray powder diffraction spectra of RES alone, PG, PG-RES (4:1) SD and PG-RES (50:1) SD, and PG:RES (4:1) PM and PG:RES (50:1) PM

The test was further conducted with RES upon PG incorporation. For PG/RES PMs, RES characteristic peaks at  $16.40^\circ$ ,  $19.24^\circ$ ,  $22.40^\circ$ ,  $23.60^\circ$ , and  $28.32^\circ$  were evident with reduced intensity in PM spectra of low ratio (4:1). These peaks were further flattened in PM of high ratio (50:1). The progressive reduction of peak intensity indicated the spectral dilution effect of PG on RES. By contrast, both PG-RES (4:1) SD and PG-RES (50:1) SD showed smooth curves (denoted in red lines in Figure 2.4), indicating the amorphous state of RES in solid dispersions due to the spray-drying processing. Specifically, compared to PG-RES (4:1) PM, the absence of the major RES diffraction peaks in PG-RES (4:1) SDs spectra suggested that spray-drying processing substantially reduced the crystalline structure of RES.

The loss of RES lattice crystalline structure in solid dispersion was due to the incorporation of RES with PG particulates and co-solvent spray-drying processing. During co-solvent mixing, RES crystallites were broken down and fully dissolved in the ethanol-water mixture. Subsequently, the RES molecules were either adsorbed onto the surface of PG particulate through H-bonds, or physically trapped within the ‘nano-pockets’ formed by glucan branches. Therefore, RES amorphous structure was retained in the highly-branched structure of PG, thereby delayed the re-crystallization of RES (Chen et al, 2015; Huang & Yao, 2011). In addition, the atomization and rapid solvent removal processes of spray-drying further reduced the crystalline structure of RES (Paudel et al., 2013; Al-Obaidi et al., 2009).

#### 2.4.4 Intermolecular Interaction between RES molecule and PG particulate

FT-IR was performed to evaluate the intermolecular interaction between RES and PG with the result shown in Figure 2.4. For RES alone, its spectrum shows a trans olefinic band at  $964.2\text{ cm}^{-1}$ . In addition, characteristic bands corresponding to C–O stretching, C–C stretching of aromatic ring, and C=C aromatic double-bond stretching are indicated at  $1382.7$ ,  $1585.2$ , and  $1604.5\text{ cm}^{-1}$ , respectively (Bertacche et al., 2006). The small band due to C-H (phenyl ring) stretching and in-plane bending of-OH are seen at  $3018\text{ cm}^{-1}$  and  $1324.8\text{ cm}^{-1}$ , respectively, and the narrow band due to phenolic-OH stretching is shown at  $3324\text{ cm}^{-1}$  (Wegiel et al., 2013).

For PG, the peaks in range  $926\text{-}1150\text{ cm}^{-1}$  represent the C–C and C–O stretching in pyranose ring, the C–O–C stretching of glycosidic bonds, and C-H bending. The broad band of O-H stretching at  $3200\text{-}3500\text{ cm}^{-1}$ , the narrow band of C–H asymmetric stretching of C6 in glucosyl units at  $2830\text{-}3000\text{ cm}^{-1}$ , and the C=O stretching of C1 at  $1640\text{ cm}^{-1}$  are also seen (Chen & Yao, 2017a, Rodriguez-Rosales & Yao, 2019). Finally, the peaks due to the scissoring vibration of  $-\text{CH}_2$  and the bending vibrations of O–C–H, C–C–H, and C–O–H are seen in the range of  $1170\text{-}1480\text{ cm}^{-1}$  (Anjos et al., 2015; Hinen, 1977).

The spectral scan was further performed with the mixture of PG and RES. As shown in Figure 2.4, the top four curves represented mixture prepared using spray-drying and physical mixing at two different PG:RES ratios (4:1 and 50:1). In general, PG-RES formulations showed similar patterns to that of native PG, and the spectral ‘masking effect’ of PG on RES enhanced with the increase of PG:RES ratio. At PG:RES ratio of 4:1, most characteristic spectral peaks of RES remain, whereas at PG:RES ratio of 50:1, the spectrum of RES are hard to be identified.

Strong intermolecular interaction, usually hydrogen bonding, between PG and RES can be observed for PG-RES SDs. RES contains three phenolic hydroxyl hydrogens that act as H-bond donor interact with the acceptor groups in PG to form hydrogen bond. As shown in Figure 2.5B, the -OH stretching band at  $3201\text{ cm}^{-1}$  in RES was slightly broadened in PG-RES PMs spectra. Moreover, this band was further flattened and shifted to  $3315$  and  $3369\text{ cm}^{-1}$  in PG-RES (4:1) SD and PG-RES (50:1) SD, respectively (Figure 2.4B), suggesting the presence of hydrogen bonding. In addition, the peak of C=O stretching of C<sub>1</sub> at  $1640\text{ cm}^{-1}$  in PG disappeared in PG-RES PMs and SDs spectra (Figure 2.4A). The changes occurred in the -OH and C=O regions indicated the hydrogen bond interaction between RES and PG, where the carbonyl group in PG served as H-

bond acceptor, and the phenolic -OH groups in RES served as the H-bond donor (Wegiel et al., 2013; Cho et al., 2014).

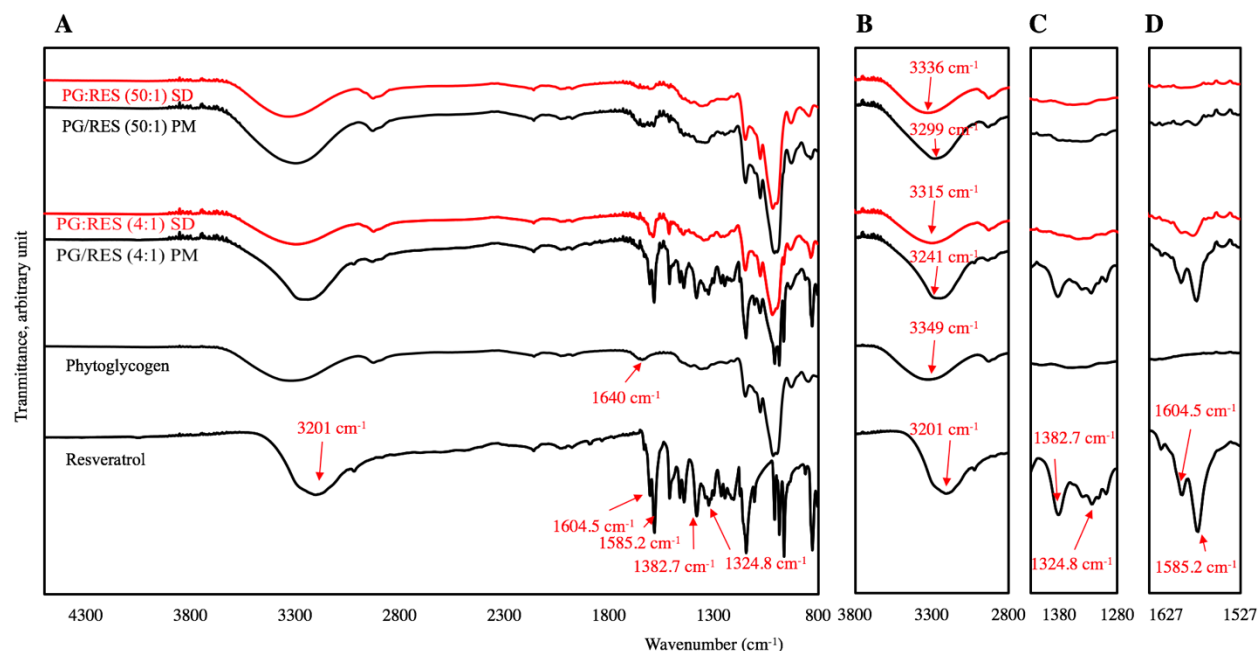


Figure 2.4 FT-IR spectra of resveratrol (RES alone), phytoglycogen (PG), PG-RES solid dispersions at PG:RES ratios of 4:1 and 50:1 (PG-RES (4:1) SD and PG-RES (50:1) SD), and PG/RES physical mixtures at PG:RES ratios of 4:1 and 50:1 (PG/RES (4:1) PM and PG/RES (50:1) PM). A, B, C and D demonstrate the spectra of 800-4500  $\text{cm}^{-1}$ , 2800-3800  $\text{cm}^{-1}$ , 1280-1430  $\text{cm}^{-1}$ , and 1527-1650  $\text{cm}^{-1}$ , respectively.

Moreover, at the PG:RES ratio of 4:1, most RES characteristic peaks are visible with PG/RES (4:1) SD. For PG-RES (4:1) SD PM, however, the spectral characteristics of RES are largely ‘masked’. For example, the band at 1382.7  $\text{cm}^{-1}$  (C–O stretching), 1324.8  $\text{cm}^{-1}$  (in-plane bending of -OH) of RES are clearly retained in PG/RES (4:1) PM but nearly invisible in the spectrum of PG-RES (50:1) SD (Figure 2.4C). In addition, the bands at 1604 and 1585  $\text{cm}^{-1}$ , originating from the vibration of C=C bond of the benzene ring, merged into one band with lower intensity in PG-RES SDs (Figure 2.4D). These changes in the spectra indicate that C–O, –OH groups, and C=C bond of the ring in RES molecule participated in the solid dispersion formation, possibly through Van der Waals interaction (Savić-Gajić et al., 2017).

#### 2.4.5 Soluble amount of resveratrol (RES) enhanced by phyto glycogen (PG)

Solubility test was conducted to determine the soluble amount of RES in RES-containing solids. The result showed that PG solubilized greater amount of RES in aqueous system. According to Figure 2.5., the inherent soluble amount of RES alone was 45.6  $\mu\text{g/mL}$ , by using PG, the soluble amount of RES was substantially increased, which followed a PG:RES ratio-dependent increase in the soluble amount of RES, reaching a highest value of 289.6  $\mu\text{g/mL}$ . In addition, for any PG:RES ratio level, solid dispersion showed much more enhanced effect than physical mixture.

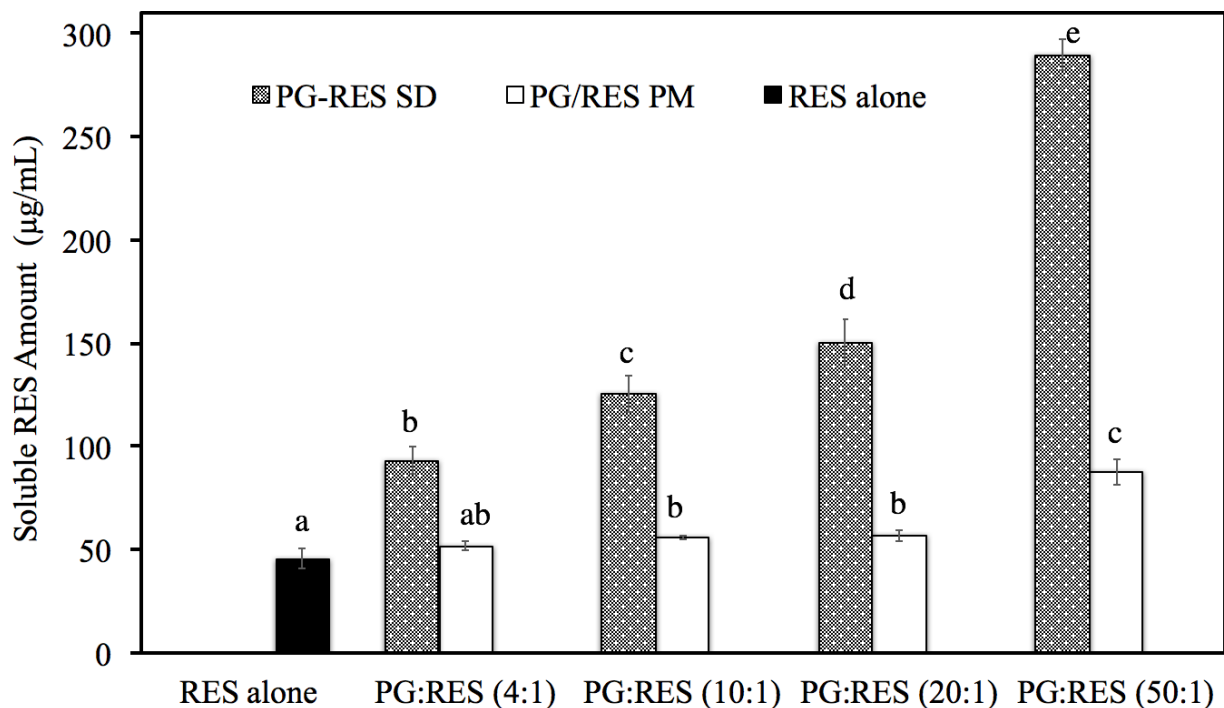


Figure 2.5 Soluble amount of RES in RES alone, PG-RES solid dispersion (SD) and PG:RES physical mixture (PM) at various PG:RES mass ratios (4:1, 10:1, 20:1 and 50:1). Soluble RES amount was determined by dispersing RES-containing solid (RES content 500  $\mu\text{g}$ ) in 1 mL DI water, the supernatant was collected and the soluble amount of RES was determined after centrifugation ( $16,000 \times g$ , 5 min.). For each type of formulation, different letters indicate statistical differences ( $p < 0.05$ ) between the mean values of RES soluble amount. Data are expressed as mean  $\pm$  SD ( $n = 3$ )

Our results suggested that PG showed great solubilizing effect on RES ( $\sim 290 \mu\text{g/mL}$  at PG:RES ratio of 50:1). Prior research showed that RES amorphous solid dispersions prepared with polymers (at a RES: polymer ratio of 1:9) carboxymethylcellulose acetate butyrate (CMCAB), hydroxypropyl methylcellulose acetate succinate (HPMCAS) and poly(vinylpyrrolidinone) (PVP),

improved RES solubility to 90  $\mu\text{g/mL}$ , 340  $\mu\text{g/mL}$  and 2500  $\mu\text{g/mL}$ , respectively (Li et al., 2013). Soy protein isolate and soluplus were only able to enhance the solubility of RES by 2~5 folds (Pujara et al., 2017; Vasconcelos et al., 2015). In addition, other key advantages of PG are its digestibility and high compatibility with biological systems, whereas synthetic polymers presented a lot of environmental and safety concerns for food product.

In this study, the effect of PG:RES ratio on the soluble amount of RES was evaluated (as shown in Figure 2.5), and the results indicated that the soluble amount of RES exhibited a PG:RES ratio-dependent manner. For example, as PG:RES ratio increased from 4:1 to 50:1, RES soluble amount progressively increased to 93.2 ~ 289.6  $\mu\text{g/mL}$  for PG-RES SD, and 51.6 ~ 87.6  $\mu\text{g/mL}$  for PG/RES PM. It has been suggested that higher amount of PG provided greater surface area that enabled the adsorption and delivery of excessive amount of RES molecules. In addition, high PG:RES ratio was also effective in inhibiting RES agglomeration/re-crystallization, which subsequently contributed to the enhanced RES soluble amount. Therefore, higher PG:RES ratio led to greater amount of solubilized RES. Based on the soluble amount test results, PG-RES (50:1) SD with the highest RES soluble amount was selected for Caco-2 permeation test.

Furthermore, Figure 2.5 showed that spray-drying processed solid dispersion exhibited significantly higher RES soluble amount compare to that of physical mixture. Depending on PG:RES ratio, PG-RES SDs prepared through spray drying increased the soluble amount of RES by 1~5 fold than that of RES alone (45.6  $\mu\text{g/mL}$ ), reaching a highest value of 289.62  $\mu\text{g/mL}$  for PG-RES (50:1) SD. In contrast, the aqueous RES soluble amount was only marginally improved by its physical mixtures, realizing a highest value of 87.55  $\mu\text{g/mL}$  for PG/RES PM (50:1).

The major advantage of solid dispersion was the generation and retention of the amorphous structure of RES. In solid dispersion, the atomization and rapid solvent removal procedures of spray-drying produced small amorphous solid particles with improved wettability (Wang, Dufour, & Zhou, 2015). In addition, the association of PG and RES through H-bonds and Van der Waals interactions further retained the amorphous structure of RES in solid dispersion. For physical mixture, the mechanical stress of physical mixing was insufficient to achieve substantial particle size reduction (Khadka et al., 2014), or the reduction of the crystalline structure of RES. Therefore, the soluble amount of RES was governed by the phase solubility of RES in the presence of PG.

#### 2.4.6 RES Caco-2 cell permeation enhanced by PG

The Caco-2 cell monolayer permeation of RES upon PG incorporation was investigated. To proceed the test, the amount of RES in RES-containing working dispersions remained soluble over 2-h incubation period was examined. RES alone working dispersions of 150 and 300 µg/mL were not fully dissolved, therefore, they were not included in further tests. The results (as shown in Table 2.1) suggested that all other RES-containing working dispersions showed no significant reduction of soluble amount of RES during the incubation period.

Table 2.1 The stability of RES-containing working solutions in cell-free HBSS media after a 2 h incubation.\*

Incubation time	RES alone <sup>1</sup>		PG-RES (50:1) SD <sup>1</sup>			
	15 µg/mL	30 µg/mL	15 µg/mL	30 µg/mL	150 µg/mL	300 µg/mL
0-h	9.73±2.41a	18.12±0.43 a	16.04±0.52 a	27.93±2.06 a	112.87±1.31 a	125.83±2.50 a
1-h	11.69±0.86 a	21.26±0.42 a	15.34±0.36 a	27.56±2.00 a	105.48±3.89 a	122.65±3.90 a
2-h	15.92±0.66 b	21.65±8.09 a	16.11±0.40 a	30.76±1.25 b	112.79±3.95 a	129.27±0.85 a

\*The stability of RES-containing working dispersions were determined by the soluble amount of RES in the tested working dispersions in cell-free HBSS media (pH 6.5, 37H, culture medium condition) at 0, 1 and 2-hour incubation time.

<sup>1</sup> Values are expressed as soluble amount of RES ± SD (n=3). Significant differences within RES alone group or PG-RES (50:1) SD group are denoted by different letters (p < 0.05).

In addition, the RES-containing working dispersions were evaluated for their cytotoxicity effects on Caco-2 cells using LDH assay. It was observed that the cytotoxicity effect of RES was in dose-dependent manner (as shown Table 2.2). Among the tested working dispersions, RES alone and PG-RES (50:1) SD working dispersions of 15 and 30 µg/mL showed cell viability above 97%, and PG-RES (50:1) SD containing RES amount of 150 µg/mL displayed 92% cell viability. In contrast, PG-RES (50:1) SD containing RES amount of 300 µg/mL showed cell viability of 83%. To ensure the integrity of Caco-2 cell monolayer, PG-RES (50:1) SD 300 µg/mL was not included for further test. Based on the results of stability and cytotoxicity tests, RES alone 15 and 30 µg/mL, PG-RES (50:1) SD 15, 30, and 150 µg/mL working dispersions were selected for permeation test.

Table 2.2 Cell viability results of RES alone and PG-RES (50:1) SD with Caco-2 cells determined using the LDH assay.

RES Concentration ( $\mu\text{g/mL}$ )	Cell viability (%) <sup>*</sup>	
	RES alone <sup>1</sup>	PG-RES (50:1) SD <sup>1</sup>
15	99.59 $\pm$ 1.38 a	98.60 $\pm$ 0.60 a
30	97.17 $\pm$ 1.00 a	97.33 $\pm$ 0.55 a
150		91.89 $\pm$ 1.78 b
300		83.59 $\pm$ 0.24 c

<sup>\*</sup>Percentage of survived cells was obtained after 2 h incubation with various RES working dispersions in HBSS at 37°C.

<sup>1</sup> Values are expressed as % cell viability  $\pm$  SD (n=3). Significant differences within RES alone group or PG-RES (50:1) SD group are denoted by different letters ( $p < 0.05$ ). No significant difference of cell viability is found among RES alone treated Caco-2 cell monolayer.

The results for cumulative Caco-2 monolayer membrane permeation of RES in RES alone and PG-RES (50:1) SD at various loading concentrations were displayed in Figure 2.6. The findings showed that both RES alone and PG-RES (50:1) SD showed a loading concentration-dependent increase in permeation; where PG-RES (50:1) SD achieved higher permeation amount of RES compared to that of RES alone during 2-hour incubation period.

At low loading amount of RES, 15 (7.5  $\mu\text{g/well}$ ) and 30  $\mu\text{g/mL}$  (15  $\mu\text{g/well}$ ) (Figure 2.6), PG-RES (50:1) SD showed higher RES permeation amount than that of RES alone. For example, at 15  $\mu\text{g/mL}$  does, the permeation amount was 0.43  $\mu\text{g/well}$  for PG-RES (50:1) SD, and 0.25  $\mu\text{g/well}$  (3.34%) for RES alone, respectively; indicating that PG-RES (50:1) SD improved the permeation amount of RES by 72%. At 30  $\mu\text{g/mL}$  does level, the permeation amount for PG-RES (50:1) SD and RES alone was 0.91  $\mu\text{g/well}$  (5.80%), and 0.71  $\mu\text{g/well}$  (6.10%), respectively; PG-RES (50:1) SD improved the permeation amount of RES by 29.6%.

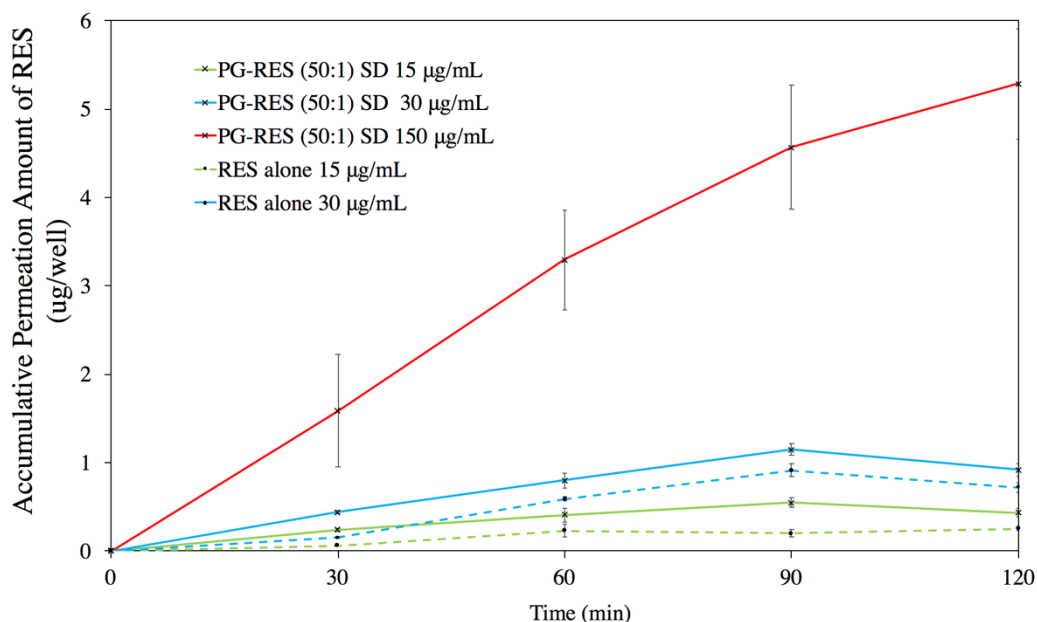


Figure 2.6 Cumulative RES permeations across the Caco-2 monolayers of RES alone and PG-RES (50:1) SD at different apical RES loading concentrations over 2-hour incubation. Blue and green lines represented the permeation of loading amount of RES  $C_{RES}=15 \mu\text{g/mL}$  ( $7.5 \mu\text{g/well}$  of RES), and  $30 \mu\text{g/mL}$  ( $15 \mu\text{g/well}$  of RES), respectively; red line represents the permeation of loading amount of RES  $C_{RES}=150 \mu\text{g/mL}$  ( $75 \mu\text{g/well}$  of RES). Solid line represents PG-RES (50:1) SD, and dashed line represents RES alone. Data was expressed as mean  $\pm$  SD ( $n = 3$ )

The increased permeation of RES for PG-RES (50:1) SD working dispersion indicated that RES molecules were effectively released from PG nanoparticles. Furthermore, the incorporation of RES increased the hydrophobicity of PG nanoparticles due to the lipophilic nature of resveratrol (Log P of RES is 3.1), therefore, enhanced its interaction with the cell monolayer membrane (Robinson et al., 2015). In addition, the distance between RES molecules and apical cell membrane was shorter for PG-RES (50:1) SD compared with RES alone due to the increased hydrophobicity. The reduced travel distance, and the enhanced RES-cell monolayer interaction would increase the local concentration of RES near the apical side of the cell monolayer, and the apical-to-basolateral concentration gradient of RES was enhanced accordingly. Therefore, PG-RES (50:1) SD generated a greater Caco-2 cell monolayer permeation of RES compared to RES alone.

At high loading amount of RES ( $150 \mu\text{g/mL}$ ,  $75 \mu\text{g/well}$ ), the permeation of RES was  $5.43 \mu\text{g/well}$  (7.24%) for PG-RES (50:1) SD, while RES alone formed white crystalline. The low intrinsic solubility of RES in RES alone limited its loading and permeation amount. In addition, the undissolved RES crystals were inaccessible to the monolayer, and led to cell damage (Szurman

et al., 2006). In contrast, the association between RES and PG nanoparticles in PG-RES (50:1) SD created and maintained the supersaturated state of RES in aqueous system, thereby, prevented the re-crystallization of RES and monolayer injuries.

To explain the enhanced permeation of PG-RES (50:1) SD at high loading amount of RES (150 µg/mL, 75 µg/well), two mechanisms were proposed: 1). PG increased total soluble amount of RES in the apical chamber and generated a high apical-to-basolateral concentration gradient, thereby, enhanced the paracellular permeation (passive diffusion) of RES molecules (Maier-Salamon et al., 2006; Henry et al., 2005; Murota et al., 2002); and 2). in Caco-2 permeation test, only 'free' RES molecule, which was unbound to the carrier but remain soluble, was able to permeate the membrane (Alex et al., 2015; Miller & Dahan., 2012; Miller et a., 2011; Dahan et al., 2013). Therefore, only small amount of 'free' RES was available for transport due to its limited intrinsic solubility (as shown in Figure 2.7). In this study, at high loading content, most RES molecules were adsorbed on to PG particles, not readily permeable. Once the 'free' RES was transported across the membrane and depleted from the apical chamber, the PG adsorbed RES molecules were gradually released to replenish the 'free' RES supply (as shown in Figure 2.7). In addition, the degradation of PG promoted the release of RES. Therefore, PG-RES (50:1) SD achieved a successful release of RES and increased the cumulative amount of 'free' RES molecules that were available for transport over time, thus enabling greater permeation amount (Meuer et al., 2009).

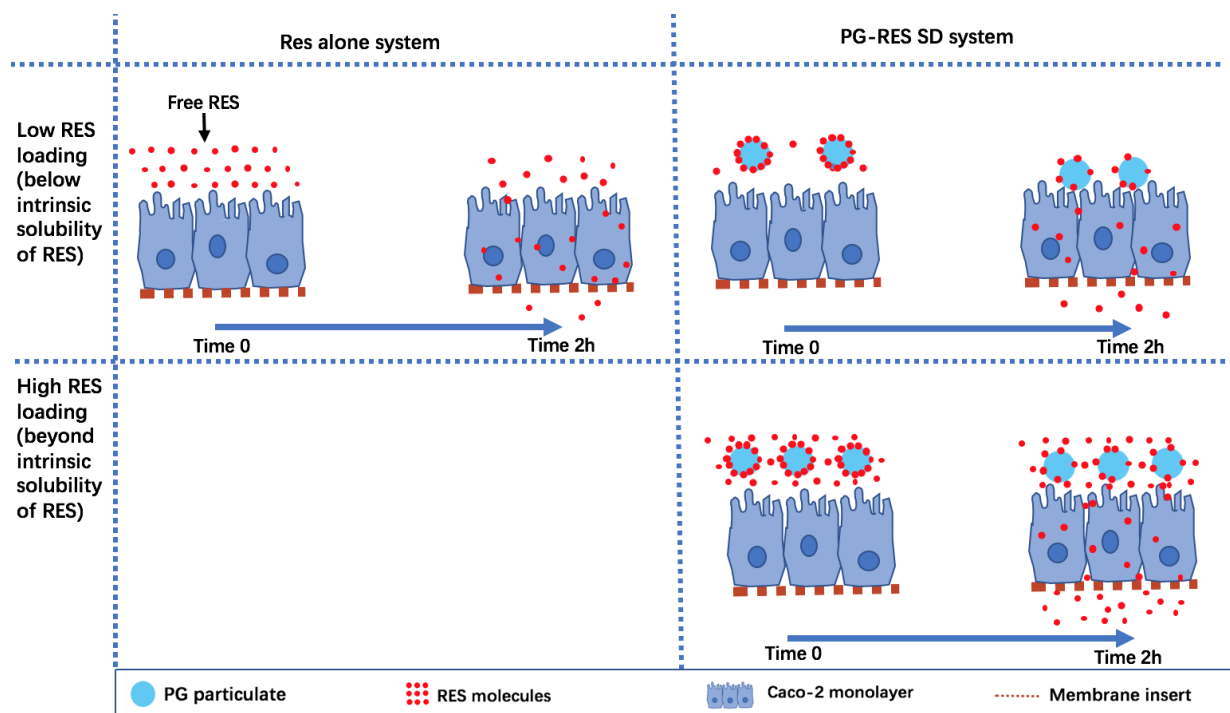


Figure 2.7 Schematic of RES alone (left) and PG-RES SD (right) Caco-2 monolayer permeation mechanisms at low RES loading amount (below intrinsic solubility of RES, upper) and high RES loading amount (lower). Only ‘free’ RES molecules (soluble and unbounded RES) can permeate the cell monolayer. After ‘free’ RES is depleted from the donor chamber, the adsorbed RES molecules are desorbed to replenish the depleted ‘free’ RES continuously to achieve a gradual permeation over time

Recent reports showed that nanostructured lipid carriers (NLCs), solid lipid nanoparticles (SLNs) only realized 1.18~1.375-fold of RES permeation than that of RES alone at loading concentration of 2.3  $\mu\text{g/mL}$  (Neves et al., 2016). Mesoporous silica nanoparticles (MSN, 20% RES loading) reached a 3-fold of permeation compare to RES alone (with loading concentrations below 20  $\mu\text{g/mL}$ ), however, high loading does was unachievable due to the limited solubility of MSN incorporated RES formulation ( $\sim 70 \mu\text{g/mL}$ ) (Juèrè et al., 2017). Compared with previous studies, our investigation revealed that PG-RES SD had great potential in improving the *in-vitro* bioavailability of RES.

## 2.5 Conclusion

The current work revealed that phytoglycogen (PG) showed promising performance in improving RES soluble amount and Caco-2 cell monolayer permeation. The highly-branched

dendritic structure of PG allowed the adsorption and stabilization of RES molecules onto and within the PG particulate, thus enhanced the aqueous soluble amount of RES. The use of spray-drying further enhanced the performance of PG-RES formulation, due to the reduced particle size and increased wettability. The ratio of PG:RES was another major factor that affected RES soluble amount; the highest PG:RES ratio (50:1) of solid dispersion realized the highest soluble amount of RES (289.62  $\mu\text{g}/\text{mL}$ ), which was 2.1 times higher than that of the lowest PG:RES ratio (4:1). FT-IR spectra showed that the PG interacted with RES through H-bonds formed between RES and PG hydroxyl groups. X-ray powder diffraction confirmed the reduced crystallinity of RES upon PG incorporation. In Caco-2 permeation model, PG solid dispersion achieved a successful release of RES, and realized a significant increase in total soluble RES amount during 2-h incubation period, which led to increased cumulative permeation over time. This study showed that PG, a naturally-occurring, biodegradable and digestible polysaccharides, is a potent delivery agent to enhance the nutritional profile of RES-containing foods through increasing the *in-vitro* efficacies of RES.

## 2.6 Reference

- Alex, A., Harris, C. J., & Smith, D. A. (2015). *Attrition in the pharmaceutical industry: reasons, implications, and pathways forward*. John Wiley & Sons.
- Al-Obaidi, H., Brocchini, S., & Buckton, G. (2009). Anomalous properties of spray dried solid dispersions. *Journal of pharmaceutical sciences*, 98(12), 4724-4737.
- Anjos, O., M. G. Campos, P. C. Ruiz & P. Antunes (2015) Application of FT-IR-ATR spectroscopy to the quantification of sugar in honey. *Food Chemistry*, 169, 218-223.
- Atanacković, M., Poša, M., Heinle, H., Gojković-Bukarica, L., & Cvejić, J. (2009). Solubilization of resveratrol in micellar solutions of different bile acids. *Colloids and Surfaces B: Biointerfaces*, 72(1), 148-154.
- Bertacche, V., Lorenzi, N., Nava, D., Pini, E., & Sinico, C. (2006). Host-guest interaction study of resveratrol with natural and modified cyclodextrins. *Journal of inclusion phenomena and macrocyclic chemistry*, 55(3-4), 279-287.
- Bradamante, S., Barenghi, L., & Villa, A. (2004). Cardiovascular protective effects of resveratrol. *Cardiovascular drug reviews*, 22(3), 169-188.

- Chen, H., & Yao, Y. (2017). Phytoglycogen improves the water solubility and Caco-2 monolayer permeation of quercetin. *Food chemistry*, 221, 248-257.
- Chen, H., & Yao, Y. (2017a) Phytoglycogen to increase lutein solubility and its permeation through Caco-2 monolayer. *Food Research International*, 97, 258-264. *Food Research International*, 97, 258-264.
- Chen, H., Narsimhan, G., & Yao, Y. (2015). Particulate structure of phytoglycogen studied using  $\beta$ -amylolysis. *Carbohydrate polymers*, 132, 582-588.
- Cho, A. R., Chun, Y. G., Kim, B. K., & Park, D. J. (2014). Preparation of alginate–CaCl<sub>2</sub> microspheres as resveratrol carriers. *Journal of Materials Science*, 49(13), 4612-4619.
- Dahan, A., Beig, A., Ioffe-Dahan, V., Agbaria, R., & Miller, J. M. (2013). The twofold advantage of the amorphous form as an oral drug delivery practice for lipophilic compounds: increased apparent solubility and drug flux through the intestinal membrane. *The AAPS journal*, 15(2), 347-353.
- Das, D. K., & Maulik, N. (2006). RES in cardioprotection: a therapeutic promise of alternative medicine. *Molecular interventions*, 6(1), 36.
- Davidov-Pardo, G., & McClements, D. J. (2014). RES encapsulation: designing delivery systems to overcome solubility, stability and bioavailability issues. *Trends in food science & technology*, 38(2), 88-103.
- Devi, P., Sharma, P., Rathore, C., & Negi, P. (2019). Novel Drug Delivery Systems of RES to Bioavailability and Therapeutic Effects. In *RES-Adding Life to Years, Not Adding Years to Life*. IntechOpen.
- Gadalla, H. H., Soliman, G. M., Mohammed, F. A., & El-Sayed, A. M. (2016). Development and in vitro/in vivo evaluation of Zn-pectinate microparticles reinforced with chitosan for the colonic delivery of progesterone. *Drug delivery*, 23(7), 2541-2554.
- Gambini, J., Inglés, M., Olaso, G., Lopez-Grueso, R., Bonet-Costa, V., Gimeno-Mallench, L., Mas-Bargues, C., Abdelaziz, K.M., Gomez-Cabrera, M. C., Vina, J., & Borrás, C. (2015). Properties of resveratrol: in vitro and in vivo studies about metabolism, bioavailability, and biological effects in animal models and humans. *Oxidative medicine and cellular longevity*, 2015.

- Gumireddy, A., Christman, R., Kumari, D., Tiwari, A., North, E. J., & Chauhan, H. (2019). Preparation, characterization, and in vitro evaluation of Curcumin-and resveratrol-loaded solid lipid nanoparticles. *AAPS PharmSciTech*, 20(4), 145.
- Hemar, Y., Cheng, L. J., Oliver, C. M., Sanguansri, L., & Augustin, M. (2010). Encapsulation of resveratrol using water-in-oil-in-water double emulsions. *Food Biophysics*, 5(2), 120-127.
- Henry, C., Vitrac, X., Decendit, A., Ennamany, R., Krisa, S., & Mérillon, J. M. (2005). Cellular uptake and efflux of trans-piceid and its aglycone trans-resveratrol on the apical membrane of human intestinal Caco-2 cells. *Journal of agricultural and food chemistry*, 53(3), 798-803.
- Higuchi, T., & Connors, K. A. (1965). Phase-solubility techniques. *Advance in Analytical Chemistry and Instrumentation*, 4, 117–212.
- Hineno, M. (1977). Infrared spectra and normal vibration of  $\beta$ -d-glucopyranose. *Carbohydrate Research*, 56(2), 219-227.
- Huang, L., & Yao, Y. (2011). Particulate structure of phytoglycogen nanoparticles probed using amyloglucosidase. *Carbohydrate Polymers*, 83, 1665–1671.
- Huang, M., Liang, C., Tan, C., Huang, S., Ying, R., Wang, Y., ... & Zhang, Y. (2019). Liposome co-encapsulation as a strategy for the delivery of curcumin and resveratrol. *Food & function*, 10(10), 6447-6458.
- Huang, X., Dai, Y., Cai, J., Zhong, N., Xiao, H., McClements, D. J., & Hu, K. (2017). RES encapsulation in core-shell biopolymer nanoparticles: Impact on antioxidant and anticancer activities. *Food Hydrocolloids*, 64, 157-165.
- James, M. G., Robertson, D. S., & Myers, A. M. (1995). Characterization of the maize gene sugary1, a determinant of starch composition in kernels. *The Plant Cell*, 7(4), 417-429.
- Juère, E., Florek, J., Bouchoucha, M., Jambhrunkar, S., Wong, K. Y., Popat, A., & Kleitz, F. (2017). In vitro dissolution, cellular membrane permeability, and anti-inflammatory response of resveratrol-encapsulated mesoporous silica nanoparticles. *Molecular Pharmaceutics*, 14(12), 4431-4441.
- Khadka, P., Ro, J., Kim, H., Kim, I., Kim, J. T., Kim, H., Cho, J. M., Yun, G., & Lee, J. (2014). Pharmaceutical particle technologies: An approach to improve drug solubility, dissolution and bioavailability. *Asian journal of pharmaceutical sciences*, 9(6), 304-316.

- la Porte, C., Voduc, N., Zhang, G., Seguin, I., Tardiff, D., Singhal, N., & Cameron, D. W. (2010). Steady-state pharmacokinetics and tolerability of trans-RES 2000mg twice daily with food, quercetin and alcohol (ethanol) in healthy human subjects. *Clinical pharmacokinetics*, 49(7), 449-454.
- Li, B., Wegiel, L. A., Taylor, L. S., & Edgar, K. J. (2013). Stability and solution concentration enhancement of resveratrol by solid dispersion in cellulose derivative matrices. *Cellulose*, 20(3), 1249-1260.
- Lu, Z., Cheng, B., Hu, Y., Zhang, Y., & Zou, G. (2009). Complexation of resveratrol with cyclodextrins: solubility and antioxidant activity. *Food chemistry*, 113(1), 17-20.
- Lucas-Abellán, C., Fortea, I., López-Nicolás, J. M., & Núñez-Delicado, E. (2007). Cyclodextrins as resveratrol carrier system. *Food chemistry*, 104(1), 39-44.
- Maier-Salamon, A., Hagenauer, B., Wirth, M., Gabor, F., Szekeres, T., & Jäger, W. (2006). Increased transport of resveratrol across monolayers of the human intestinal Caco-2 cells is mediated by inhibition and saturation of metabolites. *Pharmaceutical research*, 23(9), 2107-2115.
- Meuer, S., Braun, L., Schilling, T., & Zentel, R. (2009).  $\alpha$ -Pyrene polymer functionalized multiwalled carbon nanotubes: Solubility, stability and depletion phenomena. *Polymer*, 50(1), 154-160.
- Miller, J. M., & Dahan, A. (2012). Predicting the solubility–permeability interplay when using cyclodextrins in solubility-enabling formulations: model validation. *International journal of pharmaceuticals*, 430(1-2), 388-391.
- Miller, J. M., Beig, A., Krieg, B. J., Carr, R. A., Borchardt, T. B., Amidon, G. E., Amidon, G. L., & Dahan, A. (2011). The solubility–permeability interplay: mechanistic modeling and predictive application of the impact of micellar solubilization on intestinal permeation. *Molecular pharmaceuticals*, 8(5), 1848-1856.
- Murcia, M. A., & Martinez-Tome, M. (2001). Antioxidant activity of RES compared with common food additives. *Journal of food protection*, 64(3), 379-384.
- Murota, K., Shimizu, S., Miyamoto, S., Izumi, T., Obata, A., Kikuchi, M., & Terao, J. (2002). Unique uptake and transport of isoflavone aglycones by human intestinal Caco-2 cells: comparison of isoflavonoids and flavonoids. *The Journal of nutrition*, 132(7), 1956-1961.

- Neves, A. R., Martins, S., Segundo, M. A., & Reis, S. (2016). Nanoscale delivery of resveratrol towards enhancement of supplements and nutraceuticals. *Nutrients*, 8(3), 131.
- Paudel, A., Worku, Z. A., Meeus, J., Guns, S., & Van den Mooter, G. (2013). Manufacturing of solid dispersions of poorly water soluble drugs by spray-drying: formulation and process considerations. *International journal of pharmaceutics*, 453(1), 253-284.
- Pujara, N., Jambhrunkar, S., Wong, K. Y., McGuckin, M., & Papat, A. (2017). Enhanced colloidal stability, solubility and rapid dissolution of resveratrol by nanocomplexation with soy protein isolate. *Journal of Colloid and Interface Science*, 488, 303-308.
- Robinson, K., Mock, C., & Liang, D. (2015). Pre-formulation studies of resveratrol. *Drug development and industrial pharmacy*, 41(9), 1464-1469.
- Rodriguez-Rosales, R. J., & Yao, Y. (2019). Phytoglycogen, a natural dendrimer-like glucan, improves the soluble amount and Caco-2 monolayer permeation of curcumin and enhances its efficacy to reduce HeLa cell viability. *Food Hydrocolloids*, 105442.
- Savić-Gajić, I., Savić, I. M., Nikolić, V. D., Nikolić, L. B., Popsavin, M. M., & Rakić, S. J. (2017). The improvement of photostability and antioxidant activity of trans-resveratrol by cyclodextrins. *Advanced Technologies*, 6(2), 18-25.
- Scheffler SL, Huang L, Bi L, Yao Y. (2010). In vitro digestibility and emulsification properties of phytoglycogen octenyl succinate. *Journal of agricultural and food chemistry*, 58(8), 5140-5146.
- Sessa, M., Balestrieri, M.L., Ferrari, G., Servillo, L., Castaldo, D., D'Onofrio, N., Donsì, F. and Tsao, R. (2014). Bioavailability of encapsulated RES into nanoemulsion-based delivery systems. *Food chemistry*, 147, 42-50.
- Shi, G., Rao, L., Yu, H., Xiang, H., Yang, H., & Ji, R. (2008). Stabilization and encapsulation of photosensitive RES within yeast cell. *International Journal of Pharmaceutics*, 349(1-2), 83-93.
- Singh, A. P., Singh, R., Verma, S. S., Rai, V., Kaschula, C. H., Maiti, P., & Gupta, S. C. (2019). Health benefits of resveratrol: Evidence from clinical studies. *Medicinal Research Reviews*, 39(5), 1851-1891.

- Szurman, P., Kaczmarek, R., Spitzer, M. S., Jaissle, G. B., Decker, P., Grisanti, S., Henke-Fahle, S., Aisenbrey, S., & Bartz-Schmidt, K. U. (2006). Differential toxic effect of dissolved triamcinolone and its crystalline deposits on cultured human retinal pigment epithelium (ARPE19) cells. *Experimental eye research*, 83(3), 584-592.
- Tang, H., Xiang, S., Li, X., Zhou, J., & Kuang, C. (2019). Preparation and in vitro performance evaluation of resveratrol for oral self-microemulsion. *PloS one*, 14(4), e0214544.
- ter Ellen, B. M., Kumar, N. D., Bouma, E. M., Troost, B., van de Pol, D. P. I., van der Ende-Metselaar, H. H., ... & van der Voort, P. H. J. (2020). Resveratrol and pterostilbene potentially inhibit SARS-CoV-2 infection in vitro. *bioRxiv*.
- Vasconcelos, T., Marques, S., & Sarmiento, B. (2015). Development of a resveratrol solid dispersion with soluplus®. In *2nd Annual Meeting & Exposition of the Controlled Release Society Edinburgh, Scotland*.
- Wang, W., Dufour, C., & Zhou, W. (2015). Impacts of spray-drying conditions on the physicochemical properties of soy sauce powders using maltodextrin as auxiliary drying carrier. *CyTA-Journal of Food*, 13(4), 548-555.
- Wegiel, L. A., Mauer, L. J., Edgar, K. J., & Taylor, L. S. (2013). Crystallization of amorphous solid dispersions of resveratrol during preparation and storage—Impact of different polymers. *Journal of pharmaceutical sciences*, 102(1), 171-184.

## CHAPTER 3. OCTENYLSUCCINATE HYDROXYPROPYL PHYTOGLYCOGEN TO ENHANCE THE SOLUBILITY AND *IN-VITRO* EFFICACIES OF GRISEOFULVIN

### 3.1 Abstract

The study demonstrated the capability of octenylsuccinate hydroxypropyl phytyglycogen (OHPP) to improve the water soluble amount of griseofulvin (Gris). Gris-OHPP SD was prepared by incorporating Gris with OHPP at the weight ratio of 1/4. The soluble amount of Gris in Gris-OHPP SD was 854.6  $\mu\text{g/mL}$ , which was 22 times higher than that of pure Gris (37.7  $\mu\text{g/mL}$ ). There was hydrogen-bonding formed between Gris and OHPP as shown by FT-IR spectra. Depending on the amount of Gris loading in apical compartment, the percentage of permeated Gris of Gris-OHPP SD was 2.2~3 times higher than that of pure Gris. The *in-vitro* antifungal susceptibility tests demonstrated Gris of Gris-OHPP SD inhibited the growth of *Trichophyton rubrum*, which confirmed that Gris of Gris-OHPP was bioactive and available to exert its biofunction.

### 3.2 Introduction

Griseofulvin (Gris,  $\text{C}_{17}\text{H}_{17}\text{ClO}_6$ , molecular weight: 352.77 g/mol) is a colorless and neutral antifungal drug isolated from *Penicillium* (Ong et al., 2016). A number of studies show that Gris works effectively against mold infections caused by *Microsporum*, *Epidermophyton* and *Trichophyton*, and is commonly used to treat skin and nail infections, such as, ringworm, athlete's foot, and jock itch (Petersen et al., 2014). According to the Biopharmaceutics Classification System (BCS), Gris belongs to BCS class II drug, which is poorly water-soluble but gastrointestinal permeable. The bioavailability and gastrointestinal absorption of Gris was limited by its insoluble nature when administrated orally.

Over the past decades, various approaches have been proposed to improve the solubility and dissolution profile of Gris for its enhanced bioavailability, e.g., Nanoformulation (e.g. milling, high pressure homogenization), self-emulsifying drug delivery system (Zadeha et al., 2017), inclusion complex (Hbaieb et al., 2012), mesoporous silicas (Jambhrunkar et al., 2014), or HPMCAS (Al-Obaidi & Buckton, 2009), liposomes (Ong et al., 2016), SD (Wani et al., 2020), and microemulsions (Iradhati et al., 2017) systems. Although these technics are efficient for the

delivery of Gris, they are suffered from varying factors, such as high variation in particle size, high cost of materials, nanoparticle accumulations in organ, low stabilities, toxicity, or low loading capacity.

Octenylsuccinate hydroxypropyl phytoglycogen (OHPP), an amphiphilic nano-polymer prepared by substituting PG with hydroxypropyl group and octenylsuccinate (OS) group, is an effective carrier system that provides another pathway to enhance the solubility of water insoluble drugs. In previous studies, OHPP has been successfully applied to improve the solubility of many water insoluble drugs by 3-4 orders of magnitudes (Xie & Yao, 2018). However, the intermolecular interaction, and bioavailability of the incorporated drugs remained unknown.

In this study, we reported the feasibility of using OHPP to enable or enhance in-vitro efficacies of Gris in aqueous system. The hypothesis is that OHPP nanoparticle enhanced the soluble amount of Gris in water, and therefore improved the *in-vitro* bio-efficacy of Gris.

### **3.3 Materials and Methods**

#### **3.3.1 Chemicals**

Gris was purchased from Sigma-Aldrich (Portland, OR). All other chemicals were of reagent grade. Double-distilled water was freshly prepared whenever required. *Trichophyton rubrum* ATCC MYA-4438 was purchased from ATCC (Rockville, MD).

#### **3.3.2 Preparation and characterization of octenylsuccinate hydroxypropyl phytoglycogen (OHPP) and Gris-OHPP solid dispersion (SD)**

To prepare octenylsuccinate hydroxypropyl phytoglycogen (OHPP), 70 g of PG was suspended in DI water to form 18% (w/w) dispersion. The extraction of phytoglycogen (PG) was performed according to the method described by Chen and Yao (2017). Sodium hydroxide was added to PG dispersion to reach the concentration of 5.9% (w/w). The mixture was heated at boiling temperature for 1 h before transferred to the high-pressure reactor. Thereafter, 350 mL propylene oxide (PO) was added to the PG dispersion at the speed of 0.59 mL/min. The reaction was carried out at 40 °C for 24 h, and terminated by neutralization. Afterwards, the mixture was ultra-filtrated and adjusted to pH 8.5 ~ 9.0, followed by octenyl succinic anhydride (OSA) addition at 1:1 ratio (OSA: glucosyl units of PG). The OSA reaction was maintained at pH 8.5-9.0, 40 °C

for 24 h, and terminated by reducing the pH to 6.5. The resulting dispersion was ultra-filtrated and subjected to spray-drying. The dry material collected was octenylsuccinate hydroxypropyl phytoglycogen (OHPP).

The characterization of OHPP was conducted by measuring the weight average molecular weight ( $M_w$ ), z-average root means square radius ( $R_z$ ), molecular density ( $\rho$ ), and  $\zeta$ -potential of OHPP according to the method described by Xie and Yao (2018).

The Gris-OHPP solid dispersion (SD) was prepared by using a proprietary approach at a ratio of Gris: OHPP at 1:4. The physical mixture of Gris-OHPP was prepared by blending and mixture using mortar and pestle. The intermolecular interaction between Gris and OHPP in Gris-containing solids was characterized by FT-IR following the procedure described by Chen and Yao (2017).

### **3.3.3 *In-vitro* efficacy tests of Gris-OHPP SD (separate the tests)**

To investigate the *in-vitro* efficacies of Gris in Gris-OHPP SD, three-step experiment was conducted to measure Gris soluble amount, Caco-2 trans-epithelial permeation and anti-fungal activity. At first, the soluble amount of Gris measurement was conducted by dispersing 15 mg of Gris-containing solid (pure Gris and Gris-OHPP SD) in 1.0 mL DI water, and equilibrating for 24 h at 25 °C. Thereafter, the resulting dispersion was centrifuged ( $16,000 \times g$ , 5 min), and 0.2 mL supernatant was withdrawn before subjected to Gris content analysis using HPLC. The soluble amount of Gris was defined as the Gris content in the supernatant.

The Caco-2 trans-epithelial permeation of Gris was determined. The culturing and the monolayer development of Caco-2 BBE cells (ATCC, Rockville, MD) was performed by the method introduced in Rodriguez-Rosales & Yao (2020). The passages of Caco-2 cells were in the range of 90-102. To perform permeation test, pure Gris and Gris-OHPP SD test dispersions (0.5 mL) with soluble Gris content of 34  $\mu\text{g/mL}$  and 20  $\mu\text{g/mL}$  were prepared and applied to the apical side of the monolayer. The basolateral chamber was filled with 1.5 mL of HBSS (pH 7.4). The plates were incubated for 2 hours at 37 °C with 5% CO<sub>2</sub> and 95% air at 95% RH. At predetermined time intervals (0, 30, 60, 90 and 120 min), an aliquot of 0.75 mL was withdrawn from the basolateral side, and replaced with 0.75mL fresh HBSS (pH 7.4). The samples collected

from basolateral compartment were subjected to Gris content analysis using HPLC. Each test was performed in triplicate.

At last, the antifungal efficacy of pure Gris and Gris-OHPP SD were evaluated against *Trichophyton rubrum* ATCC MYA-4438, and the test procedures followed CLSI M38-A protocol (Santos & Hamdan, 2005). Briefly, pure Gris and Gris-OHPP SD were dissolved and serially diluted in RPMI 1640 to yield a series of working dispersions with Gris concentration ranging from 0.0626 to 16 µg/mL. To prepare the fungal inoculum, *T. rubrum* was cultured on potato dextrose agar (Sigma-Aldrich) for 7 days at 28 °C for optimal sporulation. To harvest the conidia and hyphal fragments, the fungal colonies were covered with 5 ml of sterile saline solution (0.9%), and scraped with the tip of Pasteur pipette. Thereafter, the conidium suspension was filtered, and the filtrate suspension was adjusted to a transmittance level of 70 to 72% using a spectrophotometer at wavelength of 520 nm, followed by 1:50 dilution in RPMI 1640. The anti-fungal test was performed by incubating 100 µL *T. rubrum* diluted inoculum and 100 µL Gris working dispersion in a 96-well microplate. The growth medium and drug free *T. rubrum* inoculum suspension served as growth and sterility controls, respectively. The MIC50 and MIC90 were obtained by visual reading after 7 days of incubation. MIC50 and MIC90 were defined as the lowest concentration showing 50, and 90 % growth inhibition, respectively. All tests were performed in triplicate.

### 3.3.4 Statistical Analysis

All experiments were performed in triplicate. Results were expressed as mean ± standard deviation. One-way ANOVA was used to analyze the differences between the mean values.  $P < 0.05$  was considered as statistically significant.

## 3.4 Results and Discussion

### 3.4.1 Characterization of OHPP and Gris-OHPP solid dispersion

Physical and chemical properties of OHPP and the proposed chemical interaction between Gris and OHPP in Gris-OHPP solid dispersion was examined. Regarding the basic structural properties of OHPP, the results showed that the  $M_w$  of OHPP was  $1.70 \pm 0.7 \times 10^7$  g/mol, the Z-average root square radius ( $R_z$ ) was 22.6nm, and the molecular density was 1312.6 g/mol nm<sup>3</sup>. It is found that the DS of OSA in OHPP reached 0.285 (± 0.01) and the MS of hydroxypropyl groups

in OHPP was  $2.43 (\pm 0.01)$ . For zeta-potentials, moreover, OHPP ( $-24.4 \pm 0.52$  mV) showed a relative high density of negative charge compared to that of native PG ( $-3.37 \pm 0.49$  mV) due to the introduction of OS groups.

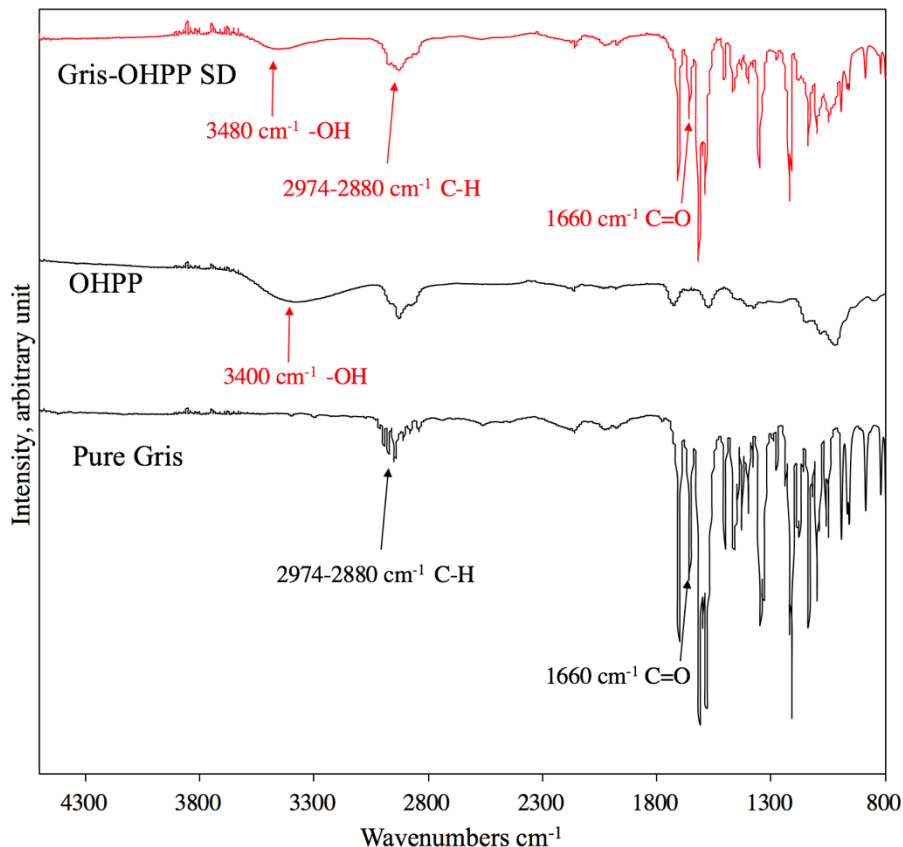


Figure 3.1 FT-IR spectra of pure Gris, OHPP, and Gris-OHPP SD. The results were vertically displayed by arbitrary amounts.

To study the intermolecular interaction between Gris and OHPP, FT-IR scan was performed on pure Gris, OHPP and Gris-OHPP SD, and the results were presented in Figure 3.1. The results suggested that the hydrogen bonding was the major interaction between Gris molecules and OHPP. Firstly, for OHPP and pure Gris, their respective spectral scan results (the bottom 2 black curves in Figure 3.1) demonstrated that all the typical spectral peaks were observed (Jambhrunkar et al., 2014; Al-Obaidi et al., 2013; Xie & Yao, 2018). The spectral scan was further conducted with Gris-OHPP SD as shown by the top red curve in Figure 3.1. One can observe that the C-H stretching bands at  $2974\text{-}2880\text{ cm}^{-1}$  were broadened in Gris-OHPP SD spectrum, suggesting the involvement of C-H in H-bonding. The weakening of C=O stretching peak (at  $1660$

$\text{cm}^{-1}$ ) in Gris-OHPP SD spectra indicated the formation of hydrogen bonds, where C=O acted as hydrogen accepting group. Furthermore, the slight shift of –OH stretching at around  $3480\text{ cm}^{-1}$  in Gris-OHPP SD implied the possible H-bond formation

### 3.4.2 *In-vitro* efficacies of Gris in Gris-OHPP SD (separate the test)

The *in-vitro* efficacies of Gris-OHPP SD was investigated by examining the following parameters: the solubility, release rate, Caco-2 permeation and anti-fungal efficiency of Gris. The solubility test evaluated Gris soluble amount in its solid dispersion and the result was shown in Figure 3.2. Our finding indicated that OHPP substantially enhanced the soluble amount of Gris in water. The soluble amount of Gris of Gris-OHPP SD was  $854.62\text{ }\mu\text{g/mL}$ , which was 22 times higher than that of pure Gris ( $37.70\text{ }\mu\text{g/mL}$ ).

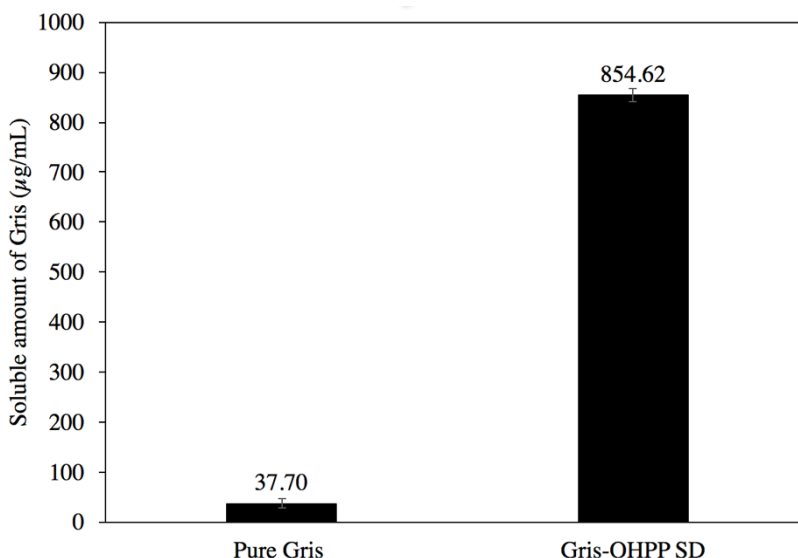


Figure 3.2 Gris solubility after equilibrating at  $25\text{ }^{\circ}\text{C}$  for 24 h. Values were represented as the amount of Gris remained soluble after 24 h. Data are expressed as mean  $\pm$  SD ( $n = 3$ ).

OHPP showed superior performance in solubilizing Gris ( $>800\text{ }\mu\text{g/mL}$ ) with a high drug loading capacity of 20%. While previous research suggested that mesoporous silica nanoparticles, micronization and HPMCAS were only able to enhance Gris soluble amount to  $62.3\text{ }\mu\text{g/mL}$ ,  $30.56\text{ }\mu\text{g/mL}$  and  $200\text{ }\mu\text{g/mL}$ , respectively (Jambhrunkar et al., 2014; Zili et al., 2005; Chiang et al., 2013).

The proposed mechanisms for OHPP to solubilize Gris molecules were: (a) the hydroxypropyl (HP) and octenyl succinate (OS) groups interacted with Gris through hydrogen-bonding and hydrophobic interactions; and (b) the highly-branched dendritic structure of PG promoted the adsorption of Gris by physically ‘trapping’ the drug molecule within the glucan chains network. In addition, the physical processing achieved efficient particle size reduction, which subsequently generated large surface area and encouraged the incorporation of Gris and OHPP.

The Caco-2 cell monolayer permeation test was performed on Gris-OHPP SD to predict the *in-vivo* absorption of Gris upon OHPP incorporation. The cumulative amount of Gris across the Caco-2 monolayer was shown in Figure 3.3. The result showed that both pure Gris and Gris-OHPP SD showed a loading dose-dependent increase in Gris permeation amount, while Gris-OHPP SD exhibited more enhanced effect.

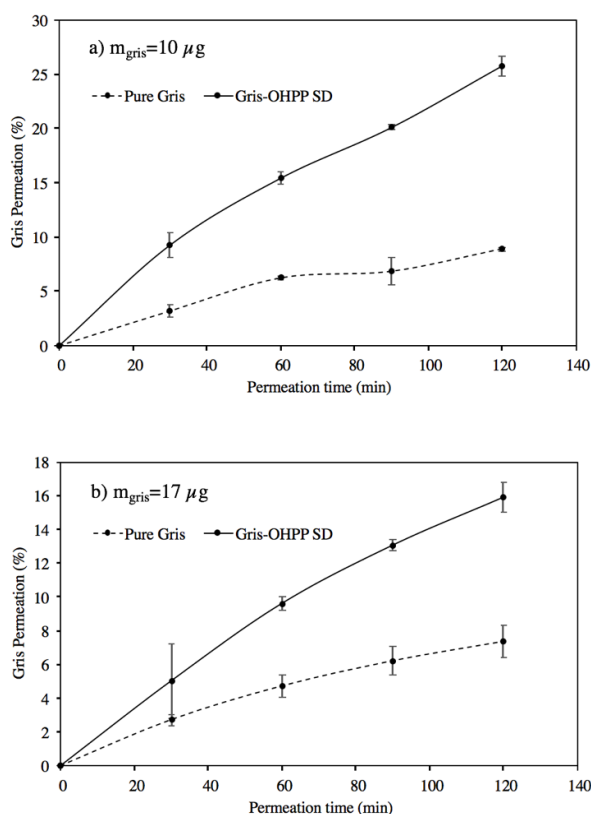


Figure 3.3 Cumulative Gris permeations across the Caco-2 monolayers, with apical loading of Gris total amount of: A)  $m_{gris} = 10 \mu g$  and B)  $m_{gris} = 17 \mu g$ . The ‘Gris Permeation (%)’ was calculated by dividing the amount of Gris in basolateral compartment by the initial amount of Gris in the donor compartment. Data expressed as mean  $\pm$  SD ( $n = 3$ ), significant differences between Gris and Gris-OHPP SD were denoted by different letters ( $p < 0.05$ ).

Figure 3.3a showed that, at the 20 µg/mL (10 µg/well) loading amount, the percentage of permeated Gris for pure Gris and Gris-OHPP SD were 8.9% (0.89 µg/well) and 25.8 % (2.58 µg/well), respectively. According to Figure 3.3b, at the loading of 34 µg/mL (17 µg/well), the percentage of permeated Gris for pure Gris and Gris-OHPP SD were 7.4% (1.26 µg/well) and 15.9% (2.70 µg/well), respectively. The results indicated that Gris-OHPP SD achieved 2.2 ~ 2.8 folds of Gris permeation amount than that of pure Gris, implying the substantial higher amount of Gris being solubilized.

Table 3.1 The MIC range of Gris against *Trichophyton rubrum*

	MIC <sub>90</sub> (µg/mL)	MIC <sub>50</sub> (µg/mL)
Pure Gris	>8.0	>8.0
Gris-OHPP SD	1.0	0.25

Finally, the antifungal efficacy of Gris-OHPP SD and pure Gris were tested against *Trichophyton rubrum* to examine Gris bioactive, and the MIC<sub>90</sub> and MIC<sub>50</sub> of pure Gris and Gris-OHPP SD. The MIC range of Gris were summarized in Table 3.1. It was found that no antifungal activity was observed for pure Gris within the tested concentration range. However, for Gris-OHPP SD, the MIC<sub>90</sub> and MIC<sub>50</sub> against *T. rubrum* were 1 µg/mL and 0.25 µg/mL, respectively, which were consistent with the previous report (da Silva Barros et al., 2007). Overall, the finding indicated that Gris of Gris-OHPP was bioactive and available to exert its bio-function without assistant of organic solvents (*e.g.* DMSO, ethanol, methanol, etc.).

### 3.5 Conclusion

In this study, OHPP showed promising properties in improving soluble amount of Gris. FTIR analysis revealed the hydrogen bonds formed between Gris and OHPP. The soluble amount of Gris of Gris-OHPP was 22 times higher than that of pure Gris. Depending on the loading amount of Gris in apical compartment, the percentage of permeated Gris of Gris-OHPP SD was 2.2~2.8 times higher than that of pure Gris. The *in-vitro* antifungal susceptibility tests demonstrated that the MIC<sub>90</sub> and MIC<sub>50</sub> values of Gris-OHPP SD were consistent with previous reports, indicating

the bio-function of Gris was not compromised upon OHPP incorporation. In summary, the results revealed that OHPP is capable in solubilizing poor soluble Gris and enable its *in-vitro* bio-efficacy.

### 3.6 Reference

- Al-Obaidi, H., & Buckton, G. (2009). Evaluation of griseofulvin binary and ternary solid dispersions with HPMCAS. *AAPS PharmSciTech*, 10(4), 1172.
- Al-Obaidi, H., Lawrence, M. J., Al-Saden, N., & Ke, P. (2013). Investigation of griseofulvin and hydroxypropylmethyl cellulose acetate succinate miscibility in ball milled solid dispersions. *International journal of pharmaceutics*, 443(1-2), 95-102.
- Chen, H., & Yao, Y. (2017). Phytoglycogen improves the water solubility and Caco-2 monolayer permeation of quercetin. *Food chemistry*, 221, 248-257.
- Chiang, P. C., Cui, Y., Ran, Y., Lubach, J., Chou, K. J., Bao, L., ... & Qin, A. (2013). In vitro and in vivo evaluation of amorphous solid dispersions generated by different bench-scale processes, using griseofulvin as a model compound. *The AAPS journal*, 15(2), 608-617.
- da Silva Barros, M. E., de Assis Santos, D., & Hamdan, J. S. (2007). Evaluation of susceptibility of Trichophyton mentagrophytes and Trichophyton rubrum clinical isolates to antifungal drugs using a modified CLSI microdilution method (M38-A). *Journal of medical microbiology*, 56(4), 514-518.
- Hbaieb, S., Kalfat, R., & Chevalier, Y. (2012). Loading antifungal drugs onto silica particles grafted with cyclodextrins by means of inclusion complex formation at the solid surface. *International journal of pharmaceutics*, 439(1-2), 234-245.
- Iradhati, A. H., & Jufri, M. (2017). Formulation and physical stability test of griseofulvin microemulsion gel. *International Journal of Applied Pharmaceutics*, 9, 23-26.
- Jambhrunkar, S., Qu, Z., Popat, A., Karmakar, S., Xu, C., & Yu, C. (2014). Modulating in vitro release and solubility of griseofulvin using functionalized mesoporous silica nanoparticles. *Journal of colloid and interface science*, 434, 218-225.
- Ong, S. G. M., Ming, L. C., Lee, K. S., & Yuen, K. H. (2016). Influence of the encapsulation efficiency and size of liposome on the oral bioavailability of griseofulvin-loaded liposomes. *Pharmaceutics*, 8(3), 25.
- Petersen, A. B., Rønneest, M. H., Larsen, T. O., & Clausen, M. H. (2014). The chemistry of griseofulvin. *Chemical reviews*, 114(24), 12088-12107.

- Rodriguez-Rosales, R. J., & Yao, Y. (2019). Phytoglycogen, a natural dendrimer-like glucan, improves the soluble amount and Caco-2 monolayer permeation of curcumin and enhances its efficacy to reduce HeLa cell viability. *Food Hydrocolloids*, 105442.
- Santos, D. A., & Hamdan, J. S. (2005). Evaluation of broth microdilution antifungal susceptibility testing conditions for *Trichophyton rubrum*. *Journal of Clinical microbiology*, 43(4), 1917-1920.
- Wani, R. J., Sharma, P., Zhong, H. A., & Chauhan, H. (2020). Preparation and Characterization of Griseofulvin Solid Dispersions. *ASSAY and Drug Development Technologies*, 18(3), 109-118.
- Xie, Y., & Yao, Y. (2018). Octenylsuccinate hydroxypropyl phytoglycogen, a dendrimer-like biopolymer, solubilizes poorly water-soluble active pharmaceutical ingredients. *Carbohydrate polymers*, 180, 29-37.
- Zadeha, B. S. M., Salimi, A., & Aminib, R. (2017). Novel Super Saturated Self-Emulsifying System for Oral Delivery of Griseofulvin: Design, Preparation and ex-vivo Intestinal Permeability. *Journal of Reports in Pharmaceutical Sciences*, 6(2), 180-190.
- Zili, Z., Sfar, S., & Fessi, H. (2005). Preparation and characterization of poly- $\epsilon$ -caprolactone nanoparticles containing griseofulvin. *International journal of pharmaceutics*, 294(1-2), 261-267.

## CHAPTER 4. OCTENYLSUCCINATE HYDROXYPROPYL PHYTOGLYCOGEN (OHPP) TO ENHANCE THE SOLUBILITY AND *IN-VITRO* EFFICACIES OF RESVERATROL

### 4.1 Abstract

This study evaluated the capability of phytoglycogen (PG) derivatives hydroxypropyl phytoglycogen (HPP) and octenylsuccinate hydroxypropyl phytoglycogen (OHPP) to improve the aqueous soluble amount and Caco-2 monolayer permeation of resveratrol (RES). The OHPP-RES and HPP-RES solid dispersions (SDs) were prepared using spray-drying at OHPP/RES and HPP/RES ratios of 4/1. The obtained solid dispersions were characterized for RES soluble amount, crystallinity, intramolecular interaction, dissolution profile and *in-vitro* permeation. X-ray diffraction patterns showed the reduced crystallinity of RES in its solid dispersions. FTIR spectra indicated the formation of hydrogen bond between RES and HPP/OHPP. The soluble amount of RES in OHPP-RES SD and HPP-RES SD were 638 µg/mL and 176.7 µg/mL, respectively, which were over 17 and 5 times than that of RES alone (35.2 µg/mL), respectively. For dissolution test, OHPP-RES SD and HPP-RES SD released 98.5% and 94.97% of RES, respectively. In contrast, the dissolution rate of RES alone was only around 33.8%. The trans-epithelial permeation results showed that RES molecule was successfully released from HPP and OHPP to exert its biofunction.

### 4.2 Introduction

Resveratrol (RES) is a polyphenol, naturally present in more than 70 plant species, especially abundant in grape skin, peanuts berries, red wines and various human foods. Many pharmacological effects have been reported for RES, including, anti-oxidant, anti-fungal, anti-cancer, anti-carcinogenic, and cardio-protective properties (Singh et al., 2019). Moreover, RES has been shown to treat obesity-related disease either by reducing adipose tissue mass through stimulating lipolysis of existing adipocytes (Baile et al., 2011), and serving as calorie restriction mimetic (Timmers et al., 2011).

RES has many health and therapeutic benefits in humans, yet its low water solubility became the major limiting factor for clinical and pharmaceutical applications. Poor aqueous solubility leads to reduced dissolution rate and bioavailability. According to previous research, the

plasma RES concentration cannot be related to the dosage administered (Timmers et al., 2011, Almeida et al., 2009). It was noted that by increasing oral dosage of RES by 20 times, its plasma level only achieved a 6-fold enhancement due to low solubility (Boocock et al., 2007). Meanwhile, it's been reported that the total RES release might take hours to days, which was too long for skin, gut and nasal mucosa applications (Isely et al., 2019). In addition, percentage of RES release during dissolution was saturated only around 50% over 24 hours (Pujara et al., 2017).

Consequently, numerous novel delivery systems of RES have been designed for the enhanced bioavailability through improving RES solubility and dissolution rate. The amorphous solid dispersion (ASD) is of great interest as it can achieve orders of magnitude increases in dissolution rate and apparent solubility. Polymers, especially the synthetic ones, are among the most commonly-used additives in ASD. Many polymers such as PVP, HPMC, HPMCAS, PAA and CM CAB have been applied to formulate RES in ASD form (Wegiel et al., 2013).

Over the past 20 years there has been an increasing interest in dendrimer particle for the delivery of hydrophobic active ingredients. Dendrimer's highly branched structure provides both surface reaction site and interior cavity for the encapsulation of guest molecules. Among various dendrimer-like particles, phytoglycogen (PG), a natural, highly branched, glucan extracted from the kernel of maize mutant sugary-1(su 1) through formation of covalent bond to the terminal groups. PG has shown outstanding capacity in the delivery of many polyphenols, such as, curcumin, quercetin and lutein (Chen and Yao 2017, Chen and Yao 2017a, Chen, Narsimhan and Yao 2015).

Numerous reactive surface ending groups allowed PG to be functionalized through chemical modifications. Previous research reported that the hydroxyl group on PG surface was esterified with octenylsuccinate groups to form phytoglycogen octenylsuccinate (PG-OS). PG-OS facilitated emulsion formation to prevent lipid oxidation and prolong efficacy of bacteriocin (Bi et al., 2011; Scheffler et al., 2010). To further extend the functionality of PG nanoparticle, dual modifications were carried out to provide PG with more desirable properties (Ariyantoro et al., 2018). For example, Nano-11, an octenylsuccinate and (3-Chloro-2-hydroxypropyl) trimethylammonium chloride (CHTAC) modified PG nanoparticle, has been successfully utilized as vaccine adjuvant (Lu et al., 2015); OHPP, an amphiphilic biopolymer that is prepared by grafting PG particle with octenylsuccinate and hydroxypropyl groups, realized the delivery of many water insoluble active ingredients, e.g. celecoxib, docetaxel, paclitaxel, fenofibrate, curcumin and griseofulvin (Xie & Yao, 2019; Xie & Yao, 2018a; Xie & Yao, 2018b).

The objective of this study was to evaluate and compare two of the PG derivatives hydroxypropyl phytoglycogen (HPP) and octenylsuccinate hydroxypropyl phytoglycogen (OHPP) that represent single and dual modification of PG particles, respectively, to improve the water solubility, dissolution rate and Caco-2 monolayer permeation of RES without the assist of organic solvent.

### **4.3 Materials and Methods**

#### **4.3.1 Chemicals**

Resveratrol ( $C_{14}H_{12}O_3$ , > 99% purity) was obtained from TCI Chemicals (Pvt. Ltd., Chennai, India). The Caco-2 BBE cell was purchased from ATCC (Rockville, MD). Lactate dehydrogenase (LDH) cytotoxicity assay kit was purchased from Thermo Fisher Scientific (Pittsburgh, PA). Propylene oxide and octenylsuccinate anhydride were obtained from Sigma-Aldrich. All chemicals used were of analytical grade.

#### **4.3.2 Preparation of hydroxypropyl phytoglycogen (HPP) and octenylsuccinate hydroxypropyl phytoglycogen (OHPP)**

The preparation of OHPP and HPP were according to Xie & Yao (2017) with modifications. Firstly, 70 g of phytoglycogen (PG) was dissolved in water to form 18% (w/w) dispersion. PG was extracted according to Chen & Yao (2017). Thereafter, sodium hydroxide was added to PG dispersion at a concentration of 5.9% (w/w), followed by heating for an hour at boiling temperature. The resulting mixture was transferred to the high-pressure reactor, and 350 mL and 700 mL propylene oxide (PO) was continuously pumped into the reactor for 10 hours at the speed of 0.59 mL/min and 1.16 mL/min to obtain HPP500 (the intermediate product of OHPP) and HPP, respectively. The reaction was proceeded for another 15 h before neutralization. The reaction temperature was maintained at 40 °C. Afterwards, the ultrafiltration (300kD MWCO, centramate™, Pall Life Science, NY) was conducted to purify HPP500 and HPP dispersions. The HPP dispersion was subsequently spray-dried to obtain the dried particles.

To prepare OHPP, and octenyl succinic anhydride (OSA) was gradually added to the purified HPP500 dispersion in an OSA: PG glucosyl unit ratio of 1:1 within 5 h. The pH was maintained between 8.5 and 9.0 using NaOH. The reaction was carried out at 40 °C and terminated

after 24 h by reducing the pH to 6.5 using HCl. Afterwards, the mixture was subjected to ultrafiltration system (300kD MWCO, centramate™, Pall Life Science, NY) to obtain the purified OHPP.

Furthermore, the purified OHPP and HPP dispersions were spray dried using a lab scale spray-dryer (mini B-290, BÜCHI, Switzerland) at inlet/outlet temperature 130 °C/90 °C, feeding rate of 5 mL/min, with a nitrogen flow of 350 L/min. The dried materials collected were OHPP and HPP.

### **4.3.3 Characterization of PG, HPP and OHPP particulates**

The weight average molecular weight ( $M_w$ ), z-average root-mean-square radius ( $R_z$ ), molecular density ( $\rho$ ) of PG, OHPP and HPP were determined in advance according to the method described by Scheffler et al. (2010). The  $\zeta$ -potential measurements were conducted by A Zetasizer Nano (ZS90, Malvern Instruments Ltd., UK) at room temperature, using 0.01% (w/v) PG, OHPP and HPP solutions prepared in 20 mM NaAc buffer (pH 5.5). In addition, the molar substitution (MS) of octenylsuccinate (OS) and hydroxypropyl (HP) groups with OHPP and HPP were determined using  $^1\text{H}$  NMR according to the method described by Xie & Yao (2018). All measurements were performed in triplicates and the results were presented as mean  $\pm$  standard deviation (SD).

Furthermore, the morphology of PG, OHPP and HPP particulates were studied by TEM. Firstly, OHPP was dissolved in pure ethanol (0.01% w/v); HPP and PG were dissolved in 0.02M NaAc buffer (pH 5.5, 0.01% w/v). To prepare the specimen, the support grid (400-mesh carbon-coated, FCF 400-Cu, EMS, PA) was glow discharged before loading the polymer fluid onto it. Thereafter, the grids were dried at room temperature, followed by a negative staining using 2% aqueous uranyl acetate. The specimens were observed using Tecnai G2 20 TEM (FEI company, Hillsboro OR) operated at 200 kV.

### **4.3.4 Preparation of RES Physical Mixture (PM) and Solid Dispersions (SD)**

The RES was incorporated with OHPP and HPP at a weight ratio RES: OHPP and RES: HPP of 1:4 in ethanol, then followed by spray drying to form OHPP-RES and HPP100-RES solid

dispersions (SDs). To achieve this, RES was fully dissolved in ethanol at 3.0 mg/mL, and OHPP/HPP was added to RES ethanol solution at a concentration of 12.0 mg/mL. The ethanol solutions were spray-dried to produce the dry powder of OHPP-RES and HPP100-RES SDs using Büchi Mini-spray dryer B-290 (Büchi Labortechnik AG, Switzerland) equipped with nitrogen purge for the use of organic solvents. The system was operated at an inlet and outlet temperature of 90 °C and 57–60 °C, respectively, with a feeding rate at 6 mL/min, and nitrogen flow at 350 L/h. The organic solvent in the nitrogen gas collected from the outlet was condensed in Büchi Inert Loop B-295.

OHPP/RES and HPP/RES physical mixtures (PMs) were prepared by blending RES and OHPP/HPP using mortar and pestle at the weight ratio of 1:4. All solid dispersions and physical mixtures were stored at -20°C.

#### **4.3.5 Phase solubility of RES in each of HPP and OHPP**

The solubilizing capacity of OHPP and HPP was quantitatively evaluated by the phase solubility method developed by Higuchi and Connors (1965). An excessive amount of RES was added to DI water that contained increasing concentrations (0, 12.5, 25, 50, and 100 mg/mL) of OHPP/HPP. The suspensions were shaken in water bath (SHEL LAB Models WS27, VWR International, PA) at 25 °C for 24 h and then centrifuged at 16,000 × g for 5 min. The supernatant was collected and re-constituted in ethanol for RES quantification using HPLC. Experiments were performed in triplicate.

#### **4.3.6 X-ray powder diffraction**

To evaluate the crystallinity of HPP, OHPP and RES in RES-containing solids, X-ray powder diffraction crystallgrams were obtained by X-ray powder diffractometer (XRD-6000, Shimadzu, North America) with a Bragg-Brentano optical setup equipped a long fine focus x-ray tube. All samples were scanned over a range of 10°–35° with nickel filtered Cu K $\alpha$  radiation ( $\lambda = 1.5406 \text{ \AA}$ ) at 40 kV and 30 mA. The scanning speed was 8° (2 $\theta$ )/min.

#### **4.3.7 FT-IR**

To study the intermolecular interaction between RES molecule and OHPP/HPP, the infrared spectra of RES alone, OHPP, HPP, RES/OHPP PM, RES/HPP PM, RES-OHPP SD and HPP-RES SD were obtained with Thermo-Nicolet Nexus 470 FT-IR spectrometer (Nicolet, Thermo, USA) equipped with a Smart OMNI-sampler. A total of 40 accumulative scans were collected, with a resolution of  $4\text{ cm}^{-1}$ , within the frequency range of  $800 \sim 4500\text{ cm}^{-1}$ .

#### **4.3.8 Soluble RES amount determination**

In this study, soluble amount of RES in RES alone, OHPP-RES SD or HPP-RES SD was determined. Firstly, the RES-containing solids (contained 2.5 mg of RES) was fully dissolved in 1.0 mL DI water, followed by three minutes of vortexing. The suspensions were centrifuged ( $16,000 \times g$ , 5 min) to remove the insolubles. An aliquots of 0.2 mL supernatant was collected and transferred to 0.8 mL ethanol, and the soluble amount of RES was determined using HPLC. Experiments were performed in triplicate and the results were presented as mean  $\pm$  standard deviation (SD).

#### **4.3.9 Dissolution test**

The dissolution rate of RES in RES alone, OHPP-RES SD and HPP-RES SD were determined using dissolution paddle method using USP Apparatus II (paddle) (Varian VK7025, Varian Inc, Cary, CA). The experiments were conducted in 1000 mL vessel containing 500 mL phosphate buffer (USP SIF, pH 6.8, 58 mM) without pancreatin. Accurately weighed samples containing the equivalent of 50 mg RES were dispersed in 500 mL phosphate buffer (pH 6.8, 50 mM), and stirred with rotating paddles at 100 rpm ( $37\text{ }^{\circ}\text{C}$ ). At pre-determined time intervals (10, 20, 30, 60, 90, 120, 150 and 180 min), aliquots of 1 mL fluid were aspirated and centrifuged ( $16,000 \times g$ , 5 min). Thereafter, supernatant of 0.2 mL was withdrawn and re-constituted with 0.8 mL ethanol for RES quantification using HPLC. Experiments were carried out in triplicate.

#### **4.3.10 RES Caco-2 cell permeation analysis**

##### ***RES working dispersions preparation and stability tests***

Working dispersions of RES (0.5% DMSO), OHPP-RES SD, and HPP-RES SD were prepared for Caco-2 cell cytotoxicity and monolayer permeation tests. For RES (0.5% DMSO) working dispersions, a DMSO stock dispersion of was prepared by dissolving pure resveratrol in 1 mL DMSO (RES content 3000 µg/mL). Thereafter, the stock dispersion was serial diluted to working dispersions of RES concentration at 15 µg/mL, and 30 µg/mL in HBSS (pH 6.5). For OHPP-RES SD working dispersions, 15 mg OHPP-RES SD was dissolved in 1 mL buffer HBSS (pH 6.5), and further diluted to RES concentration of 15 and 30 µg/mL with HBSS (pH 6.5).

In Caco-2 cell permeation test, the Caco-2 cells were incubated with RES working dispersions for 2 hours. Thereby, the stability of RES (0.5% DMSO), OHPP-RES SD, and HPP-RES SD working dispersions were examined. The freshly prepared working dispersion was incubated in a 24-well plate (Corning, NY) under incubation conditions (37°C). At pre-determined time points 0 min, 60 min and 120 min, aliquots of 0.33 mL were withdrawn from each well and subjected to centrifugation (5,000×g for 3 min) to remove insolubles. The supernatant was collected RES soluble amount quantification using HPLC.

##### ***RES Caco-2 cell monolayer permeation test***

The human intestinal Caco-2 cell line was obtained from ATCC (Rockville, MD). To prepare the cell stock, Caco-2 cells were cultured in DMEM medium supplemented with 10% FBS, 1% L-glutamine, 100 units/mL penicillin, and 100 µg/mL of streptomycin (Sigma-Aldrich), and maintained at 37°C in 95% air/5% CO<sub>2</sub>. The passages of cells used were between 90 ~ 105. The monolayer was sub-cultured every 3 days at 80–90% confluence.

The impact of OHPP, HPP, RES (0.5% DMSO), HPP-RES SD, and OHPP-RES SD working dispersions on the cytotoxicity of Caco-2 monolayer cells was examined by LDH test. Firstly, Caco-2 cells were seeded at a density of  $6 \times 10^5$  cells/mL in 24-well plates (Corning, NY) containing 500 µL DMEM (10% FBS)/well. The cells attached to the bottom of the well and propagated as a monolayer after 21~23 days of incubation. The monolayers were incubated with RES-containing working dispersions for 2 hours. The monolayers incubated with 500 µL HBSS (pH 6.5), and 500 µL lysis buffer (10×) for 45 min served as negative and positive control,

respectively. After incubation, the plates were centrifuged (250×g, 3min), and the supernatant (50 µL) was collected and mixed with 50.0 µL of diluted LDH reaction mixture (Pierce LDH Cytotoxicity Assay Kit, Thermo Scientific). The mixtures were further incubated in dark for another 30 min before adding the stop solution (50.0 µL/well). The absorbance values were measured at 490 and 680 nm. The experiment was performed in triplicate.

For permeation tests, Caco-2 cells were seeded on 12-well polycarbonate trans-well membrane inserts (area: 1.12 cm<sup>2</sup>, 0.4 µm pore size, Corning Costar Corp. NY) at a cell density of 6.0 × 10<sup>5</sup> cells/cm<sup>2</sup>, and maintained for 21~23 days to develop monolayer. The apical chamber and basolateral chamber were filled with 0.5 mL and 1.5 mL medium (DMEM with 10% FBS), respectively. The medium was changed every other day. The integrity of the monolayer was monitored by measuring trans-epithelial electrical resistance (TEER) value using Millicell-ERS equipment (Millipore, USA) before and after the test. The wells that exceeded 250 Ω/cm<sup>2</sup> were selected for further permeation test.

The culture medium (DMEM with 10% FBS) was changed 12-24 h before the experiment. The monolayers were rinsed twice using HBSS buffer (pH 7.4, 37 °C) 30 minutes before test. RES (0.5% DMSO), HPP-RES SD, and OHPP-RES SD working dispersions (15 µg/mL and 30 µg/mL) were loaded into the apical compartment. Pure HBSS (pH 6.5, 37 °C) was taken as control. After 0 min, 30 min, 60 min, 90 min and 120 min of incubation, aliquots of 0.75 mL were taken from basolateral compartments and replaced with equal amount of HBSS medium. The collected fluid was dissolved in ethanol at volume ratio of 1:4 (HBSS: ethanol w/w), and the mixture was subjected for RES quantification. Each treatment was performed in triplicate.

#### **4.3.11 Statistical Analysis**

All experiments were performed in triplicate for each condition. Results were presented as mean ± standard deviation (SD). One-way ANOVA was performed for significant difference analysis. P-value ≤ 0.05 was used to identify significant differences between results using SPSS for Windows (version rel. 10.0.5, 1999, SPSS Inc., Chicago, IL, USA).

## 4.4 Results

### 4.4.1 HPP and OHPP characterization

Figure 4.1. showed the TEM image of phytyglycogen (PG), hydroxypropyl phytyglycogen (HPP) and octenylsuccinate hydroxypropyl phytyglycogen (OHPP) used in this study. The PG nanoparticle showed cauliflower-like shape with small portion of aggregates. The image of OHPP and HPP revealed that most nanoparticles were individually dispersed.

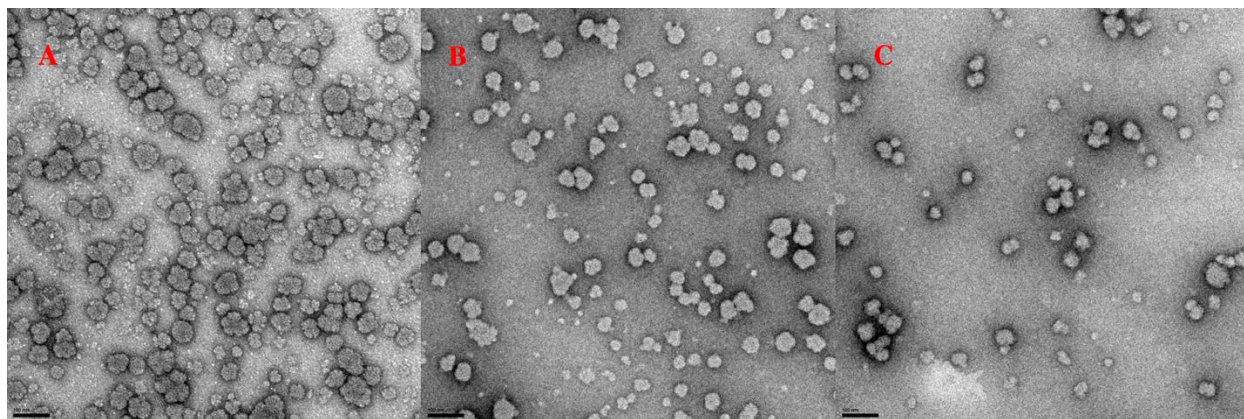


Figure 4.1 Transmission electron microscopy (TEM) images of native phytyglycogen (A), hydroxypropyl phytyglycogen (B) and octenylsuccinate hydroxypropyl phytyglycogen (C). The scale bar represented 100 nm.

The molecular weight ( $M_w$ ), particle size ( $R_z$ ), and  $\zeta$ -potential (mV) values of PG, HPP and OHPP were shown in Table 4.1. The  $M_w$  of PG, HPP, and OHPP were  $1.98 \times 10^7$ ,  $2.26 \times 10^7$ , and  $1.70 \times 10^7$  g/mol, respectively. For  $R_z$  values, PG (18.5 nm) particulate decreased to 15.9 nm for HPP, and 17.0 nm for OHPP. The  $R_z$  value for PG was generally large as HPSEC allowed the sizing of fragments, monomers and aggregates. For HPP and OHPP, the bulky hydroxypropyl group (HP) destruct the inter-molecular forces among aggregates (Masina et al., 2017), which led to the reduced apparent particle size. Noticeably, the  $\zeta$ -potential of OHPP ( $-24.4 \pm 4.5$  mV) was significantly lower than that of PG ( $-5.37 \pm 2.5$  mV) due to the introduction of carboxylate moieties of OS groups. The NMR results was used to calculate the molar substitution (MS) of functional groups for PG derivatives. For OHPP, the MS values of the OS and HP groups were  $0.29 \pm 0.01$  and  $2.43 \pm 0.03$ , respectively. For HPP, the MS value of the HP groups was  $3.14 \pm 0.07$ .

Table 4.1 Molecular weight ( $M_w$ , g/mol), particle size ( $R_z$ , nm),  $\zeta$ -potential (mV), molecular density ( $\rho$ , g/mol $\cdot$ nm<sup>3</sup>), and molar substitution (MS) of HP and OS groups of PG, HPP and OHPP<sup>a</sup>.

<b>PG and PG derivatives</b>	<b><math>M_w</math>(g/mol) <math>\times 10^6</math></b>	<b><math>R_z</math> (nm)</b>	<b><math>\zeta</math>-potential (mV)</b>	<b><math>\rho</math> (g/mol<math>\cdot</math>nm<sup>3</sup>)<sup>1</sup></b>	<b>OS*</b>	<b>HP*</b>
<b>PG</b>	19.8 $\pm$ 0.1	18.5 $\pm$ 2.2	-5.37 $\pm$ 2.5	3138.3		
<b>HPP</b>	22.6 $\pm$ 0.3	15.9 $\pm$ 0.3	-5.4 $\pm$ 1.2	5633.1		3.14 $\pm$ 0.07
<b>OHPP</b>	17.0 $\pm$ 0.2	17.0 $\pm$ 0.7	-24.4 $\pm$ 4.5	3498.5	0.29 $\pm$ 0.01	2.43 $\pm$ 0.03

<sup>a</sup> Data were expressed as mean  $\pm$  standard deviation (SD) (n = 3).

\*OS and HP represented the molar substitution (MS) of octenylsuccinate groups (OS) and hydroxypropyl groups (HP)

<sup>1</sup> molecular density ( $\rho$ ) was calculated as  $\rho = \frac{M_w}{R_z^3}$

#### 4.4.2 Phase solubility of RES in each of HPP and OHPP

The solubilizing capacity of HPP and OHPP to dissolve pure RES in water was quantitatively evaluated by the phase solubility method developed by Higuchi & Connors (1965), and the results were presented in Figure 4.2. Our findings revealed that OHPP and HPP significantly enhanced the saturated solubility of pure RES in aqueous.

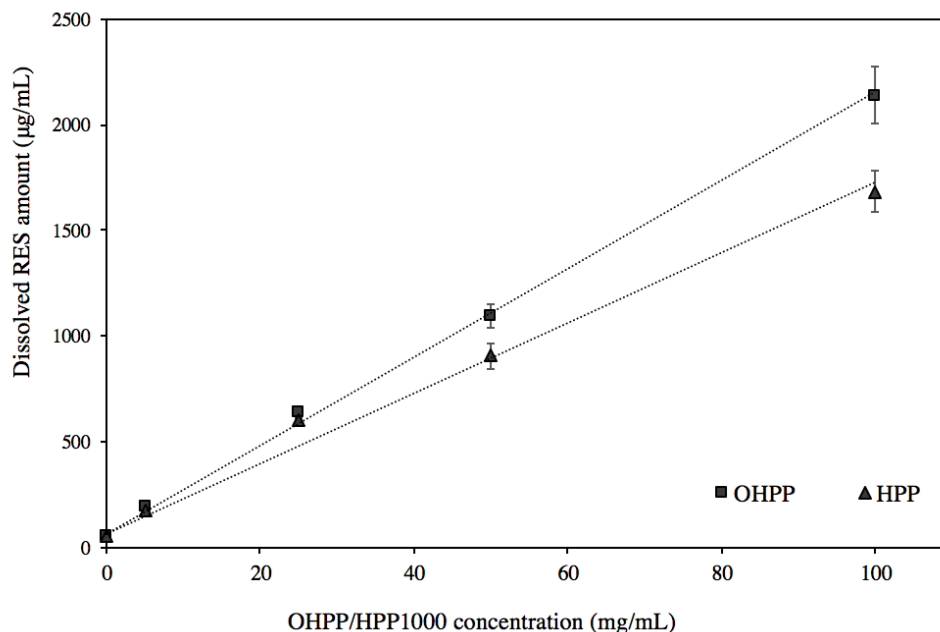


Figure 4.2 Phase solubility profiles of RES in the presence of OHPP/HPP in DI water at 25 °C for 24 hours. Data are expressed as mean  $\pm$  standard deviation (SD) (n = 3).

In Figure 4.2, the solubilized RES reached  $188.9 \pm 15.1$ ,  $642.1 \pm 5.7$ ,  $1094.1 \pm 58.4$ , and  $2139.0 \pm 135.6$   $\mu\text{g/mL}$  at OHPP concentration of 5, 25, 50 and 100 mg/mL, respectively. The amount of RES solubilized increased linearly ( $R^2=0.99$ ) with increasing OHPP concentrations, and the diagram can be classified as  $A_L$ -type phase-diagram (Higuchi & Connors, 1965). HPP showed similar trend, where the solubilized RES amount reached  $171.8 \pm 30.0$ ,  $602.6 \pm 10.2$ ,  $907.6 \pm 60.2$ , and  $1684.0 \pm 97.0$   $\mu\text{g/mL}$  at HPP concentration of 5, 25, 50 and 100 mg/mL, respectively.

OHPP and HPP concentration of 100 mg/mL, the soluble amount of RES reached 2139.5  $\mu\text{g/mL}$  and 1684.0  $\mu\text{g/mL}$ , respectively, which was 60.8 and 47.8 times that of pure RES (35.2  $\mu\text{g/mL}$ ). Both OHPP and HPP increased RES soluble amount significantly, whereas OHPP exhibited enhanced performance in solubilizing RES due to the extended hydrophobic surface brought by the octenylsuccinate groups.

#### 4.4.3 Intermolecular Interaction between RES molecule and each of HPP and OHPP particulates

FTIR was conducted to characterize intermolecular interaction between OHPP/HPP and RES, the results are presented in Figure 4.3. Firstly, spectral scan results of RES alone were displayed as top curve in both graph, where all characteristic peaks were observed. Characteristic bands corresponding to C–O stretching, phenolic C–O stretching and the trans olefinic band were seen at  $1380.8\text{ cm}^{-1}$ ,  $1145\text{ cm}^{-1}$ ,  $964.2\text{ cm}^{-1}$ , respectively (Bertacche et al., 2006). The small band due to C=C aromatic double-bond stretching were seen at  $1510.0$ ,  $1585.2\text{ cm}^{-1}$  and  $1604.5\text{ cm}^{-1}$ . Moreover, small bands at  $3018\text{ cm}^{-1}$  and  $1380.8\text{ cm}^{-1}$  were attributed to the –CH (phenyl ring) stretching and in-plane -OH (Pandita et al., 2014). At last, the broad peak due to the -OH stretching was at  $3201.3\text{ cm}^{-1}$ .

The bottom black curve in Figure 4.3A and B represented the spectra of HPP and OHPP, respectively. For both OHPP and HPP, the broad band at  $3400\text{ cm}^{-1}$  corresponded to –OH stretching (Eguchi et al., 2017). Absorption bands corresponding to –CH<sub>2</sub> and –CH stretching were seen at  $2964$  and  $2904\text{ cm}^{-1}$  in HPP,  $2929\text{ cm}^{-1}$  in OHPP, indicating the presence of hydroxypropyl groups (Eguchi et al., 2017; Mahdavinia et al., 2015). In addition, OHPP spectrum showed distinct peaks at  $1731\text{ cm}^{-1}$  and  $1571\text{ cm}^{-1}$ , which corresponded to C=O stretching of the ester group and asymmetric stretching vibration of carboxylate RCOO<sup>-</sup>, respectively (Fonseca-Florido et al., 2018; Wang et al., 2013), indicating the presence of OS groups. At last, peaks of –CH scissoring vibration and O–C–H, C–C–H and C–O–H bending vibrations were at  $1190\text{-}1500\text{ cm}^{-1}$  (Anjos et al., 2015; Hineno, 1977).

Moreover, the spectral scan was further conducted with physical mixtures and solid dispersions of RES-HPP and RES-OHPP. In Figure 4.3A and B, the two curves in the middle of both graphs represented the RES-HPP and RES-OHPP mixture processed by spray-drying and physical mixing at HPP:RES and OHPP:RES ratio of 4:1.

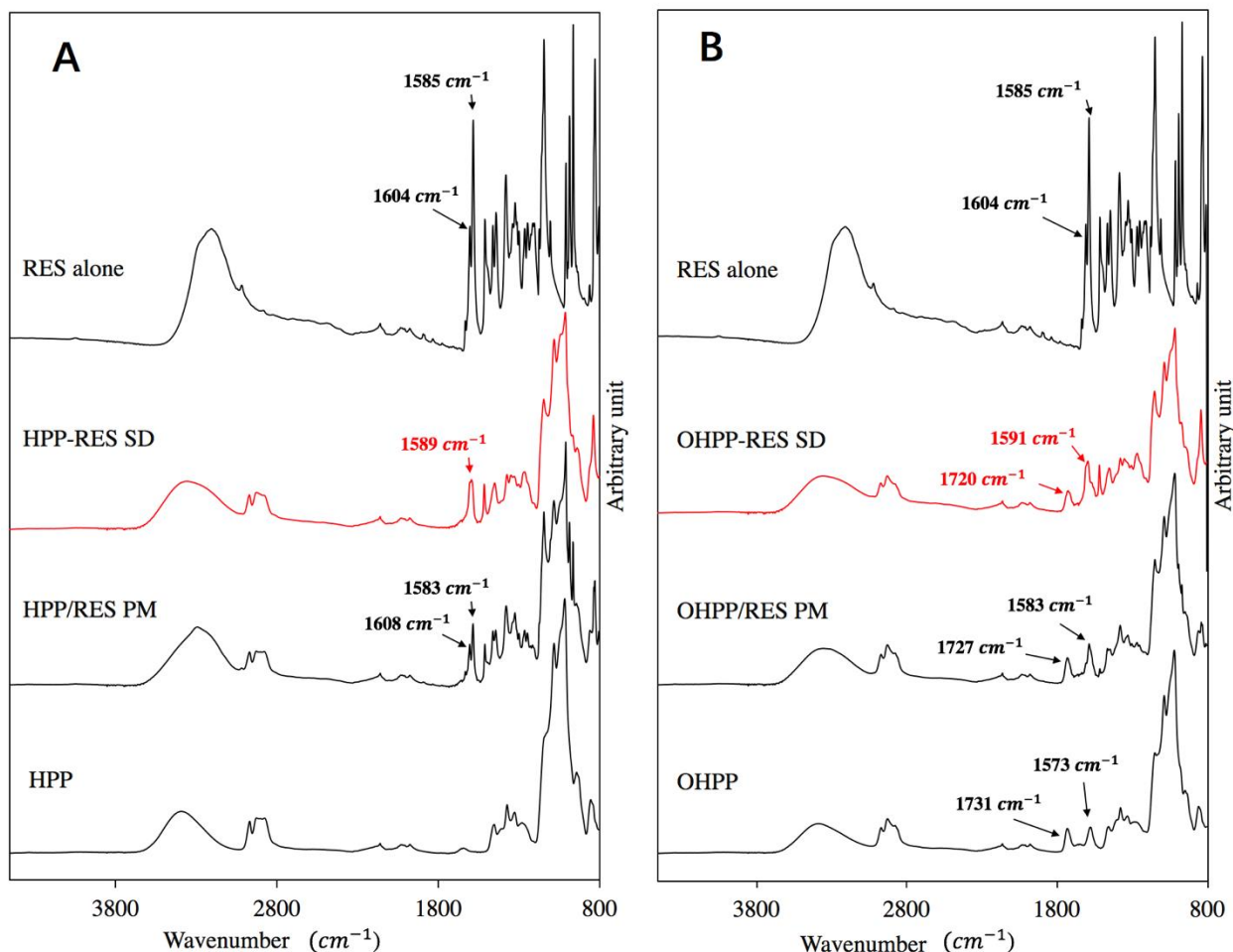


Figure 4.3 FTIR spectra of RES alone, HPP, OHPP and RES-containing formulations. OHPP, solid dispersions of RES with OHPP (OHPP-RES SD), and physical mixtures of RES with OHPP (OHPP/RES PM) were displayed in graph A; HPP, solid dispersion of RES with HPP (HPP-RES SD), and physical mixtures of RES with HPP (HPP/RES PM) were displayed in graph B. RES alone (RES alone) was included in both graphs, denoted as black curve on top.

As shown in Figure 4.3A and B, common features were observed in both RES-OHPP and RES-HPP formulations. The stretching peak of  $\text{-OH}$  in RES at  $3201.3 \text{ cm}^{-1}$  was significantly broadened and shifted to  $3291 \text{ cm}^{-1}$  and  $3380 \text{ cm}^{-1}$  in the spectrum of HPP-RES PM and HPP-RES SD, respectively. These stretching peaks were further broadened and shifted to  $3347 \text{ cm}^{-1}$  and  $3378 \text{ cm}^{-1}$  in OHPP-RES PM and OHPP-RES SD spectrum, respectively. The shift in the absorption bands indicated the hydroxyl groups in resveratrol participated in hydrogen bond formation. In addition, peaks at  $1585.2 \text{ cm}^{-1}$  and  $1604.5 \text{ cm}^{-1}$  ( $\text{C}=\text{C}$  stretching in aromatic rings in RES) were absent as they merged into a single broad asymmetric band at around  $1600.6 \text{ cm}^{-1}$  (OHPP-RES SD) and  $1589.0 \text{ cm}^{-1}$  (HPP-RES SD), suggesting that RES was physically embedded within OHPP

and HPP particulates. Furthermore, the peaks at  $1571\text{ cm}^{-1}$  and  $1731\text{ cm}^{-1}$  in OHPP shifted to  $1591\text{ cm}^{-1}$  and  $1720\text{ cm}^{-1}$  in OHPP-RES SD, respectively. These shifts indicated that the C=O ester and carboxylate group were involved in hydrogen-bonding.

#### 4.4.4 Crystallinity of RES in RES containing solid dispersions and physical mixtures

XRD analysis was performed to investigate the crystallinity of RES in its solid dispersions and physical mixtures with HPP and OHPP, and their X-ray diffraction patterns were shown in Figure 4.4. The X-ray diffraction patterns of RES-HPP formulations, RES alone, HPP, RES-HPP SD and RES-HPP PM, were presented in Figure 4.4A, and the crystallogram of RES alone, OHPP, RES-OHPP SD and RES-OHPP PM were shown in Figure 4.4B.

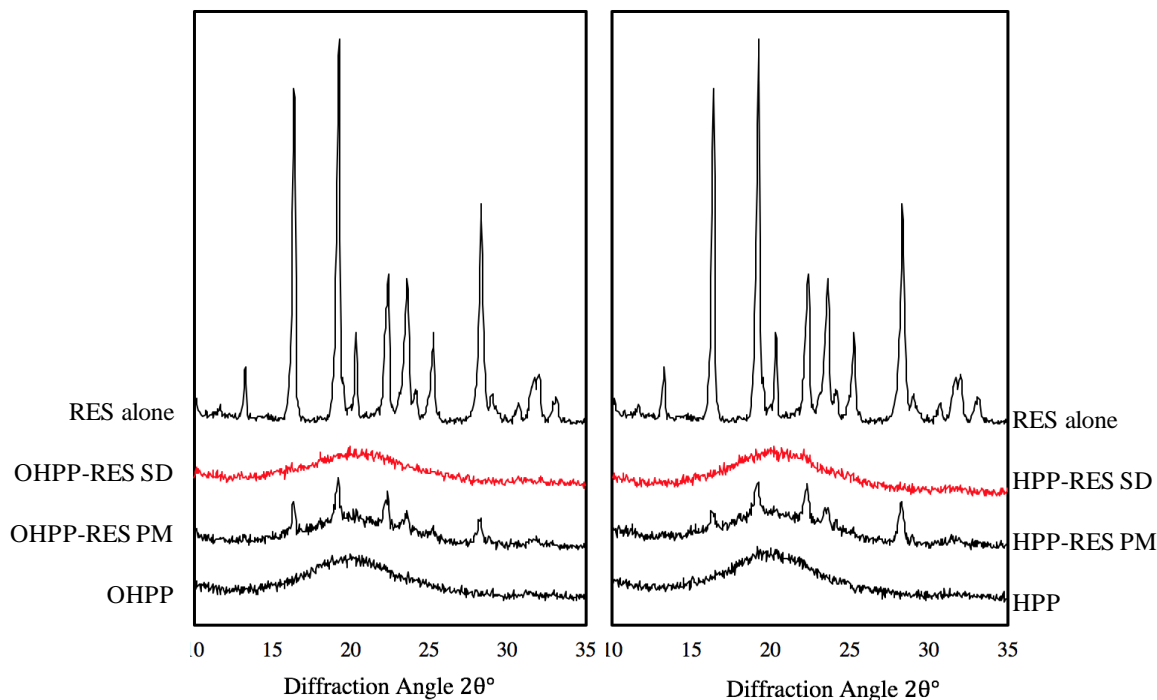


Figure 4.4 XRD crystallgrams of RES alone, OHPP, HPP, solid dispersions of RES with OHPP (OHPP-RES SD), HPP (HPP-RES SD), and physical mixtures of RES with OHPP (OHPP-RES PM), HPP (HPP-RES PM).

For RES alone, presented as top black curves in Figure 4.4A and B, the XRD crystallgram showed characteristic sharp peaks at  $2\theta^\circ$  values of  $13.20^\circ$ ,  $16.24^\circ$ ,  $19.24^\circ$ ,  $20.30^\circ$ ,  $22.44^\circ$ ,  $23.62^\circ$ ,  $25.30^\circ$ , and  $28.34^\circ$  over the range of  $10\text{-}35^\circ$ , indicating its crystalline nature (Dal Magro et al.,

2017; Popova et al., 2014; Liu et al., 2017). In addition, the amorphous nature of OHPP and HPP were evident in their spectra as no sharp diffraction peaks were observed (the bottom black curves in Figure 4.4A and B).

The XRD analysis was further performed with HPP-RES and OHPP-RES PM and SD (denoted by red curves in the spectra). Specifically, in both HPP-RES PM and OHPP-RES PM spectra, the characteristic peaks of RES at 16.32°, 19.16°, 22.32°, 23.56°, and 28.32° were still evident with reduced intensity. In addition, both OHPP-RES SD and HPP-RES SD spectra showed smooth curves without any diffraction peaks, suggesting the crystalline structure of RES was significantly reduced upon spray-drying processing.

The reduction of RES crystalline structure was due to the incorporation of OHPP and HPP, and spray-drying. For physical mixture, the reduced peaks intensities suggested that RES crystallites were either embedded among the outer glucan branches or remained unloaded. For solid dispersions, the solvent ethanol dissolved and broke down the crystalline structure of RES. The surface octenylsuccinic anhydride (OSA), hydroxypropyl (HP) groups, and branches of HPP and OHPP allowed the adsorption of RES molecules onto the surface of OHPP and HPP particulates through hydrogen-bonding and hydrophobic interactions. The surface adsorbed RES molecules were either embedded on the outer surface of the polymer or migrated to the inner region of the HPP/OHPP particulate. The RES molecules inside the polymer were physically entrapped within the highly-branched glucan network of HPP and OHPP. These interactions enabled the retention of amorphous structure of RES (Chen et al., 2015). In addition, the steric hindrance caused by the branching pattern of polymer reduced the dissociation of RES molecules from HPP and OHPP, thereby, prevented RES re-crystallization. Finally, the atomization and rapid solvent removal processes of spray-drying further enhanced the formation and retention of RES amorphous structure.

#### **4.4.5 RES soluble amount**

The soluble amount of RES in its solid dispersions and physical mixtures were examined in this study, and the results were displayed in Figure 4.5. In general, both OHPP and HPP substantially increased the soluble amount of RES, where OHPP showed more enhanced effect. In addition, the influence of processing approach was evaluated. The results suggested that both

physical mixture and spray drying substantially enhanced the soluble amount of RES, while spray-drying showed prominent effect.

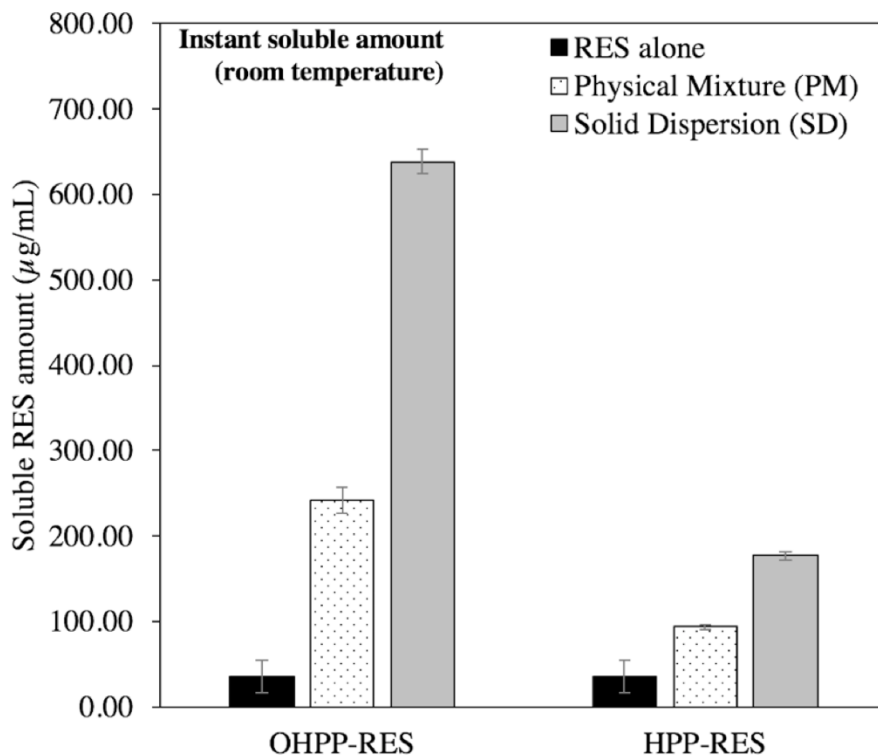


Figure 4.5 Soluble amount of RES in RES alone, OHPP-RES solid dispersion (SD) and physical mixture (PM) at OHPP:RES ratio of 4:1, HPP-RES SD solid dispersion (SD) and physical mixture (PM) at HPP:RES ratio of 4:1. The instant soluble RES amount (on the left) was determined by dispersing RES-containing samples in 1 mL DI water (RES content: 2500 µg/mL), the supernatant was collected after centrifugation (16,000 × g, 5 min). All experiments were carried out at room temperature and performed in triplicates. Data are expressed as mean ± SD (n = 3).

Firstly, the impact of carrier HPP and OHPP on RES soluble amount was evaluated (as shown in Figure 4.5). The inherent soluble amount of RES was 35.2 µg/mL. The results showed that both HPP and OHPP enhanced the aqueous soluble amount of RES substantially, where OHPP exhibited stronger solubilizing effect. For example, the instant soluble amount of RES in OHPP-RES PM reached 242.6 µg/mL, which was 2.6 times than that of HPP-RES PM (93.4 µg/mL). For solid dispersions, the instant soluble amount of RES in OHPP-RES SD was 638.1 µg/mL, which was 3.6 times than that of HPP-RES SD (176.7 µg/mL).

For each carrier, both solid dispersion (SD) and physical mixture (PM) enhanced the soluble amount of RES significantly, where the solid dispersion (SD) showed prominent results.

For example, the aqueous RES soluble amount was substantially improved by physical blending, reaching a soluble amount of RES at 242.6  $\mu\text{g/mL}$  and 93.4  $\mu\text{g/mL}$  for OHPP-RES PM and HPP-RES PM, respectively. The RES soluble amount was further enhanced by spray drying. According to Figure 4.5, OHPP-RES SD increased RES soluble amount by more than 2.6 times compared with OHPP-RES PM, reaching a value of 638.1  $\mu\text{g/mL}$ . HPP-RES SD elevated the soluble amount of RES by 0.9-fold (176.7  $\mu\text{g/mL}$ ) compared with that of physical mixture (93.4  $\mu\text{g/mL}$ ). Based on the test results, solid dispersions of OHPP-RES and HPP-RES with the highest soluble amount of RES were selected for dissolution and Caco-2 permeation test.

The highly-branched structure and surface functional groups of OHPP/HPP, and spray-drying processing significantly enhanced the total amount of RES suspending in the aqueous system, and effectively inhibited the recrystallization of RES. To incorporate RES with OHPP/HPP, both polymer and RES were fully dissolved in ethanol. During dissolution, the hydroxypropyl (HP) group on HPP was readily to interact with RES molecules and formed hydrogen bonds. For OHPP, the hydrophobic octenylsuccinate (OS) groups on the surface of OHPP provided additional sites to interact with RES molecules through either hydrogen bonding or hydrophobic interaction (Xie & Yao, 2018). These interactions increased the adsorption of RES onto the polymer surface. Furthermore, some of the surface adsorbed RES molecules migrated into the internal region of the polymer, and were physically entrapped inside the internal ‘cavity’ of the highly-branched architectures of OHPP and HPP. The physical entrapment increase the total soluble amount of RES in water. In addition, the spray-drying processing produced amorphous solid particles with improved wettability (Wang et al., 2015), which further improved the soluble amount of RES.

Two factors contributed to the retention of amorphous structure of RES. Firstly, the bulky and sterically crowded surface functional groups ‘capped’ the internal cavities. The entrapped RES molecules were not able to diffuse out of the polymer into the medium to recrystallize. Secondly, the dissolved polymer and RES will remain amorphous during spray-drying processing, as the atomization, rapid drying rate, and polymer kinetically inhibited RES crystallization.

In contrast, the mechanical stress of physical mixing was insufficient to reduce the particle size, therefore, RES remained in its crystalline state. The soluble amount of RES was governed by the phase solubility of OHPP and HPP.

#### 4.4.6 Dissolution test

RES is classified as Biopharmaceutics Classification System (BCS) Class II drug, possessing high permeability and low solubility, where its absorption rate and bioavailability is limited by *in-vitro* dissolution rate. Therefore, the enhancement of RES dissolution rate leads to the improved absorption and bioavailability of orally administered RES dosage. In this study, the *in-vitro* dissolution tests were conducted in 500 mL USP SIF (simulated intestinal fluid) pH 6.8 (50 mM) phosphate buffer without pancreatin to characterize the release rate of RES from its solid dosages. The measured dissolution rate of RES alone, OHPP-RES SD and HPP-RES SD within 180-minute dissolution period is shown in Figure 4.6.

In general, both HPP-RES SD and OHPP-RES SD enhanced the dissolution rate of RES in aqueous buffer, and OHPP outperformed HPP in releasing RES into the medium. For example, OHPP-RES SD and HPP-RES SD released 98.5% and 94.97% of RES, respectively. In contrast, the cumulative release of RES alone over 3 hours was only around 33.8%, which agreed with earlier reports (Pujara et al., 2017; Zhang et al., 2013; Hao et al., 2015).

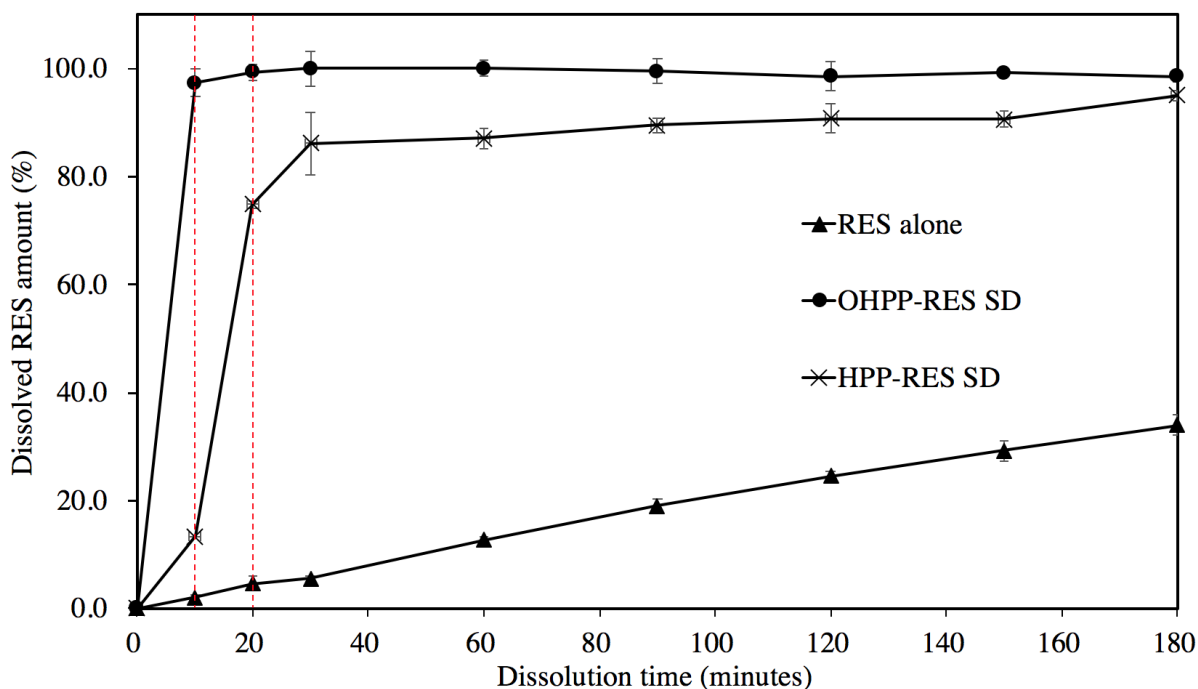


Figure 4.6 Dissolution profiles of RES alone, OHPP-RES SD and HPP-RES SD. Accurately weighed RES-containing solids (RES content of 50 mg) were dispersed into 500 mL phosphate buffer (pH 6.8, 58 mM), and stirred with rotating paddles at 100 rpm (37 °C). 1 mL aliquot was collected at pre-determined time points to determine the soluble amount of RES. Data are expressed as mean  $\pm$  SD (n = 3).

Examining with detail, a significant initial burst was observed in both OHPP-RES SD and HPP-RES SD formulations, and OHPP exhibited greater initial burst release. For example, a rapid increase of RES release rate was also seen in HPP-RES SD dissolution profile, where the cumulative dissolved RES amount reached 74.8% and 86.1% at the second (20-minute) and the third (30-minute) sampling points, respectively. OHPP-RES SD realized a faster dissolution of RES, where 97.3% of RES was into the medium by the first sampling time point (10-minute), which was 6.28 and 48.78 times higher than that of HPP-RES (13.4%) and RES alone (1.9%), respectively.

Furthermore, Figure 4.6. showed that both OHPP-RES SD and HPP-RES SD were able to maintain the supersaturated state of RES in aqueous system after the initial burst release. For example, after the first 10- minute, OHPP-RES SD maintained the soluble amount of RES over a period of 180-minute. HPP-RES SD showed similar trend, where no reduction of soluble amount of RES was observed. There was a gradual increase in HPP-RES SD dissolution from 74.8% at 10-minute to 94.9% at 180-minute.

XRD results indicated that the crystalline structure of RES was reduced upon the incorporation of OHPP and HPP through spray-drying (Liu et al., 2018). The amorphous solid dispersions of OHPP-RES and HPP-RES increased the total soluble amount of RES in the aqueous system (Pujara et al., 2017; Kanaujia et al., 2015; Merisko-Liversidge et al., 2003; Ubrich et al., 2004). The initial burst (rapid dissolution) can be attributed to the increased surface area and wettability due to spray-drying. The faster dissolution of OHPP-RES SD was due to the formation of higher energy phase resulted from interactions between OHPP and RES. In addition, the amorphized RES molecules were thermodynamically unstable which may lead to the recrystallization of RES. OHPP and HPP sustained the supersaturated state of RES through stabilizing the amorphous state. This was because the polymeric matrix effectively inhibited the recrystallization of the incorporated drugs (Nair et al., 2020).

#### **4.4.7 Caco-2 permeation of RES**

The Caco-2 cell monolayer permeation of RES upon OHPP and HPP incorporation was investigated. To ensure the integrity of the monolayer, the stability and cytotoxicity of the RES-containing working dispersions were examined. Firstly, the amount of RES in RES-containing

working dispersions remained soluble over 2-h incubation period was investigated. The amount of RES remained soluble at time 0, 1 and 2-h were displayed in Table 4.2, and the results showed that no significant decrease of soluble amount of RES was observed with any RES-containing working dispersions after 2-h incubation.

Table 4.2 The stability of RES-containing working dispersions in cell-free HBSS media after a 2-h incubation.\*

Incubation time	RES (0.5% DMSO) <sup>1</sup>		OHPP-RES SD <sup>1</sup>		HPP-RES SD <sup>1</sup>	
	15 µg/mL	30 µg/mL	15 µg/mL	30 µg/mL	15 µg/mL	30 µg/mL
<b>0-h</b>	13.00±0.72 a	25.31±2.71 a	10.35±0.41 a	19.12±0.44 a	10.05±0.30 a	15.32±1.09 a
<b>1-h</b>	11.00±1.85 a	25.00±1.51 a	11.63±0.79 a	23.54±0.21 b	10.15±1.52 a	24.44±0.43 b
<b>2-h</b>	12.10±0.13 a	24.89±0.42 a	12.06±0.46 a	25.06±0.78 b	10.58±0.35 a	25.33±1.26 b

\*The stability of RES-containing working dispersions were determined by the soluble amount of RES in the tested working dispersions in cell-free HBSS media (pH 6.5, 37°C, culture medium condition) at 0, 1 and 2-hour incubation time.

<sup>1</sup> Values are expressed as soluble amount of RES ± SD (n=3). Significant differences within RES (0.5% DMSO) group, OHPP-RES SD group, or HPP-RES SD group are denoted by different letters (p < 0.05).

The influence of OHPP and HPP on the viability of Caco-2 monolayers was displayed in Table 4.3. The result showed that the cell viability of OHPP and HPP were higher than 88.9%, and 84.4%, respectively. There was so significant cell viability reduction for all OHPP and HPP working dispersions, indicating that OHPP and HPP were generally non-toxic to Caco-2 cells.

Table 4.3 Cell viability results of OHPP and HPP with Caco-2 cells determined using the LDH assay.\*

OHPP/HPP Concentration (µg/mL)	Cell viability (%) <sup>*</sup>	
	OHPP <sup>1</sup>	HPP <sup>1</sup>
<b>10</b>	93.8±2.8 a	84.4±2.4 a
<b>100</b>	91.7±1.1 a	87.5±1.5 a
<b>200</b>	93.3±3.0 a	89.3±5.2 a
<b>500</b>	91.8±6.8 a	91.4±0.7 b
<b>1000</b>	88.9±5.1 a	90.0±1.3 ab
<b>2000</b>	92.8±4.4 a	86.2±3.1 a
<b>5000</b>	91.6±3.4 a	85.3±1.6 a

\*Percentage of survived cells was obtained after 2 h incubation with various OHPP and HPP working dispersions in HBSS at 37°C.

<sup>1</sup> Values are expressed as % cell viability ± SD (n=3). Significant differences within OHPP group or HPP group are denoted by different letters (p < 0.05). No significant difference of cell viability is found among OHPP treated Caco-2 cell monolayer.

Furthermore, the cytotoxicity of RES-containing working dispersions were evaluated using LDH assay, and the results are displayed in Table 4.4. Among the tested working dispersions of RES alone, OHPP-RES SD, and HPP-RES SD at 15 and 30 µg/mL showed cell viability above 87.1% upon 2-h incubation, suggesting that RES (0.5% DMSO), OHPP-RES SD, and HPP-RES SD working dispersions were not toxic to the Caco-2 cells.

Table 4.4 Cell viability results of RES (0.5% DMSO), OHPP-RES SD, and HPP-RES SD with Caco-2 cells determined using the LDH assay.\*

RES Concentration (µg/mL)	Cell viability (%) <sup>*</sup>		
	RES (0.5% DMSO) <sup>1</sup>	OHPP-RES SD <sup>1</sup>	HPP-RES SD <sup>1</sup>
<b>15</b>	103.2±2.4 a	95.2±3.3 a	90.6±1.9 a
<b>30</b>	102.2±0.9 a	95.4±4.3 a	87.1±1.6 a

\*Percentage of survived cells was obtained after 2 h incubation with various RES (0.5% DMSO), OHPP-RES SD, or HPP-RES SD working dispersions in HBSS at 37°C.

<sup>1</sup> Values are expressed as % cell viability ± SD (n=3). Significant differences within RES (0.5% DMSO) group, OHPP-RES SD group, or HPP-RES SD group are denoted by different letters (p < 0.05).

Figure 4.7 showed the Caco-2 monolayer permeation of RES (0.5% DMSO), OHPP-RES SD, and HPP-RES SD. In general, when the loading concentration of RES was lower than RES intrinsic solubility (< 35.2 µg/mL), no significant difference of RES permeation was found among

RES (0.5%DMSO), OHPP-RES SD and HPP-RES SD. At loading RES content of 15  $\mu\text{g/mL}$  (7.5  $\mu\text{g/mL}$ ), RES permeation was 1.13, 1.33, and 1.07  $\mu\text{g/mL}$  for RES (0.5% DMSO), OHPP-RES SD and HPP-RES SD, respectively. At loading RES content of 30  $\mu\text{g/mL}$  (15  $\mu\text{g/mL}$ ), RES permeation was 3.70, 4.00, and 3.6  $\mu\text{g/mL}$  for RES (0.5% DMSO), OHPP-RES SD and HPP-RES SD, respectively. This result indicated that OHPP and HPP didn't delay the release of RES or hinder its Caco-2 cell monolayer permeation.

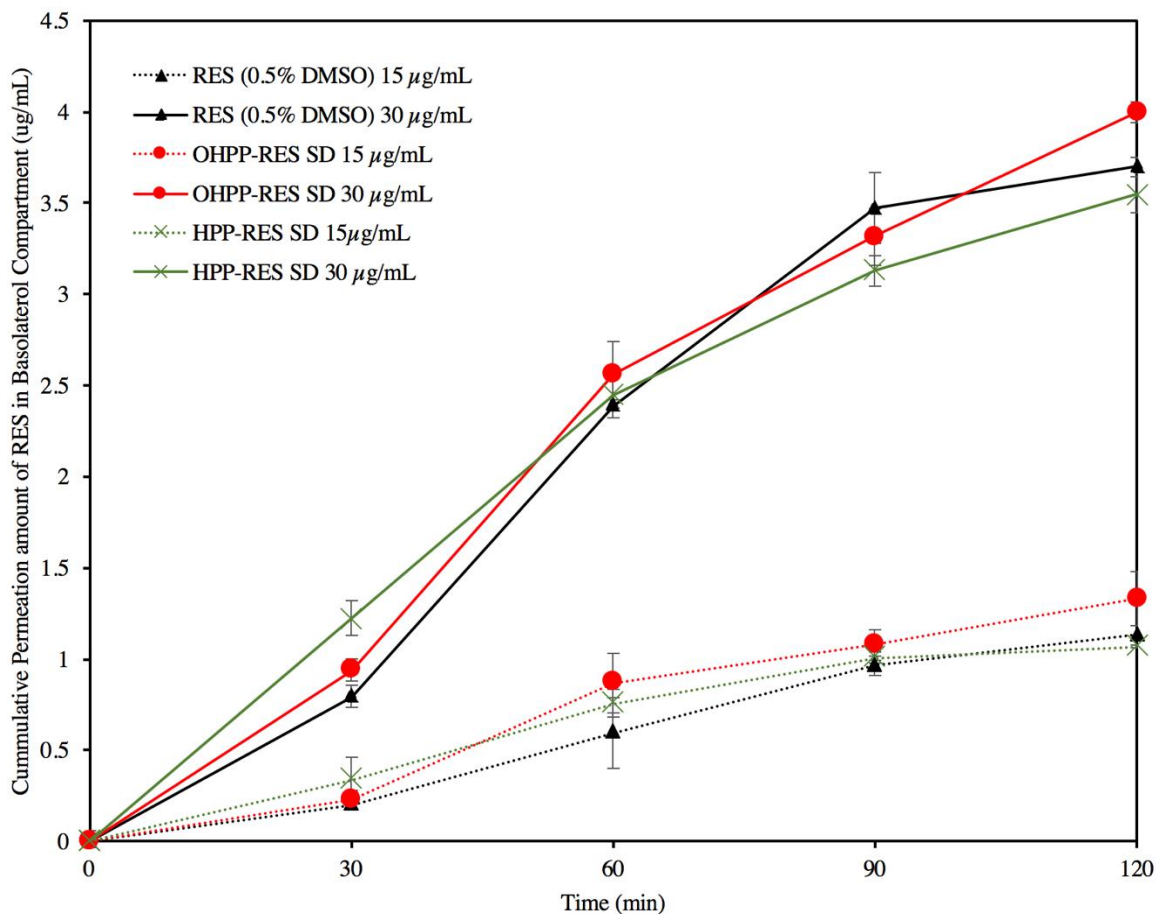


Figure 4.7 Cumulative RES permeations across the Caco-2 monolayers of RES (0.5% DMSO), OHPP-RES SD, or HPP-RES SD at different apical RES loading concentrations over 2-hour incubation. Red, green, and black lines represented the permeation of OHPP-RES SD, HPP-RES SD, and RES (0.5% DMSO), respectively. Solid, and dotted lines represented the permeation of loading amount of RES  $C_{RES}=30 \mu\text{g/mL}$  (15  $\mu\text{g/well}$  of RES), and RES  $C_{RES}=15 \mu\text{g/mL}$  (7.5  $\mu\text{g/well}$  of RES), respectively. Data was expressed as mean  $\pm$  SD (n = 3).

## 4.5 Conclusion

This study compared and evaluated HPP and OHPP structure, and their *in-vitro* performances in the delivery of RES. Our results indicated that both nanoparticles were capable to improve the soluble amount of RES, while dual modified particle OHPP showed superior performance.

It was revealed by X-ray powder diffraction analysis that RES was amorphorized upon incorporation with OHPP and HPP. In contrast, FTIR analysis suggested that both OS and HP functional groups allow OHPP to interact with RES via hydrogen-bonding, while only HP formed hydrogen bonds with RES molecules in HPP-RES SD. Owing to stronger interaction between RES and OHPP particle, OHPP-RES SD exhibited the highest soluble amount of RES, which was almost 20 and 4 times than that of HPP-RES SD and pure RES, respectively. HPP released only 90% of RES molecules throughout 3-hour dissolution, whereas almost 100% of RES was released from OHPP-RES SD in 10 minutes due to greater wettability conferred by OS groups. Noticeably, the release of RES was not compromised by OHPP-RES SD in Caco-2 experiment permeation model, and realized permeation at high RES loading concentration. The results showed that OHPP was more effective than HPP in increasing soluble amount and dissolution rate of RES. In addition, OHPP has shown considerable potential to solubilize RES and enable its biological efficacies. The study suggested that the desirable properties of PG as a natural polymer could be effectively enhanced by dual chemical modification.

## 4.6 Reference

- Abouelmagd, S. A., Sun, B., Chang, A. C., Ku, Y. J., & Yeo, Y. (2015). Release kinetics study of poorly water-soluble drugs from nanoparticles: are we doing it right?. *Molecular pharmaceutics*, 12(3), 997-1003.
- Almeida, L., M. Vaz-da-Silva, A. Falcao, E. Soares, R. Costa, A. I. Loureiro, C. Fernandes-Lopes, J. F. Rocha, T. Nunes, L. Wright & P. Soares-da-Silva. (2009). Pharmacokinetic and safety profile of trans-resveratrol in a rising multiple-dose study in healthy volunteers. *Molecular Nutrition & Food Research*, 53, S7-S15.
- Anjos, O., M. G. Campos, P. C. Ruiz & P. Antunes (2015) Application of FT-IR-ATR spectroscopy to the quantification of sugar in honey. *Food Chemistry*, 169, 218-223.

- Ariyantoro, A. R., Katsuno, N., & Nishizu, T. (2018). Effects of dual modification with succinylation and annealing on physicochemical, thermal and morphological properties of corn starch. *Foods*, 7(9), 133.
- Baile, C. A., J. Y. Yang, S. Rayalam, D. L. Hartzell, C. Y. Lai, C. Andersen & M. A. Della-Fera. (2011). Effect of resveratrol on fat mobilization. *Resveratrol and Health*, 1215, 40-47.
- Bertacche, V., N. Lorenzi, D. Nava, E. Pini & C. Sinco. (2006). Host-guest interaction study of resveratrol with natural and modified cyclodextrins. *Journal of Inclusion Phenomena and Macrocyclic Chemistry*, 55, 279-287.
- Boocock, D. J., G. E. S. Faust, K. R. Patel, A. M. Schinas, V. A. Brown, M. P. Ducharme, T. D. Booth, J. A. Crowell, M. Perloff, A. J. Gescher, W. P. Steward & D. E. Brenner. (2007). Phase I dose escalation pharmacokinetic study in healthy volunteers of resveratrol, a potential cancer chemopreventive agent. *Cancer Epidemiology Biomarkers & Prevention*, 16, 1246-1252.
- Chen, H., & Yao, Y. (2017). Phytoglycogen improves the water solubility and Caco-2 monolayer permeation of quercetin. *Food chemistry*, 221, 248-257.
- Chen, H., & Yao, Y. (2017a). Phytoglycogen to increase lutein solubility and its permeation through Caco-2 monolayer. *Food Research International*, 97, 258-264. *Food Research International*, 97, 258-264.
- Chen, H., Narsimhan, G., & Yao, Y. (2015). Particulate structure of phytoglycogen studied using  $\beta$ -amylolysis. *Carbohydrate polymers*, 132, 582-588.
- Chen, R. N., Ho, H. O., Yu, C. Y., & Sheu, M. T. (2010). Development of swelling/floating gastroretentive drug delivery system based on a combination of hydroxyethyl cellulose and sodium carboxymethyl cellulose for Losartan and its clinical relevance in healthy volunteers with CYP2C9 polymorphism. *European Journal of Pharmaceutical Sciences*, 39(1-3), 82-89.
- Dal Magro, C., Aguiar, G. P., Venerai, J. G., dos Santos, A. E., de Chaves, L. M., Oliveira, J. V., & Lanza, M. (2017). Co-precipitation of trans-resveratrol in PHBV using Solution Enhanced Dispersion by Supercritical Fluids technique. *The Journal of Supercritical Fluids*, 127, 182-190.

- Eguchi, N., Kawabata, K., & Goto, H. (2017). Electrochemical polymerization of 4, 4-dimethyl-2, 2guchi, N., Ka in concentrated polymer liquid crystal solution. *Journal of Materials Science and Chemical Engineering*, 5(02), 64.
- Fan, N., Z. G. He, P. P. Ma, X. Wang, C. Li, J. Sun, Y. H. Sun & J. Li. (2018). Impact of HPMC on inhibiting crystallization and improving permeability of curcumin amorphous solid dispersions. *Carbohydrate Polymers*, 181, 543-550.
- Fonseca-Florido, H. A., H. G. Vazquez-Garcia, G. Mendez-Montevalvo, U. A. Basilio-Cortes, R. Navarro-Cortes, M. L. Rodriguez-Marin, J. Castro-Rosas & C. A. Gomez-Aldapa (2018) Effect of acid hydrolysis and OSA esterification of waxy cassava starch on emulsifying properties in Pickering-type emulsions. *Lwt-Food Science and Technology*, 91, 258-264.
- Hao, J., Gao, Y., Zhao, J., Zhang, J., Li, Q., Zhao, Z., & Liu, J. (2015). Preparation and optimization of resveratrol nanosuspensions by antisolvent precipitation using Box-Behnken design. *Aaps Pharmscitech*, 16(1), 118-128.
- Hineno, M. (1977). Infrared spectra and normal vibration of  $\beta$ -d-glucopyranose. *Carbohydrate Research*, 56(2), 219-227.
- Higuchi, T., & Connors, K. A. (1965). Advances in analytical chemistry and instrumentation. *Phase Solubility Studies*, 117-212.
- Kanaujia, P., Poovizhi, P., Ng, W. K., & Tan, R. B. H. (2015). Amorphous formulations for dissolution and bioavailability enhancement of poorly soluble APIs. *Powder technology*, 285, 2-15.
- Isely, C., Hendley, M. A., Murphy, K. P., Kader, S., Annamalai, P., & Gower, R. M. (2019). Development of microparticles for controlled release of resveratrol to adipose tissue and the impact of drug loading on particle morphology and drug release. *International journal of pharmaceuticals*, 568, 118469.
- Liu, T., Müller, R. H., & Möschwitzer, J. P. (2017). Systematical investigation of a combinative particle size reduction technology for production of resveratrol nanosuspensions. *AAPS PharmSciTech*, 18(5), 1683-1691.
- Liu, T., Müller, R. H., & Möschwitzer, J. P. (2018). Consideration of the solid state for resveratrol nanocrystal production. *Powder Technology*, 332, 63-69.

- Mahdavinia, G. R., S. Etehad, M. Amini & M. Sabzi. (2015). Synthesis and characterization of hydroxypropyl methylcellulose-g-poly(acrylamide)/LAPONITE (R) RD nanocomposites as novel magnetic- and pH-sensitive carriers for controlled drug release. *Rsc Advances*, 5, 44516-44523.
- Masina, N., Choonara, Y. E., Kumar, P., du Toit, L. C., Govender, M., Indermun, S., & Pillay, V. (2017). A review of the chemical modification techniques of starch. *Carbohydrate polymers*, 157, 1226-1236.
- Merisko-Liversidge, E., Liversidge, G. G., & Cooper, E. R. (2003). Nanosizing: a formulation approach for poorly-water-soluble compounds. *European journal of pharmaceutical sciences*, 18(2), 113-120.
- Meuer, S., L. Braun, T. Schilling & R. Zentel. (2009). alpha-Pyrene polymer functionalized multiwalled carbon nanotubes: Solubility, stability and depletion phenomena. *Polymer*, 50, 154-160.
- Modi, S., & Anderson, B. D. (2013). Determination of drug release kinetics from nanoparticles: overcoming pitfalls of the dynamic dialysis method. *Molecular pharmaceuticals*, 10(8), 3076-3089.
- Nair, A. R., Lakshman, Y. D., Anand, V. S. K., Sree, K. N., Bhat, K., & Dengale, S. J. (2020). Overview of Extensively Employed Polymeric Carriers in Solid Dispersion Technology. *AAPS PharmSciTech*, 21(8), 1-20.
- Pandita, D., S. Kumar, N. Poonia & V. Lather (2014) Solid lipid nanoparticles enhance oral bioavailability of resveratrol, a natural polyphenol. *Food Research International*, 62, 1165-1174.
- Popova, M., Szegedi, A., Mavrodinova, V., Tušar, N. N., Mihály, J., Klébert, S., ... & Yoncheva, K. (2014). Preparation of resveratrol-loaded nanoporous silica materials with different structures. *Journal of Solid State Chemistry*, 219, 37-42.
- Pujara, N., Jambhrunkar, S., Wong, K. Y., McGuckin, M., & Popat, A. (2017). Enhanced colloidal stability, solubility and rapid dissolution of resveratrol by nanocomplexation with soy protein isolate. *Journal of colloid and interface science*, 488, 303-308.
- Scheffler, S. L., Huang, L., Bi, L., & Yao, Y. (2010). In vitro digestibility and emulsification properties of phytoglycogen octenyl succinate. *Journal of agricultural and food chemistry*, 58(8), 5140-5146.

- Serajuddin, A. T. M. (1999). Solid dispersion of poorly water-soluble drugs: Early promises, subsequent problems, and recent breakthroughs. *Journal of Pharmaceutical Sciences*, 88, 1058-1066.
- Singh, A. P., R. Singh, S. S. Verma, V. Rai, C. H. Kaschula, P. Maiti & S. C. Gupta. (2019). Health benefits of resveratrol: Evidence from clinical studies. *Medicinal Research Reviews*, 39, 1851-1891.
- Timmers, S., E. Konings, L. Bilet, R. H. Houtkooper, T. van de Weijer, G. H. Goossens, J. Hoeks, S. van der Krieken, D. Ryu, S. Kersten, E. Moonen-Kornips, M. K. C. Hesselink, I. Kunz, V. B. Schrauwen-Hinderling, E. E. Blaak, J. Auwerx & P. Schrauwen. (2011). Calorie Restriction-like Effects of 30 Days of Resveratrol Supplementation on Energy Metabolism and Metabolic Profile in Obese Humans. *Cell Metabolism*, 14, 612-622.
- Ubrich, N., Bouillot, P., Pellerin, C., Hoffman, M., & Maincent, P. (2004). Preparation and characterization of propranolol hydrochloride nanoparticles: a comparative study. *Journal of controlled release*, 97(2), 291-300.
- Van Eerdenbrugh, B. & L. S. Taylor. (2010). Small Scale Screening To Determine the Ability of Different Polymers To Inhibit Drug Crystallization upon Rapid Solvent Evaporation. *Molecular Pharmaceutics*, 7, 1328-1337.
- Wang, C., X. W. He, Q. Huang, X. Fu, F. X. Luo & L. Li. (2013). Distribution of Octenylsuccinic Substituents in Modified A and B Polymorph Starch Granules. *Journal of Agricultural and Food Chemistry*, 61, 12492-12498.
- Wegiel, L. A., L. I. Mosquera-Giraldo, L. J. Mauer, K. J. Edgar & L. S. Taylor. (2015). Phase Behavior of Resveratrol Solid Dispersions Upon Addition to Aqueous media. *Pharmaceutical Research*, 32, 3324-3337.
- Wegiel, L. A., L. J. Mauer, K. J. Edgar & L. S. Taylor. (2013). Crystallization of amorphous solid dispersions of resveratrol during preparation and storage-Impact of different polymers. *Journal of Pharmaceutical Sciences*, 102, 171-184.
- Xie, Y. & Y. Yao. (2018). Octenylsuccinate hydroxypropyl phytoglycogen enhances the solubility and in-vitro antitumor efficacy of niclosamide. *International Journal of Pharmaceutics*, 535, 157-163.

- Xie, Y., & Yao, Y. (2018b). Octenylsuccinate hydroxypropyl phytyglycogen, a dendrimer-like biopolymer, solubilizes poorly water-soluble active pharmaceutical ingredients. *Carbohydrate polymers*, 180, 29-37.
- Xie, Y., & Yao, Y. (2019). Incorporation with Dendrimer-Like Biopolymer Leads to Improved Soluble Amount and In Vitro Anticancer Efficacy of Paclitaxel. *Journal of pharmaceutical sciences*, 108(6), 1984-1990.
- Yano, K., Masaoka, Y., Kataoka, M., Sakuma, S., & Yamashita, S. (2010). Mechanisms of membrane transport of poorly soluble drugs: role of micelles in oral absorption processes. *Journal of pharmaceutical sciences*, 99(3), 1336-1345.
- Yerushalmi, N., & Margalit, R. (1994). Bioadhesive, collagen-modified liposomes: molecular and cellular level studies on the kinetics of drug release and on binding to cell monolayers. *Biochimica et Biophysica Acta (BBA)-Biomembranes*, 1189(1), 13-20.
- Zhang, X. P., Le, Y., Wang, J. X., Zhao, H., & Chen, J. F. (2013). Resveratrol nanodispersion with high stability and dissolution rate. *LWT-Food Science and Technology*, 50(2), 622-628.

## CHAPTER 5. PARTITIONING OF CCVJ IN OIL-WATER TWO-LAYER SYSTEM CONTAINING AMPHIPHILIC BIOPOLYMERS

### 5.1 Abstract

In this study, 9-(2-carboxy-2-cyanovinyl)-julolidine (CCVJ), a hydrophilic fluorescence molecular rotor, was used to characterize the impact of amphiphilic biopolymers, including starch octenylsuccinate (OSA-starch), sodium caseinate, and gum arabic on CCVJ water/oil partitioning, based on fluorescence emission intensity and peak wavelength ( $\lambda_{em\ max}$ ) values. For this study, an oil-water two-layer system was designed, where CCVJ was incorporated in the system through oil or aqueous phase. Fluorescence spectra showed that the partitioning of CCVJ was greater in water than in oil. To study the impact of biopolymers on CCVJ partitioning, the biopolymers were incorporated in the system through the aqueous phase, and CCVJ was incorporated into the oil phase. After 24-hour stabilization, the spectra showed that both OSA-starch and gum arabic reduced the transferring of CCVJ from oil to aqueous phase. The spectra of OSA-starch showed a major quantum yield at 492 nm, whereas gum arabic showed a broad band emission (from 462~492 nm) in the spectra. In contrast, the spectra of sodium caseinate didn't show any oil-to-aqueous phase transfer reduction of CCVJ, which resembled the spectra of sodium caseinate pure dispersion.

### 5.2 Introduction

A non-disruptive, rapid, and high-throughput *in-situ* method needs be developed, which can characterize the amphiphilic biopolymer structure and monitoring interfacial behavior. The physicochemical properties and stability of emulsion-based food product are substantially affected by the type and the number of amphiphilic biopolymers (Zhu et al., 2019; Dai et al., 2019; Gharehbeblou et al., 2019; Dickinson, 2003). There have been methods developed to inspect dynamic/static interfacial tension, *e.g.* maximum bubble pressure; pendant drop, spinning drop, etc. (Stauffer, 1965; Berry et al., 2015; Cayias et al., 1975; Carbonaro et al., 2019; Jiang et al., 2019), and others on inspecting interfacial rheological properties. Meanwhile, there have been methods focusing on examining emulsifier adsorption kinetics, *e.g.* ellipsometry (Bénarouche et al., 2017, Guzman et al., 2017; Miller et al., 2017), as well as the quantification of adsorbed

emulsifier, *e.g.* proteomics (Shen et al., 2020; Miriani et al., 2012). However, these methods have been associated with various limitations, such as low efficiency, lengthy adsorption time, poor accuracy, limited to protein-based matrix, emulsion disruption, and un-applicable to concentrated surfactant solutions or emulsion stabilized by electrostatic repulsion (Nazarov & Abdulhalim., 2020; Shen et al., 2020).

Molecular rotors (MRs) are a group of fluorophores that react to the increase in local viscosity (spatial restriction) with increasing emission intensity (Peng & Yao., 2020; Akers & Haidekker, 2004). With the property of non-disruptive, non-invasive, and highly sensitive features (Yu et al., 2016; Lai et al., 2015; Akers & Haidekker, 2004; Haidekker et al., 2001), viscosity-sensitive MR has become an attractive tool for various applications, *e.g.*, biomedical imaging (Mu et al., 2019; Dent et al., 2016; Yang et al., 2014), and mapping cellular organelles and biomolecules micro-viscosity (Zou et al., 2019; Haidekker & Theodorakis, 2016; López-Duarte et al., 2014; Kuimova., 2012).

CCVJ (9-(2-carboxy-2-cyanovinyl)-julolidine) is a hydrophilic molecular rotor. It has been employed to characterize polysaccharides (Peng & Yao, 2020; Hawe et al., 2010; Akers & Haidekker, 2004; Haidekker et al., 2001), proteins (Yu et al., 2016; Lai et al., 2015), phospholipids (Mustafic et al., 2010), and other biopolymers (Гульнов et al., 2016) in biological environment. Though CCVJ was mainly sensitive to the change in the viscosity of environment, the emission maximum remained sensitive to the polarity (Hawe et al., 2010; Haidekker et al., 2005a). In polar solvent, the transition of CCVJ from ground state to excited state generates a dipole moment, and the energy expended for polar solvent molecule re-orientation leads to a red-shift of emission wavelength. Therefore, the fluorescence spectra of CCVJ is also affected by the polarity of local environment, and the spectra emission peak ( $\lambda_{em\ max}$ ) can be used to identify the location of CCVJ molecules in a complex system.

In this study, we examined the interaction of molecular rotor CCVJ with selected biopolymers, and found that CCVJ is a dual polarity and viscosity probe of amphiphilic biopolymers in oil-water two-layer system. The outcome of this work provided a new platform in the exploration of biopolymers, in particular their properties at oil-water interface.

The hypothesis is that fluorescence spectra of molecular rotor CCVJ can be used to characterize the interfacial behavior of biopolymers based on shift of emission peak ( $\lambda_{em\ max}$ ). To

test the hypothesis, an oil-water two-layer system was designed to form an oil-water interface where CCVJ and biopolymers would be distributed among oil and aqueous phases. Starch-OS, PG-OS, gum arabic, and sodium caseinate were selected as model biopolymers. The impact of biopolymer structure and their interfacial arrangement on CCVJ partitioning were interpreted from the intensity of blue-shift.

### **5.3 Materials and Methods**

#### **5.3.1 Chemicals**

Octenylsuccinate starch (OSA-starch) and gum arabic were obtained from Ingredion (Chicago, IL). Sodium caseinate was kindly provided by company from industry. Molecular rotor CCVJ (9-(2-Carboxy-2-cyanovinyl) julolidine) ( $\geq 97.0\%$ ) was purchased from Sigma-Aldrich. Vegetable oil was purchased from local grocery store. Double-distilled water was used.

#### **5.3.2 Extraction of PG**

The extraction of PG was done according to the method described by Hua et al (2017).

#### **5.3.3 Preparation of Octenylsuccinate Phytoglycogen (PG-OS)**

Octenylsuccinate phytoglycogen (PG-OS) was prepared according to the method described by Scheffler (2010), where 1-octenyl succinate anhydride used was at the levels of 6% based on the dry weight of glucans.

#### **5.3.4 Preparation of Biopolymer Dispersions**

Precise amount of each of OSA-starch, PG-OS, gum arabic, and sodium caseinate was added in phosphate-buffered saline (PBS) (5 mM, pH 7) to form dispersions with concentrations ranging from 1.25 to 50 mg/mL. Pure PBS was used as blank control.

#### **5.3.5 Preparation of Biopolymer-CCVJ Dispersions**

Precisely weighted 5.0 mg CCVJ was dissolved in 0.50 mL DMSO (HPLC grade, Fisher Chemical, US). The dispersion with the volume of 0.1 mL was further diluted with 7.46 mL oil to

obtain the CCVJ stock oil solution (0.50 mM). Another DMSO dissolved CCVJ solution of 0.1 mL was diluted with 7.46 mL PBS to obtain the CCVJ stock aqueous solution (0.50 mM).

In each 1-mL capped polypropylene centrifuge tube, 10  $\mu\text{L}$  CCVJ aqueous stock solution and 990  $\mu\text{L}$  biopolymer dispersion were mixed to form biopolymer-CCVJ dispersion. For aqueous and oil controls, 10  $\mu\text{L}$  CCVJ aqueous or oil stock solution was mixed with 990  $\mu\text{L}$  PBS or oil, respectively, yielding working solutions containing 5.0  $\mu\text{M}$  CCVJ in PBS or oil. To equilibrate CCVJ-containing solutions or dispersions, capped tubes were wrapped with aluminum foil and agitated in a shaking water bath (70 rpm) overnight at room temperature. Thereafter, a 200  $\mu\text{L}$  aliquot of each fluid was added in triplicate in 96-well microplates for fluorescence measurements.

### **5.3.6 Preparation of Oil-water Two-layer System Containing CCVJ**

To investigate the partitioning of CCVJ between oil and aqueous phases, an oil-water two-layer system that contains an oil phase (42 mg) on the top of a PBS layer (200  $\mu\text{L}$ ) was designed. For the first group, CCVJ was delivered to the two-layer system from the oil phase. Firstly, 200  $\mu\text{L}$  PBS was added to a well of a microplate, thereafter, 42 mg CCVJ oil working solution with CCVJ concentration of 10.94  $\mu\text{M}$  (0.134  $\mu\text{g}/\text{well}$ ), 21.88  $\mu\text{M}$  (0.268  $\mu\text{g}/\text{well}$ ), 43.76  $\mu\text{M}$  (0.537  $\mu\text{g}/\text{well}$ ) and 65.64  $\mu\text{M}$  (0.537  $\mu\text{g}/\text{well}$ ) in oil were added on the top of the aqueous (PBS) layer. At time points of 0.5, 1, 4, and 24 h, the two-layer systems were subjected to fluorescence measurement.

To study the impact of biopolymers on the partition of CCVJ, two-layer systems were formed with biopolymer dispersions and CCVJ oil working solution and the fluorescence was measured at 0.5 and 24 h.

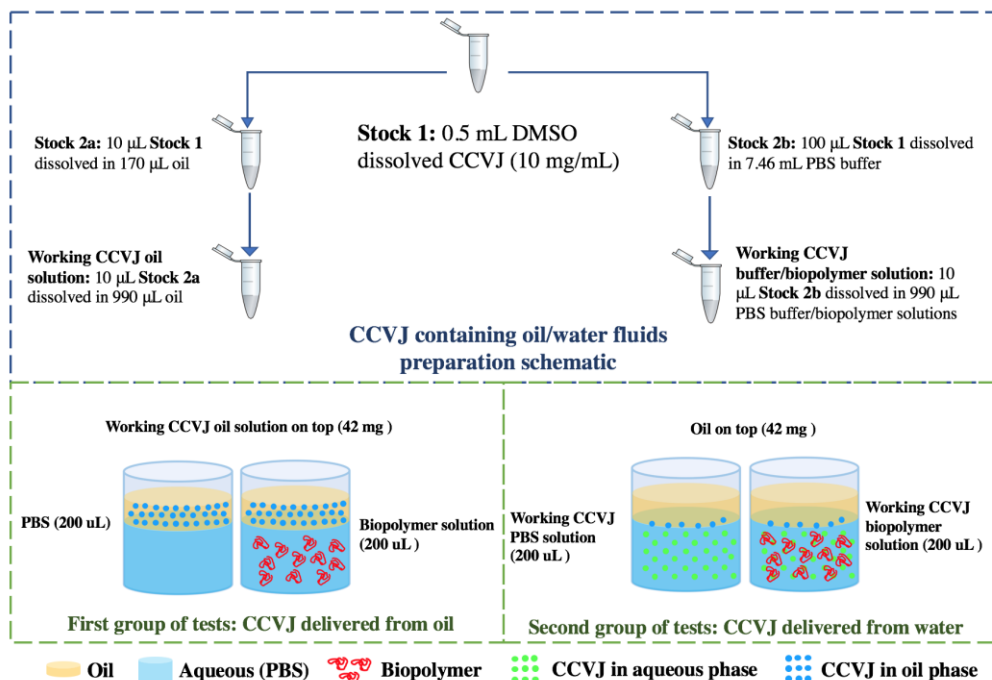


Figure 5.1 Schematic showing the preparation of CCVJ containing oil-water two-layer systems. Oil phase was on the top of the aqueous layer. For the first group (CCVJ delivered from the oil phase), the final concentration of CCVJ in working CCVJ oil solution on top (42 mg) was 21.88  $\mu\text{M}$  (0.268  $\mu\text{g}/\text{well}$ ) in oil. For the second group (CCVJ delivered from the oil phase), the final concentration of CCVJ in working CCVJ PBS solution was 5  $\mu\text{M}$  (0.268  $\mu\text{g}/\text{well}$ ) in PBS.

For the second group, CCVJ was delivered to the two-layer system from the aqueous phase. Firstly, 200  $\mu\text{L}$  CCVJ PBS working solution with CCVJ concentrations of 2.5  $\mu\text{M}$  (0.134  $\mu\text{g}/\text{well}$ ), 5  $\mu\text{M}$  (0.268  $\mu\text{g}/\text{well}$ ), 10  $\mu\text{M}$  (0.537  $\mu\text{g}/\text{well}$ ) and 15  $\mu\text{M}$  (0.537  $\mu\text{g}/\text{well}$ ) in PBS were transferred into a microplate well. Afterwards, pure oil (42 mg) was dispensed on the top of buffer layer. The plate was subjected to fluorescence measurement at 0.5, 1, 4, and 24 h.

To study the impact of biopolymer on the partition of CCVJ, the two-layer system was formed using oil and biopolymer-CCVJ dispersion. The fluorescence measured was conducted with the biopolymer containing two-layer system at 0.5 and 24 h.

### 5.3.7 Fluorescence Measurement

The Fluorescence measurement with 96-well microplates (Greiner Bio-one, Germany) were conducted using a Synergy H1 Hybrid Multi-mode Reader (BioTek, US) in the top-read mode with 7 mm read height. For each formulation, triplicate wells were prepared and measured.

The excitation wavelength was set at 420 nm and the emission spectra scanning was set from 450 to 650 nm with a bandwidth of 2 nm.

### 5.3.8 Statistical Analysis

Experiments were performed in triplicate. Results were expressed as mean  $\pm$  standard deviation. One-way ANOVA was performed for significant difference analysis using SPSS for Windows (version rel. 10.0.5, 1999, SPSS Inc., Chicago, IL, USA). P-value  $\leq$  0.05 was used to identify significant differences between results.

## 5.4 Results and Discussions

### 5.4.1 CCVJ fluorescence emission in oil and aqueous phases

Single-phase system that contained CCVJ in oil phase and water phase (PBS buffer) was characterized first. Figure 5.2 A and B show the observed fluorescence emission spectra of CCVJ in oil and PBS, respectively. The result indicated that, in oil, CCVJ fluorescence emission peak maximum ( $\lambda_{em\ max}$ ) was blue-shifted (shifted to shorter wavelength) at greater extent and with much higher emission intensity than in PBS. The impact of oil/buffer on fluorescence peak intensity and peak maximum ( $\lambda_{em\ max}$ ) was examined.

In general, Figure 5.2 showed that the emission intensity was substantially higher in oil than in PBS. For example, at CCVJ concentration of 2.5  $\mu$ M, the emission intensity of CCVJ was  $\sim$ 52000 OFE in oil, which was 8 times higher than that in PBS ( $\sim$ 6600 OFE). In PBS, 2.5 to 15  $\mu$ M CCVJ led to emission intensity of  $\sim$ 6600 to 21300 OFE. The embedded graph in Figure 5.2B indicated that the observed fluorescence emission intensity increased linearly (slope=1163.1,  $R^2=0.999$ ) with increasing CCVJ concentration (from 2.5 to 15  $\mu$ M) in PBS. Noticeably, 5  $\mu$ M or higher of CCVJ in oil led to emission peak intensities out of the detection limit. In addition, oil/buffer has appreciable impact on peak maximum of CCVJ. Figure 5.2 showed that the peak emission maximum of CCVJ located at 460 nm in oil and 496 nm in PBS.

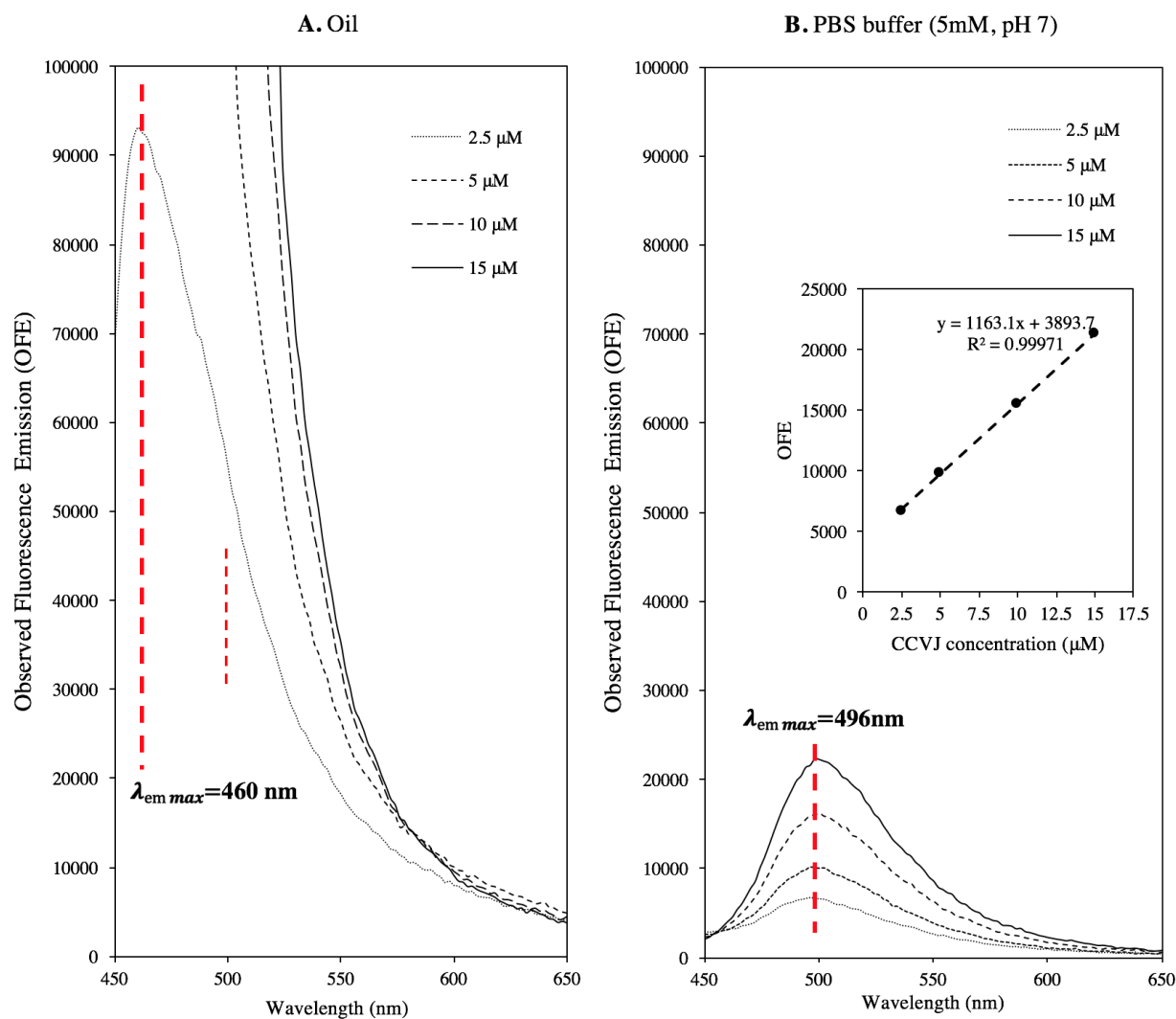


Figure 5.2 The observed fluorescence emission spectra of CCVJ at concentrations from 2.5 to 15  $\mu\text{M}$  in oil (**A**) and PBS (**B**) are shown. The embedded graph in **B** shows the OFE intensity of CCVJ in PBS at CCVJ concentration of 2.5, 5, 10, and 15  $\mu\text{M}$ , and the fitted curves were shown in dotted lines.

In oil, the viscous nature (inter-particulate interactions among long chain triglycerides) retarded TICT relaxation (non-radiative process), led to much enhanced fluorescence intensity (Toliautas et al., 2019). In contrast, the reduced fluorescence emission of PBS was attributed to the strong quenching of CCVJ by water molecules.

The difference in  $\lambda_{em\ max}$  between oil and PBS was possibly attributed to their different polarity. As indicated by Haidekker et al. (2005), after photo-excitation of CCVJ molecule, a dipole moment between the ground and excited state is generated.

High concentration of fluorophore lead to dimer, tetramer formation, inner-filter effects, (Würthner et al., 2002). The linear relationship between the CCVJ concentration ( $\mu\text{M}$ ) and the fluorescence emission intensity in PBS indicated that the CCVJ concentration range of 2.5~15  $\mu\text{M}$  exhibited negligible inner filter effect, and no aggregation or complexes formation was observed for CCVJ molecules. Therefore, the applied concentration range of CCVJ can be used to measure the concentration of the dissolved compound.

The large difference in emission intensity and the difference of peak location between oil and aqueous system allows for high-sensitivity detection of CCVJ partitioning in oil and water phases as well as the impact of biopolymers on such CCVJ partitioning.

#### **5.4.2 CCVJ partitioning in oil-water two-layer system**

To examine the partition of CCVJ between oil and aqueous phase, CCVJ was delivered to the oil-water two-layer system either from the aqueous phase at CCVJ concentration of 2.5  $\mu\text{M}$  (0.134  $\mu\text{g/well}$ ), 5  $\mu\text{M}$  (0.268  $\mu\text{g/well}$ ), 10  $\mu\text{M}$  (0.537  $\mu\text{g/well}$ ) and 15  $\mu\text{M}$  (0.537  $\mu\text{g/well}$ ) in PBS, or from the oil phase at CCVJ concentration of 10.94  $\mu\text{M}$  (0.134  $\mu\text{g/well}$ ), 21.88  $\mu\text{M}$  (0.268  $\mu\text{g/well}$ ), 43.76  $\mu\text{M}$  (0.537  $\mu\text{g/well}$ ) and 65.64  $\mu\text{M}$  (0.537  $\mu\text{g/well}$ ) in oil. The total amount of CCVJ/well in both delivery approaches were the same. The fluorescence emission scan was performed on the CCVJ containing oil-water two-layer system at stabilization time of 0.5, 1, 4 and 24 h, and the observed CCVJ emission spectra were displayed in Figure 5.3. In general, the results showed that over 24-h stabilization, CCVJ preferred to either stay or partition into the aqueous phase.

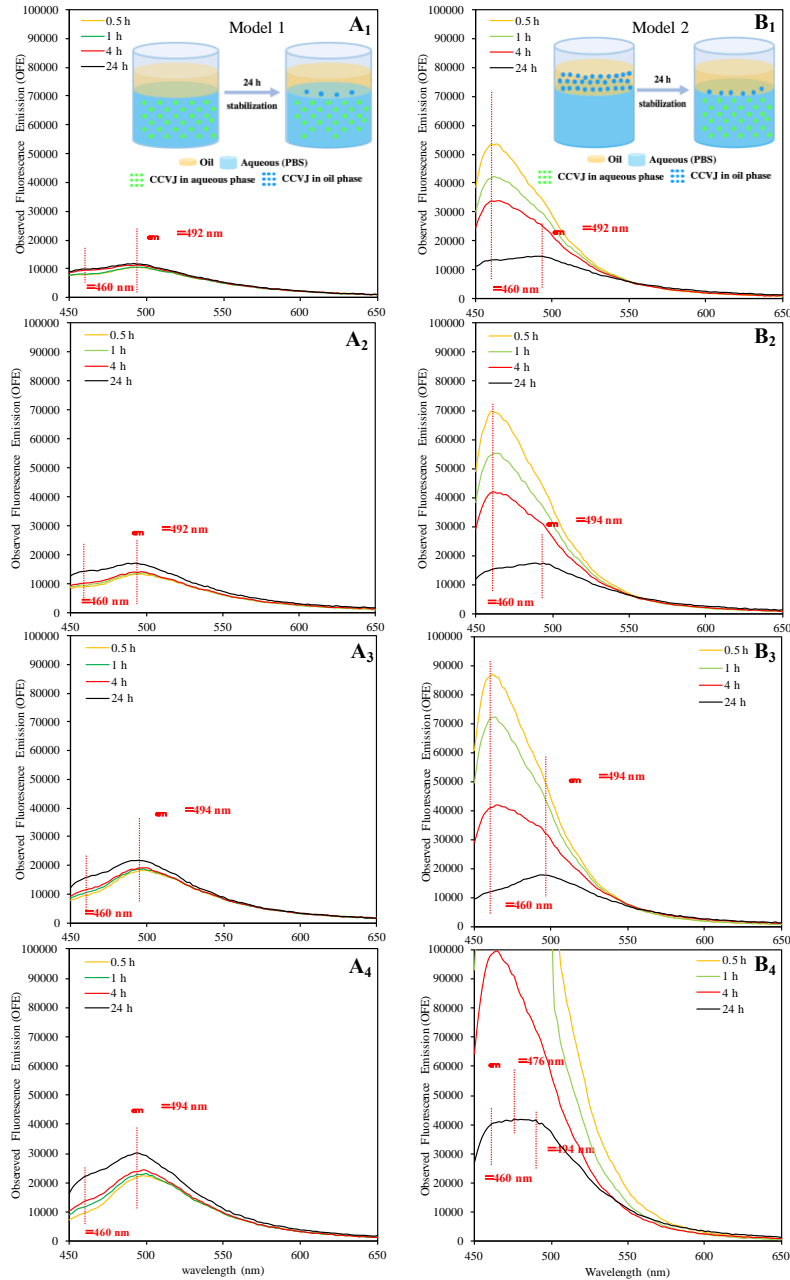


Figure 5.3 The change of observed fluorescence emission spectra of CCVJ in the oil-water two-layer system over 24 h. CCVJ was delivered from PBS (A<sub>1,2,3,4</sub>) or oil (B<sub>1,2,3,4</sub>) to the two-layer system (the total amount of CCVJ delivered to the system were the same in both delivery approaches). In the group that CCVJ was delivered from PBS, the concentrations of CCVJ in the aqueous phase for A<sub>1</sub>, A<sub>2</sub>, A<sub>3</sub>, and A<sub>4</sub> were 2.5 (0.134  $\mu\text{g}/\text{well}$ ), 5 (0.268  $\mu\text{g}/\text{well}$ ), 10 (0.537  $\mu\text{g}/\text{well}$ ), and 15  $\mu\text{M}$  (0.537  $\mu\text{g}/\text{well}$ ), respectively. In the group that CCVJ was delivered from oil, the concentrations of CCVJ in the oil phase for B<sub>1</sub>, B<sub>2</sub>, B<sub>3</sub>, and B<sub>4</sub> were 10.94 (0.134  $\mu\text{g}/\text{well}$ ), 21.88 (0.268  $\mu\text{g}/\text{well}$ ), 43.76 (0.537  $\mu\text{g}/\text{well}$ ) and 65.64  $\mu\text{M}$  (0.537  $\mu\text{g}/\text{well}$ ), respectively.

When CCVJ was delivered to the oil-water two-layer system from the aqueous phase. In general, the emission intensity at  $\lambda_{em\ max}$  increased as the concentration of CCVJ increased. Figure 5.3A<sub>1,2,3,4</sub> showed that CCVJ spectra (both emission peak location and intensity) of 0.5, 1, 4 and 24 h were essentially the same, suggesting that CCVJ molecules remained in the PBS layer. However, after 24-h, a little shoulder appeared at around 460 nm, along with a slight blue-shift of their  $\lambda_{em\ max}$  compared with the spectra of 0.5, 1, and 4-h. For example, the emission intensity of 24-h at  $\lambda_{460\ nm}$  increased by 150~1800, 4000~5000, 4200~6000, and 9000~12000 OFE for CCVJ PBS concentration of 2.5, 5, 10, and 15  $\mu\text{M}$ , respectively (Figure 5.3A<sub>1,2,3,4</sub>). The  $\lambda_{em\ max}$  located at 496 nm for all spectra of 0.5-h. Subsequently, the  $\lambda_{em\ max}$  shifted to 492, 492, 494, and 494 nm after 24-h stabilization for CCVJ concentration of 2.5, 5, 10, and 15  $\mu\text{M}$ , respectively (Figure 5.3A<sub>1,2,3,4</sub>). The changes in the spectra indicated the partitioning of a minor amount of CCVJ into the oil phase.

When CCVJ was delivered to the two-layer system from oil, 0.5-h spectra of Figure 5.3B<sub>1,2,3,4</sub> all showed prominent peak at 460 nm, indicating that majority of the CCVJ remained in the oil phase. From 0.5 to 4h, shoulders started to form at higher wavelength. After 24 h, the peak maximum of CCVJ emission shifted to 492~494 nm while the emission intensity was significantly reduced. For example, at CCVJ concentration of 5  $\mu\text{M}$  (Figure 5.3B<sub>2</sub>), during the 24 h monitoring, the peak location of CCVJ emission shifted from 460 to 494 nm (red-shift) while the emission intensity was reduced from ~70000 to ~20000 RFE. The changes in spectra suggested the partitioning of a large amount of CCVJ into the aqueous phase from oil. Indeed, the 24-h spectra were essentially the same between two approaches of CCVJ delivery. The preferential partitioning of CCVJ into the aqueous phase was attributed to its hydrophilicity. The remaining CCVJ in the oil phase is due to the julolidine base in the structure (Akers & Haidekker, 2004). Noticeably, there was no distinguishable emission peak for CCVJ of 65.64  $\mu\text{M}$  (0.537  $\mu\text{g}/\text{well}$ ) in oil (Figure 5.3B<sub>4</sub>). Instead, a broad emission band ranging from 460 ~ 494 nm was formed. This indicated that 24 h was insufficient to stabilize the system with high concentration of CCVJ delivered from oil.

### 5.4.3 Impact of biopolymer on the spectra of CCVJ fluorescence emission

The fluorescence emission scan was performed with respect to CCVJ in OSA-starch, PG-OS, gum arabic and sodium caseinate aqueous dispersions, respectively. The observed CCVJ emission spectra for each biopolymer were displayed in Figure 5.4.

Figure 5.4 showed that, for each type of biopolymer, the respective emission intensity increased monotonically with respect to the biopolymer concentration. For some of the biopolymers, the biopolymer concentration exceeding a specific value result in that the spectral peak of the RFE intensity was beyond the maximum read (100,000 RFE). For example, for OSA-starch and PG-OS, the spectral peak was un-detectable at concentration of 50 mg/mL. As for sodium caseinate, the spectral peak can be detected only with concentration of 1.25 mg/mL and 2.5 mg/mL.

The details of the magnitude of the spectral peak was examined, and their relation to the biopolymer concentration were plotted in Figure 5.5. It was observed that, at all concentration levels, CCVJ produced the weakest fluorescence signal in gum arabic, but the strongest in sodium caseinate. For example, at 2.5 mg/mL concentration, the observed peak OFE intensity was ~12000 for gum arabic, ~17000 for PG-OS, ~21000 for starch-OS and ~70000 for sodium caseinate. Finally, similar spectra were seen for PG-OS and OSA-starch.

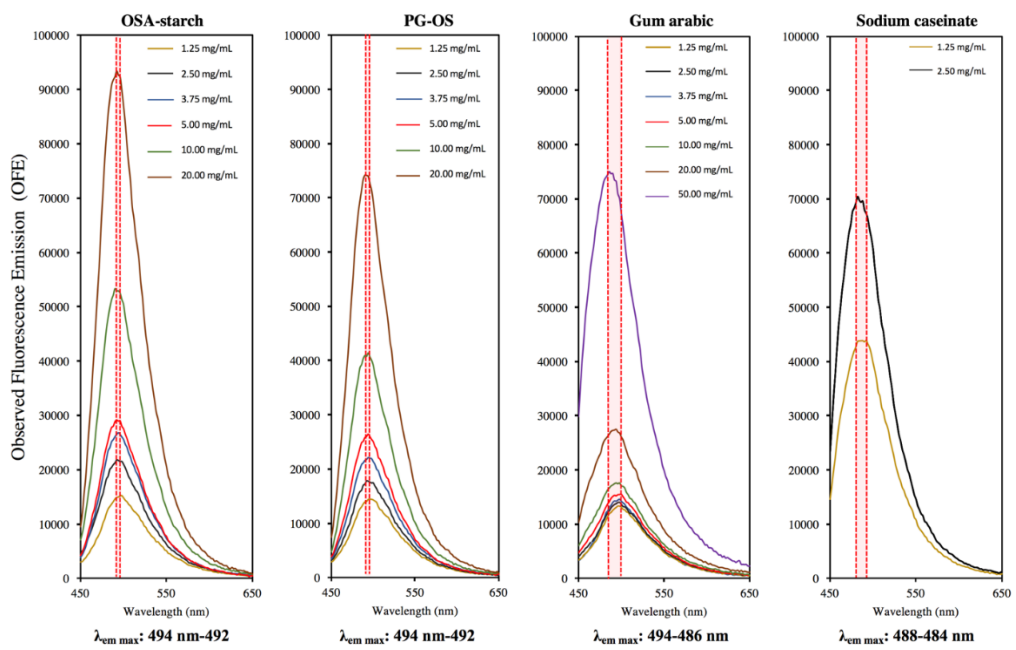


Figure 5.4 The observed fluorescence emission spectra of CCVJ in OSA-starch, PG-OS, gum arabic, and sodium caseinate aqueous dispersions. For each biopolymer, only emission spectra within detectable emission intensity range are displayed in the figure. In each group, from bottom to top, the concentrations of biopolymer were: (1) 1.25, 2.5, 3.75, 5, 10, and 20 mg/mL for OSA-starch, (2) 1.25, 2.5, 3.75, 5, 10, and 20 mg/mL for PG-OS, (3) 1.25, 2.5, 3.75, 5, 10, 20, and 50 mg/mL for gum arabic, and (4) 1.25, and 2.5 mg/mL for sodium caseinate. The red-shaded area indicates the change of the peak maximum ( $\lambda_{em\ max}$ ), with its value provided at the bottom of graph for each biopolymer.

Noticeably, a linear response between biopolymer concentration and emission intensity was obtained at low biopolymer concentrations (1~ 5 mg/mL), the results were displayed in the embedded graph of Figure 5.5. Explicitly, the trend-line slopes of polymers were in the order of sodium caseinate (slop= $2.52 \times 10^7$ ,  $R^2=0.99$ ) > OSA-starch (slop= $3.90 \times 10^6$ ,  $R^2=0.99$ ) > PG-OS (slop= $3.00 \times 10^6$ ,  $R^2=0.99$ ) > gum arabic (slop= $1.00 \times 10^6$ ,  $R^2=0.88$ ). For gum arabic dispersions, the OFE intensity was relatively low, around ~ 14000-15900 RFE. On the other hand, the gradient fluorescence (50000- 70000 RFU) in diluted sodium caseinate dispersions was the strongest among all polymers tested, indicating that sodium caseinate provided greater spatial restrictions than the other 3 polymers. In addition, the plots of OSA-starch and PG-OS were quite similar, indicating that the two biopolymer has alike structure that imposed similar level of spatial restriction for CCVJ (Peng & Yao., 2020; Haidekker et al., 2005). This result indicated that the fluorescence of CCVJ can be used to effectively differentiate the nano-structures based on their spatial restriction on CCVJ intramolecular twisting.

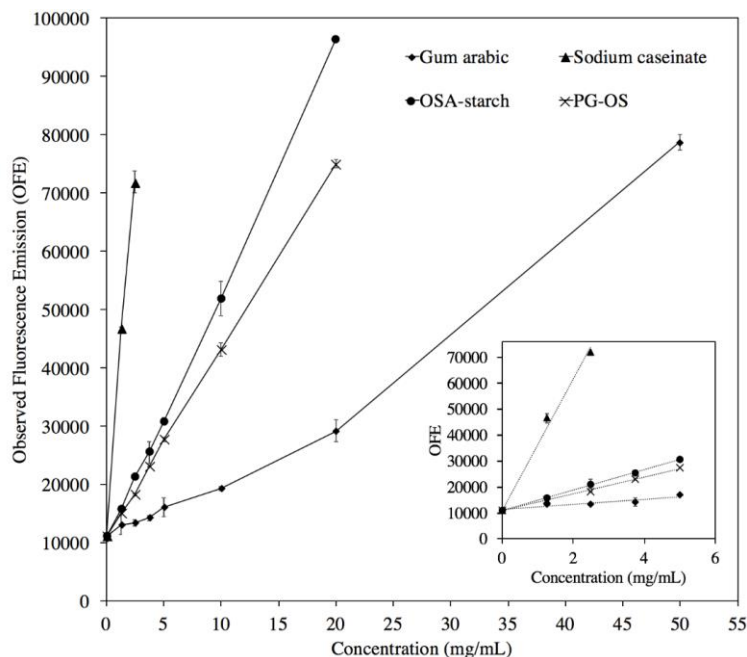


Figure 5.5 The emission intensity (OFEs were obtained at  $\lambda_{em\ max}$  of biopolymer dispersions) as a function of biopolymer concentration (mg/mL) in aqueous dispersion. For each biopolymer, the concentrations of ranges were: (1) 1.25~ 20 mg/mL for OSA-starch and PG-OS; (2) 1.25~ 50 mg/mL for gum arabic, and (3) 1.25~ 2.5 mg/mL for sodium caseinate. The embedded figure showed the observed fluorescence emission intensity (OFE were obtained at  $\lambda_{em\ max}=494\ nm$  for OSA-starch, PG-OS and gum arabic dispersions, and  $\lambda_{em\ max}=488\ nm$  for sodium caseinate dispersions) at biopolymer concentration of 0~5.0 mg/mL, and the fitted curves were shown in dotted lines.

Examining with detail, the relation between the biopolymer concentration and the peak maximum ( $\lambda_{em\ max}$ ) was plotted in Figure 5.6 for the selected biopolymers. In general, the peak maximums of biopolymer dispersions were all blue-shifted compared to that of PBS buffer, and the result showed that the extend of shifting was affect by the type of polymer and concentration.

Firstly, Figure 5.6 showed the influence of polymer concentration on the peak location, and it was observed that all biopolymers showed concentration-dependent increase in the magnitude of blue-shift. For example, the spectra of low concentrations (1.0 ~ 5.0 mg/mL) OSA-starch, PG-OS and gum arabic dispersions exhibited no blue-shift compared to that of PBS buffer. For more concentrated dispersions (>10 mg/mL) of OSA-starch and PG-OS, a very minor drifting in the  $\lambda_{em\ max}$  of 2 nm was observed ( $\lambda_{em\ max}$  values reduced from 494 to 492 nm). In addition, an increase in gum arabic concentration resulted in a progressive increase in blue-shift, reaching a wavelength of 486 nm at 50 mg/mL ( $\lambda_{em\ max}$  values reduced from 494 to 486 nm). Similar trend was found in sodium caseinate, where  $\lambda_{em\ max}$  values reduced from 488 to 484nm as concentration increased. The results revealed that higher concentration of dispersed biopolymer led to stronger blue-shift of CCVJ peak location. Moreover, the impact of biopolymer type on the  $\lambda_{em\ max}$  was evaluated, and the results were presented in Figure 5.6. We found that, within the tested concentration range, the blue-shifting rate was in the order of PG-OS<OSA-starch < gum arabic < sodium caseinate

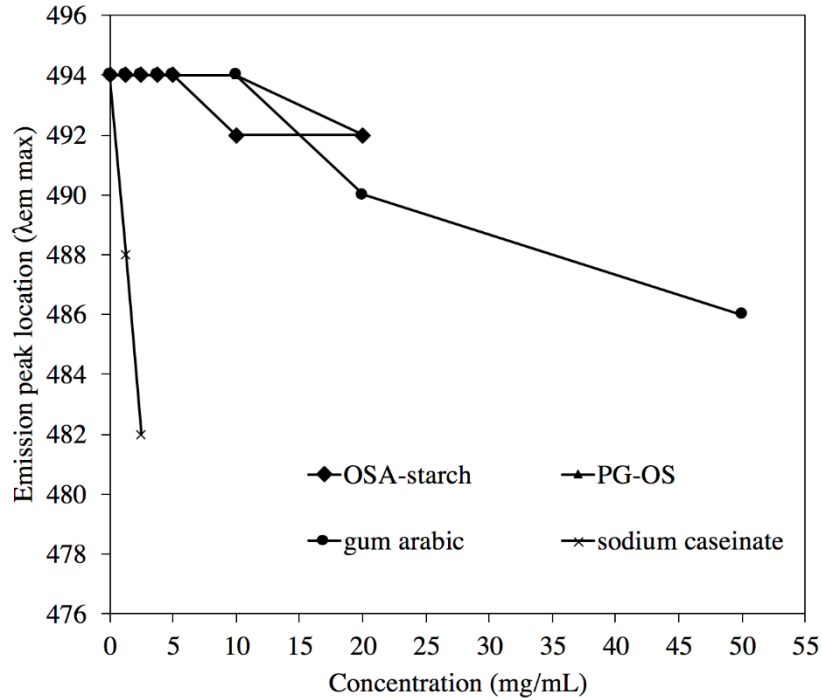


Figure 5.6 Wavelength of emission peak location ( $\lambda_{em\ max}$ ) as a function of biopolymer concentration (mg/mL) in aqueous dispersion. For each biopolymer, the concentrations of ranges were: (1) 1.25~ 20 mg/mL for OSA-starch and PG-OS; (2) 1.25~ 50 mg/mL for gum arabic, and (3) 1.25~ 2.5 mg/mL for sodium caseinate.

CCVJ emits blue-shifted fluorescence in more hydrophobic domain, therefore, more concentrated polymer dispersion brought more non-polar regions for CCVJ to reside and produced blue-shift at higher extend. In addition, we considered the ranking of blue-shifting rate was attributed to the hydrophobicity and the amount of the nano-cavities provided by the biopolymer. The glucan chain network of OSA-starch and PG-OS was only able to provide slightly hydrophobic nano-cavities for CCVJ. In contrast, sodium caseinate contained large amount of protein ‘nano-pockets’ and aggregates, which contributed much higher amount of non-polar nano-cavities to host CCVJ. For gum arabic, the low emission intensity indicated that the short glucan branches cannot form sufficient cavities to host and restriction the twisting of CCVJ. Therefore, the CCVJ molecule was possibly associated with the hydrophobic region of glycoprotein. Due to the low protein content (2-3% protein in gum arabic) gum arabic provided reduced amount of non-polar domain compared to sodium caseinate. (Akers & Haidekker, 2004; Haidekker et al., 2005; Haidekker et al., 2005a; Hawe, et al., 2010).

As a result, the structure information (*e.g.* hydrophobicity, spatial restriction, etc.) can be derived from the analysis of emission intensity and peak location. Therefore, the emission spectra allowed the differentiation and probing of biopolymer in aqueous dispersion.

#### **5.4.4 Impact of biopolymer on the spectra of CCVJ fluorescence emission in oil-water two-layer system**

The impact of biopolymer on CCVJ emission spectra in oil-water two-layer system was further examined. To investigate the biopolymer effects on CCVJ water-partitioning, a group of experiments were conducted through delivering CCVJ from the oil phase and the biopolymer from aqueous phase. After the delivering, the observed fluorescence emission (OFE) spectra were recorded, and the result at stabilization time of 0.5-h and 24-h were presented in the middle column of Figure 5.7. As a reference, the spectra of biopolymer aqueous dispersions were presented in the right column of Figure 5.7.

For all biopolymers, the spectra showed prominent peaks at 462 nm at 0.5 h, indicating the presence of CCVJ in oil. Furthermore, the peaks for all polymers exhibited a significant red-shift along with reduced RFE intensity after 24-h stabilization, suggesting the occurrence of CCVJ water-partitioning. For example, Figure 5.7A<sub>2</sub> showed that OSA-starch peak locations were red-shifted from 462 to 492 nm along with a decrease in RFE intensity (from ~90000 to ~30000 RFE) in stabilization time from 0.5-h to 24-h. Comparing with the spectra of OSA-starch aqueous dispersion, after 24-h the spectrum from the oil-water two-layer system became nearly identical to that from aqueous dispersion. Comparing with the spectra of OSA-starch aqueous dispersion, after 24-h the spectrum from the oil-water two-layer system becomes nearly identical to that from aqueous dispersion (Figure 5.7A<sub>3</sub>). For the other three biopolymers, similar trends were observed in their corresponding 24-h stabilized spectra (Figure 5.7B<sub>2</sub>, C<sub>2</sub> and D<sub>2</sub>). For CCVJ in aqueous dispersion of PG-OS, gum arabic and sodium caseinate, their spectral peaks location was at 494nm, 494nm and 482nm, respectively (Figure 5.7B<sub>3</sub>, C<sub>3</sub> and D<sub>3</sub>). The peak locations and emission intensities of CCVJ in their aqueous dispersions were comparable to their 24-h stabilized spectra (Figure 5.7). Consequently, it was anticipated that there was a strong water-partitioning of CCVJ after 24-h stabilization, and yielded a spectrum similar to that of aqueous biopolymer dispersion. Alternatively, majority of CCVJ molecules moved into the aqueous phase.

Further comparing with the spectra of the aqueous dispersions (Figure 5.7A<sub>3</sub>, B<sub>3</sub>, C<sub>3</sub> and

D<sub>3</sub>), it was observed that an enhancement of RFE intensity at a shorter wavelength emerged after 24-h. The level of enhancement was dependent on the type of biopolymer. For OSA-starch and PG-OS at 24-h (Figure 5.7A<sub>2</sub> and B<sub>2</sub>), the intensity enhancement at wavelength around 462nm was ascertained, although rather weak. For gum arabic at 24-h (Figure 5.7C<sub>2</sub>), a strong enhancement at around 462nm was observed, which formed a broad band spectrum over wavelength range 462~492 nm (highlighted by the red shade). Noticeably, nearly no spectral broadening was observed for sodium caseinate (Figure 5.7D<sub>2</sub>) at 24-h, which was identical to its corresponding aqueous dispersion.

Considering that CCVJ in oil produced a spectral peak at 462 nm, the magnitude enhancement at 462 nm indicated that a portion of CCVJ remained in the oil phase after 24-h. Therefore, it was anticipated that there exists interaction between CCVJ and biopolymer that governed the water-partitioning of CCVJ. For sodium caseinate, for example, Akers & Haidekker (2004) demonstrates that the biopolymer in aqueous phase produced strong protein-CCVJ interaction that removed CCVJ from the surrounding solvent, thus yielded spectra identical to those in aqueous dispersion. For OSA-starch/PG-OS and gum arabic, a noticeable RFE intensity enhanced at 462 ~492 nm of 24-h suggested the delay of CCVJ water-partitioning, though the broadening of spectrum was relatively more prominent in gum arabic.

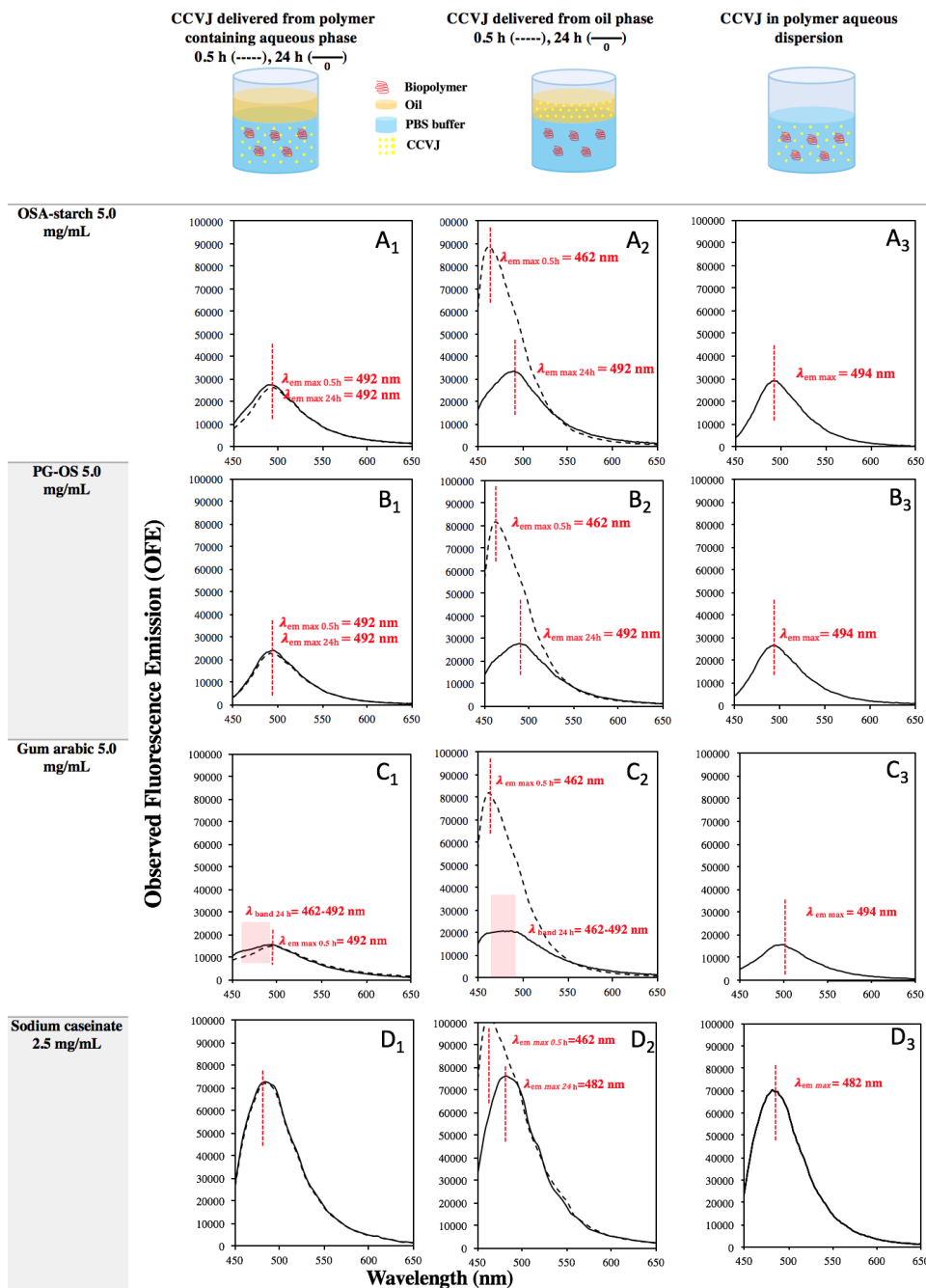


Figure 5.7 The observed fluorescence emission (OFE) spectra ( $\lambda_{\text{ex}} = 420 \text{ nm}$ ,  $\lambda_{\text{em}} = 450 \sim 650 \text{ nm}$ ) of CCVJ in oil-water two-layer system in the presence of biopolymers with concentration ranges of 2.5 ~ 5 mg/mL for OSA-starch, PG-OS, gum arabic, and sodium caseinate. The schematic on top showed the experiment setup which was composed of oil phase (on top) and aqueous phase with biopolymer (on the bottom). Two experimental conditions were tested: 1) CCVJ was delivered from water phase (left column), and 2) CCVJ was delivered from oil phase (middle column). Emission spectra of 0.5-h stabilization (dashed lines), and 24-h stabilization (solid lines) were recorded. Red shaded area indicated that the fluorescence was observed as emission intensity over a band of wavelengths instead of a peak.

To further examine the biopolymer impact on the oil-partitioning of CCVJ, another group of experiments were conducted with both CCVJ and biopolymer delivered from the aqueous phase. The results of CCVJ emission spectra were presented in the left column of Figure 5.7. Obviously, for the selected biopolymers, their corresponding spectra at 0.5-h were nearly identical to those of their aqueous dispersions, indicating the majority of CCVJ in the aqueous phase. After 24-h, OSA-starch, PG-OS and sodium caseinate yielded spectra similar to their corresponding spectra at 0.5-h (Figure 5.7A<sub>1</sub>, B<sub>1</sub> and D<sub>1</sub>), suggesting that CCVJ remained in the aqueous phase after the 24-h stabilization. Noticeably, an obvious RFE intensity enhancement at around 462 was observed in gum arabic spectrum (Figure 5.7C<sub>1</sub>) of 24-h (highlighted by the red shade). The enhancement occurring at wavelength 462 nm indicated that a small amount of CCVJ partitioned into oil phase after 24-h.

As a result, the spectra results suggested that OSA-starch, PG-OS and gum arabic delayed CCVJ water-partitioning as CCVJ delivered from the oil phase. Meanwhile, as CCVJ was delivered from the aqueous phase, only gum arabic encouraged the oil-partitioning of CCVJ. Moreover, the interaction of sodium caseinate and CCVJ in aqueous phase dominate the emission spectra regardless of the source of CCVJ.

## 5.5 Conclusion

In this study, we investigated amphiphilic biopolymer, OSA-starch, PG-OS, gum arabic and sodium caseinate effects on molecular rotor CCVJ partitioning in oil-and-water two-layer system, and demonstrated that CCVJ can be used as probe for the characterization of biopolymer. The results showed that CCVJ preferentially partitioned into water, and its partitioning and emission pattern was strongly affected by biopolymers. The spectra results showed that both OSA-starch and gum arabic hindered the transferring of CCVJ from oil to aqueous phase. The spectra of OSA-starch showed a major quantum yield at 492 nm, whereas gum arabic showed a broad band emission (from 462~492 nm) in the spectra. In contrast, the spectra of sodium caseinate resembled the spectra of its aqueous dispersion, which didn't show any reduction of oil-to-aqueous phase transfer of CCVJ.

This study described the impact of amphiphilic biopolymer on CCVJ emission pattern in a complex (oil-water) environment, and highlighted the sensitivity of molecular rotor to different

types of amphiphilic biopolymers in oil-water two-layer system. The work in the future may include detailed mechanism of CCVJ-polymer interaction, the adsorption kinetics of varying interfacial area, and further application in emulsions.

## 5.6 Reference

- Akers, W., & Haidekker, M. A. (2004). A molecular rotor as viscosity sensor in aqueous colloid dispersions. *J. Biomech. Eng.*, *126*(3), 340-345.
- Bénarouche, A., Sams, L., Bourlieu, C., Vié, V., Point, V., Cavalier, J. F., & Carrière, F. (2017). Studying gastric lipase adsorption onto phospholipid monolayers by surface tensiometry, ellipsometry, and atomic force microscopy. In *Methods in Enzymology* (Vol. 583, pp. 255-278). Academic Press.
- Berry, J. D., Neeson, M. J., Dagastine, R. R., Chan, D. Y., & Tabor, R. F. (2015). Measurement of surface and interfacial tension using pendant drop tensiometry. *Journal of colloid and interface science*, *454*, 226-237.
- Carbonaro, A., Cipelletti, L., & Truzzolillo, D. (2019). Spinning drop dynamics in miscible and immiscible environments. *Langmuir*, *35*(35), 11330-11339.
- Cayias, J. L., Schechter, R. S., & Wade, W. H. (1975). The measurement of low interfacial tension via the spinning drop technique.
- Dai, L., Yang, S., Wei, Y., Sun, C., McClements, D. J., Mao, L., & Gao, Y. (2019). Development of stable high internal phase emulsions by pickering stabilization: Utilization of zein-propylene glycol alginate-rhamnolipid complex particles as colloidal emulsifiers. *Food chemistry*, *275*, 246-254.
- Dent, M. R., López-Duarte, I., Dickson, C. J., Chairatana, P., Anderson, H. L., Gould, I. R., ... & Kuimova, M. K. (2016). Imaging plasma membrane phase behaviour in live cells using a thiophene-based molecular rotor. *Chemical Communications*, *52*(90), 13269-13272.
- Dickinson, E. (2003). Hydrocolloids at interfaces and the influence on the properties of dispersed systems. *Food hydrocolloids*, *17*(1), 25-39.

- Gharehbeiglou, P., Jafari, S. M., Hamishekar, H., Homayouni, A., & Mirzaei, H. (2019). Pectin- whey protein complexes vs. small molecule surfactants for stabilization of double nano- emulsions as novel bioactive delivery systems. *Journal of Food Engineering*, *245*, 139- 148.
- Guzman, G., Bhaway, S. M., Nugay, T., Vogt, B. D., & Cakmak, M. (2017). Transport-Limited Adsorption of Plasma Proteins on Bimodal Amphiphilic Polymer Co-Networks: Real- Time Studies by Spectroscopic Ellipsometry. *Langmuir*, *33*(11), 2900-2910.
- Haidekker, M. A., & Theodorakis, E. A. (2010). Environment-sensitive behavior of fluorescent molecular rotors. *Journal of biological engineering*, *4*(1), 11.
- Haidekker, M. A., & Theodorakis, E. A. (2016). Ratiometric mechanosensitive fluorescent dyes: design and applications. *Journal of Materials Chemistry C*, *4*(14), 2707-2718.
- Haidekker, M. A., Akers, W., Lichlyter, D., Brady, T. P., & Theodorakis, E. A. (2005a). Sensing of flow and shear stress using fluorescent molecular rotors. *Sensor Letters*, *3*(1-2), 42-48.
- Haidekker, M. A., Brady, T. P., Lichlyter, D., & Theodorakis, E. A. (2005b). Effects of solvent polarity and solvent viscosity on the fluorescent properties of molecular rotors and related probes. *Bioorganic chemistry*, *33*(6), 415-425.
- Haidekker, M. A., Ling, T., Anglo, M., Stevens, H. Y., Frangos, J. A., & Theodorakis, E. A. (2001). New fluorescent probes for the measurement of cell membrane viscosity. *Chemistry & biology*, *8*(2), 123-131.
- Hawe, A., Filipe, V., & Jiskoot, W. (2010). Fluorescent molecular rotors as dyes to characterize polysorbate-containing IgG formulations. *Pharmaceutical research*, *27*(2), 314-326.
- Jiang, Y., Zhao, C., Cheng, T., & Zhou, G. (2019). Theoretical model in cylindrical coordinates to describe dynamic interfacial tension determination with spinning drop tensiometry. *Chemical Physics*, *525*, 110409.
- Kuimova, M. K. (2012). Mapping viscosity in cells using molecular rotors. *Physical Chemistry Chemical Physics*, *14*(37), 12671-12686.
- Lai, H. P., Gao, R. C., Huang, C. L., Chen, I. C., & Tan, K. T. (2015). Fluorescence switchable probes based on a molecular rotor for selective detection of proteins and small molecules. *Chemical Communications*, *51*(90), 16197-16200.

- López-Duarte, I., Vu, T. T., Izquierdo, M. A., Bull, J. A., & Kuimova, M. K. (2014). A molecular rotor for measuring viscosity in plasma membranes of live cells. *Chemical Communications*, 50(40), 5282-5284.
- Miller, R., Aksenenko, E. V., & Fainerman, V. B. (2017). Dynamic interfacial tension of surfactant solutions. *Advances in colloid and interface science*, 247, 115-129.
- Miriani, M., Iametti, S., Bonomi, F., & Corredig, M. (2012). Structural changes of soy proteins at the oil–water interface studied by fluorescence spectroscopy. *Colloids and Surfaces B: Biointerfaces*, 93, 41-48.
- Mu, X., Liu, Y., Liu, S., Sun, Y., Lu, N., Lu, Y., ... & Li, Z. (2019). A cyanine-derived near-infrared molecular rotor for ratiometric imaging of mitochondrial viscosity in cells. *Sensors and Actuators B: Chemical*, 298, 126831.
- Mustafic, A., Huang, H. M., Theodorakis, E. A., & Haidekker, M. A. (2010). Imaging of flow patterns with fluorescent molecular rotors. *Journal of fluorescence*, 20(5), 1087-1098.
- Nazarov, A., Ney, M., & Abdulhalim, I. (2020). Parallel spectroscopic ellipsometry for ultra-fast thin film characterization. *Optics Express*, 28(7), 9288-9309.
- Pavlovich, V. S. (2006). Solvent polarity effect on excited-state lifetime of carotenoids and some dyes. *Biopolymerbiopolymers: Original Research on Biomolecules*, 82(4), 435-441.
- Scheffler, S. L., Huang, L., Bi, L., & Yao, Y. (2010). In vitro digestibility and emulsification properties of phytoglycogen octenyl succinate. *Journal of agricultural and food chemistry*, 58(8), 5140-5146.
- Shen, Y., Chang, C., Shi, M., Su, Y., Gu, L., Li, J., & Yang, Y. (2020). Interactions between lecithin and yolk granule and their influence on the emulsifying properties. *Food Hydrocolloids*, 101, 105510.
- Stauffer, C. E. (1965). The measurement of surface tension by the pendant drop technique. *The journal of physical chemistry*, 69(6), 1933-1938.
- Toliautas, S., Dodonova, J., Žvirblis, A., Čiplys, I., Polita, A., Devižis, A., ... & Vyšniauskas, A. (2019). Enhancing the Viscosity-Sensitive Range of a BODIPY Molecular Rotor by Two Orders of Magnitude. *Chemistry—A European Journal*, 25(44), 10342-10349.

- Würthner, F., Yao, S., Debaerdemaeker, T., & Wortmann, R. (2002). Dimerization of merocyanine dyes. Structural and energetic characterization of dipolar dye aggregates and implications for nonlinear optical materials. *Journal of the American Chemical Society*, *124*(32), 9431-9447.
- Yang, Z., Cao, J., He, Y., Yang, J. H., Kim, T., Peng, X., & Kim, J. S. (2014). Macro-/micro-environment-sensitive chemosensing and biological imaging. *Chemical Society Reviews*, *43*(13), 4563-4601.
- Yu, W. T., Wu, T. W., Huang, C. L., Chen, I. C., & Tan, K. T. (2016). Protein sensing in living cells by molecular rotor-based fluorescence-switchable chemical probes. *Chemical science*, *7*(1), 301-307.
- Zhu, Z., Wen, Y., Yi, J., Cao, Y., Liu, F., & McClements, D. J. (2019). Comparison of natural and synthetic surfactants at forming and stabilizing nanoemulsions: Tea saponin, Quillaja saponin, and Tween 80. *Journal of colloid and interface science*, *536*, 80-87.
- Zou, Z., Yan, Q., Ai, S., Qi, P., Yang, H., Zhang, Y., ... & Yang, R. (2019). Real-time visualizing mitophagy-specific viscosity dynamic by mitochondria-anchored molecular rotor. *Analytical chemistry*, *91*(13), 8574-8581.
- Гульнов, Д. В., Немцева, Е. В., & Кратасюк, В. А. (2016). Contrasting relationship between macro-and microviscosity of the gelatin-and starch-based suspensions and gels.

## CHAPTER 6. MOLECULAR ROTOR IN THE CHARACTERIZATION OF AMPHIPHILIC BIOPOLYMER IN EMULSIONS

### 6.1 Abstract

Molecular rotors (MRs) are a group of fluorophores of which their fluorescence intensity and emission peak wavelength ( $\lambda_{max}$ ) are affected by the local environment of MR molecules. In this study, CCVJ (9-(2-carboxy-2-cyanovinyl)-julolidine), a hydrophilic MR, was utilized as molecular probe to estimate the extent of adsorption of the selected amphiphilic polymer (starch octenylsuccinate (OSA-starch), sodium caseinate, and gum arabic) molecules at oil-water interface in emulsion. The results suggested that, all emulsions showed blue-shift (shift to lower wavelength in maximal intensity spectrum) with respect to their native polymers, indicating CCVJ was exposed to oil (hydrophobic environment) upon biopolymer interfacial adsorption. Emulsions with higher oil content showed stronger blue-shift, suggesting higher CCVJ oil exposure caused by the increased number of adsorbed biopolymers.

### 6.2 Introduction

In food, agriculture and pharmaceutical industries, amphiphilic biopolymers have been extensively explored for their emulsify properties. They facilitate the formation and stabilization of emulsion through reducing the surface tension between two immiscible phases. The emulsion properties and stability are significantly affected by the amount and interfacial behavior (e.g. diffusion/adsorption and rearrangement at the interface, etc.) of the amphiphilic biopolymer molecules adsorbed on the interface.

It is proven that fluorescence spectrophotometer/microscopy is an appropriate method that can detect and characterize *in-situ* biopolymer interfacial adsorption and behavior. Protein residues provide many intrinsic protein fluorescence probes as they are excited with UV light. Tyrosine and tryptophan residues in protein are common intrinsic fluorescence probes due to their aromatic residues that are sensitivity to the polarity of the environment (Eftink., 2002). Previous results reveal the secondary and tertiary conformational changes of myofibrillar protein (Li et al., 2020), BSA (Guo et al., 2019; Rampon et al., 2004), soy protein (Miriani et al., 2012), and ovalbumin-carboxymethyl cellulose complexes (Li et al., 2020) upon adsorption onto the oil-water interface,

through studying the fluorescence response of their tyrosine and tryptophan residues (Lakowicz, 2013; Bonomi et al., 2004). Nonetheless, intrinsic protein fluorescence technique is limited to protein-based biopolymers.

Extrinsic fluorescence probes were found to be covalently and non-covalently bound to biopolymer, and their fluorescence responses are affected by the local environment and interactions of the probes with biopolymers (Hawe et al., 2010). Extrinsic probes, including, DCVJ (Hawe et al., 2010), ANS (1-anilinonaphthalene-8-sulfonate), Bis-ANS, Nile Red (Leiske et al., 2016), and Thioflavin T (Phoon et al., 2014) were employed as sensitive and high-throughput approaches to examine the aggregation, structure change, and hydrophobicity of biopolymers (Shanmugam & Ashokkumar., 2014). However, extrinsic fluorescence probe method for the direct study of biopolymer adsorption at oil-water interface in emulsions, has not been established.

Molecular rotor (MR), an extrinsic fluorescent probe, was proposed to fulfill the simple, rapid, non-invasive, and in-situ probing of amphiphilic biopolymers upon adsorption at oil-water interface. In aqueous system, MR associates with biopolymers to probe their structure and micro-environment. In oil-water system (without any amphiphilic biopolymer), hydrophilic MR preferentially stay in the aqueous phase instead of the oil phase. As a result, in emulsion system, biopolymers that are adsorbed at oil-water interface oriented the associated hydrophilic MR molecules to the oil phase. MR shows blue-shift (shift to lower wavelength) upon exposure to more hydrophobic solvent. Therefore, the oil exposure of MR in emulsion can be interpreted from the extent of blue-shift in the emission peak, and the intensity of emission peak shift was correlated with the amount of interface adsorbed biopolymers. In addition, CCVJ can be employed as a structural probe for the differentiation of biopolymer, as the fluorescence emission intensity was sensitive to the molecular spatial restriction and molecular crowding of various biopolymer (Peng & Yao., 2020).

In this study, CCVJ (9-(2-carboxy-2-cyanovinyl)-julolidine), a hydrophilic fluorescence MR, was utilized to probe the biopolymer interfacial adsorption in oil-in-water emulsion, due to its sensitivity to both environment polarity and spatial restriction (viscosity). In this experiment, CCVJ was incorporated into emulsions prepared from model amphiphilic biopolymers, then subjected to the fluorescent measurement. OSA-starch, gum arabic, and sodium caseinate were selected as model biopolymers. The impact of biopolymer interfacial adsorption on fluorescence emission spectra was analyzed and compared. The findings of this work may support the

exploration of biopolymers in emulsion system, and their applications in emulsion-based food matrix.

## **6.3 Materials and Methods**

### **6.3.1 Materials**

Octenylsuccinate starch (OSA-starch) was purchased from Ingredion (Chicago, IL). Gum Arabic was obtained from TIC gum (White Marsh, MD). Sodium caseinate was kindly provided by company from industry. CCVJ (9-(2-Carboxy-2-cyanovinyl) julolidine, C<sub>16</sub>H<sub>16</sub>N<sub>2</sub>O<sub>2</sub>),  $\geq$  97.0% (HPLC), was purchased from Sigma-Aldrich. Vegetable oil was purchased from local grocery store. Double-distilled water was used. All chemicals used were of reagent grade.

### **6.3.2 Preparation of CCVJ Stock Solution**

Precisely weighed 5.0 mg CCVJ (Sigma-Aldrich, USA) powder was dissolved in 0.5 mL of DMSO (HPLC grade, Fisher Chemical, US) to reach concentration of 10 mg/mL. The resulting DMSO solution (0.1 mL) was further diluted with 7.46 mL phosphate buffer (PBS, 5 mM, pH 7.0) and oil to obtain the CCVJ aqueous and oil (5.0  $\mu$ M) controls, respectively. The obtained stock solutions were stored in dark at room temperature until use.

### **6.3.3 Preparation of PBS solution of CCVJ and Oil solution of CCVJ**

To prepare aqueous and oil controls, 10  $\mu$ L CCVJ aqueous or oil stock solution was mixed with 990  $\mu$ L PBS and oil, respectively, yielding working solutions containing 5.0  $\mu$ M CCVJ in PBS or oil. The obtained mixtures were wrapped with aluminum foil and equilibrated in a shaking water bath overnight at room temperature. Thereafter, a 100  $\mu$ L aliquot of each control was transferred into 96-well microplates for fluorescence measurements. Each control was prepared and measured in triplicate.

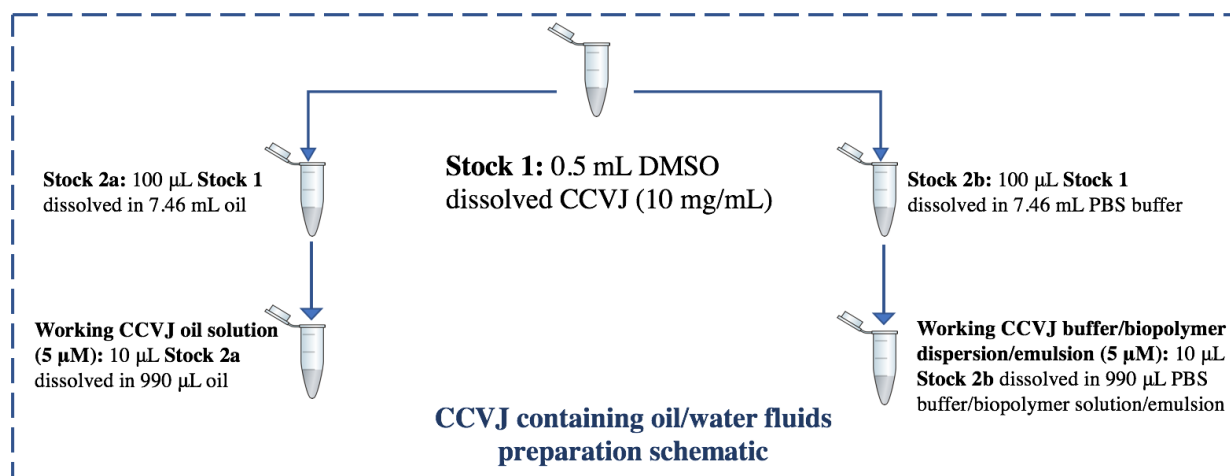


Figure 6.1 Schematic diagram showing the preparation of CCVJ containing aqueous and oil controls, biopolymer working dispersions, and emulsions.

### 6.3.4 Preparation of Biopolymer Dispersions and Emulsions dosed with CCVJ

Precisely weighed amount of OSA-starch, gum arabic, and sodium caseinate was added in phosphate-buffered saline (PBS) (5 mM, pH 7) to form dispersions with concentrations ranging from 1.25 to 100 mg/mL (1.25, 2.5, 3.75, 5, 10, 20, 50, and 100 mg/mL). Pure PBS (5mM, pH 7) served as blank control. In each 1-mL centrifuge tube, 10 µL CCVJ stocking solution was mixed with 990 µL biopolymer dispersion (5 µM CCVJ). All CCVJ containing biopolymer dispersions were wrapped with aluminum foil and stabilized in water shaking bath (70 rpm) for 2 hours at room temperature in dark. Pure PBS buffer (5mM, pH 7) was used as blank. Thereafter, 100 µL-aliquots of dispersion, and PBS blank were transferred into 96-well microplates (Greiner Bio-one, Germany) fluorescence measurements. Each experiment was performed in triplicate.

To examine the CCVJ emission response in emulsion system, oil-in-water emulsion was prepared using the selected biopolymers. Firstly, the polymer dispersion was prepared by dissolving solids of OSA-starch, gum arabic, and sodium caseinate in phosphate buffer (5 mM, pH 7.0) to reach a concentration of 10, 10 and 5 mg/mL, respectively. To the dispersions, vegetable oil was added at ratios of oil-to-biopolymer 1:2 and 1:1. Preliminary mixing was conducted with constant stirring (600 rpm for 1 hour) to form coarse emulsions. The mixtures were further treated with high-speed homogenizer (10,000 rpm for 1 min, T25ULTRA-TURRAX, IKA), followed with high-pressure homogenization (17.2-24.1 MPa, two cycles, Nano DeBee, BEE International).

In each 1-mL centrifuge tube, 10  $\mu\text{L}$  CCVJ stocking solution was mixed with 990  $\mu\text{L}$  emulsion to reach a CCVJ concentration of 5  $\mu\text{M}$ . The emulsions were wrapped with aluminum foil to avoid light degradation. Pure PBS buffer (5mM, pH 7) served as blank. Thereafter, 100  $\mu\text{L}$ -aliquots of polymer dispersion, and PBS blank were transferred into 96-well microplates (Greiner Bio-one, Germany) in triplicate for fluorescence measurements. Pure polymer dispersions (in PBS), and high-speed and high-pressure homogenization processed polymer dispersions were included as references.

### **6.3.5 Emulsion Particle Size Measurement**

The emulsions were diluted to 0.1% (w/v) using 0.01 M NaAc buffer pH 6.0. Thereafter, the particle size was determined at room temperature using a Zetasizer Nano (ZS90, Malvern Instruments).

### **6.3.6 Fluorescence Spectra Scan**

Fluorescent emission spectra and fluorescence intensity of CCVJ in biopolymer aqueous dispersions and their respective emulsions were scanned and measured using a Synergy H1 Hybrid Multi-Mode Reader from BioTek instrument in the top-read mode (read height was set at 7 mm). For each type of fluid, triplicate wells were prepared and measured. The excitation wavelength was set at 420 nm, and the emission wavelengths were scanned from 450 nm to 650 nm with the spectra bandwidth of 2 nm. The temperature was set at 25°C.

### **6.3.7 Statistical Analysis**

Each measurement was performed in triplicate. Results were expressed as mean  $\pm$  standard deviation (SD). One-way ANOVA was performed for significant difference analysis. P-value  $\leq 0.05$  was used to identify significant differences between results using SPSS for Windows (version rel. 10.0.5, 1999, SPSS Inc., Chicago, IL, USA).

## 6.4 Results and Discussions

### 6.4.1 Emulsion Particle Size

Table 6.1 compared the average particle size (*Z-Ave*) of emulsions formed using OSA-starch, gum arabic and sodium caseinate, at oil-to-biopolymer ratios of 1:2 and 1:1. In general, for each biopolymer, the average particle size increased as oil-to-biopolymer ratio increased. For example, as the oil-to-biopolymer ratio increased from 1:2 to 1:1, emulsion particle size for sodium caseinate increased by 21 nm, from 391 nm to 412 nm, gum arabic increased by 74 nm, from 540 nm to 614 nm, and OSA-starch increased by 26 nm, from 366 nm to 392 nm.

Table 6.1 Droplet size of OSA-starch (10 mg/mL, 1% w/v), gum Arabic (10 mg/mL, 1% w/v) and sodium caseinate (5 mg/mL, 0.5% w/v) emulsions with different oil concentrations.

Emulsion	Emulsion droplet size <i>Z-Ave</i> (d. nm) <sup>ab</sup>	PDI <sup>a</sup>
Sodium caseinate (biopolymer/oil 2:1)	391.24±3.91a	0.24±0.07
Sodium caseinate (biopolymer/oil 1:1)	412.43±2.37 b	0.22±0.09
Gum arabic (biopolymer/oil 2:1)	540.50±4.15 a	0.26±0.09
Gum arabic (biopolymer/oil 1:1)	614.63±7.75 b	0.11±0.09
OSA-starch (biopolymer/oil 2:1)	366.87±6.00 a	0.11±0.03
OSA-starch (biopolymer/oil 1:1)	392.13±8.25 b	0.13±0.1

<sup>a</sup>Data expressed as mean±SD (n = 3).

<sup>b</sup> Significant differences within OSA-starch, sodium caseinate, or gum arabic emulsion group are denoted by different letters (p<0.05).

At higher oil concentration, the interfacial area created by mechanical energy input during emulsification process was too large to be completely covered by the amphiphilic biopolymer, and consequently, the emulsion droplets were larger. Therefore, we considered that the emulsion with higher oil content (oil-to-biopolymer ratio of 1:1) produced larger interfacial area for biopolymer to absorb compared to lower oil content (oil-to-biopolymer ratio of 1:2). Prior work showed similar trends and suggested that at low oil and emulsifier content (≤5% w/w), the emulsion droplet specific surface area increased as oil concentration increased (Dapčević Hadnađev et al., 2013).

## 6.4.2 CCVJ fluorescence emission in oil and PBS buffer

To study the fluorescence spectra of CCVJ in emulsion, single-phase system that contained CCVJ in oil, and PBS was characterized first. Figure 6.2 showed the emission spectra of CCVJ in oil and PBS buffer. In general, the CCVJ fluorescence emission peak was more blue-shifted with higher intensity in oil than in PBS.

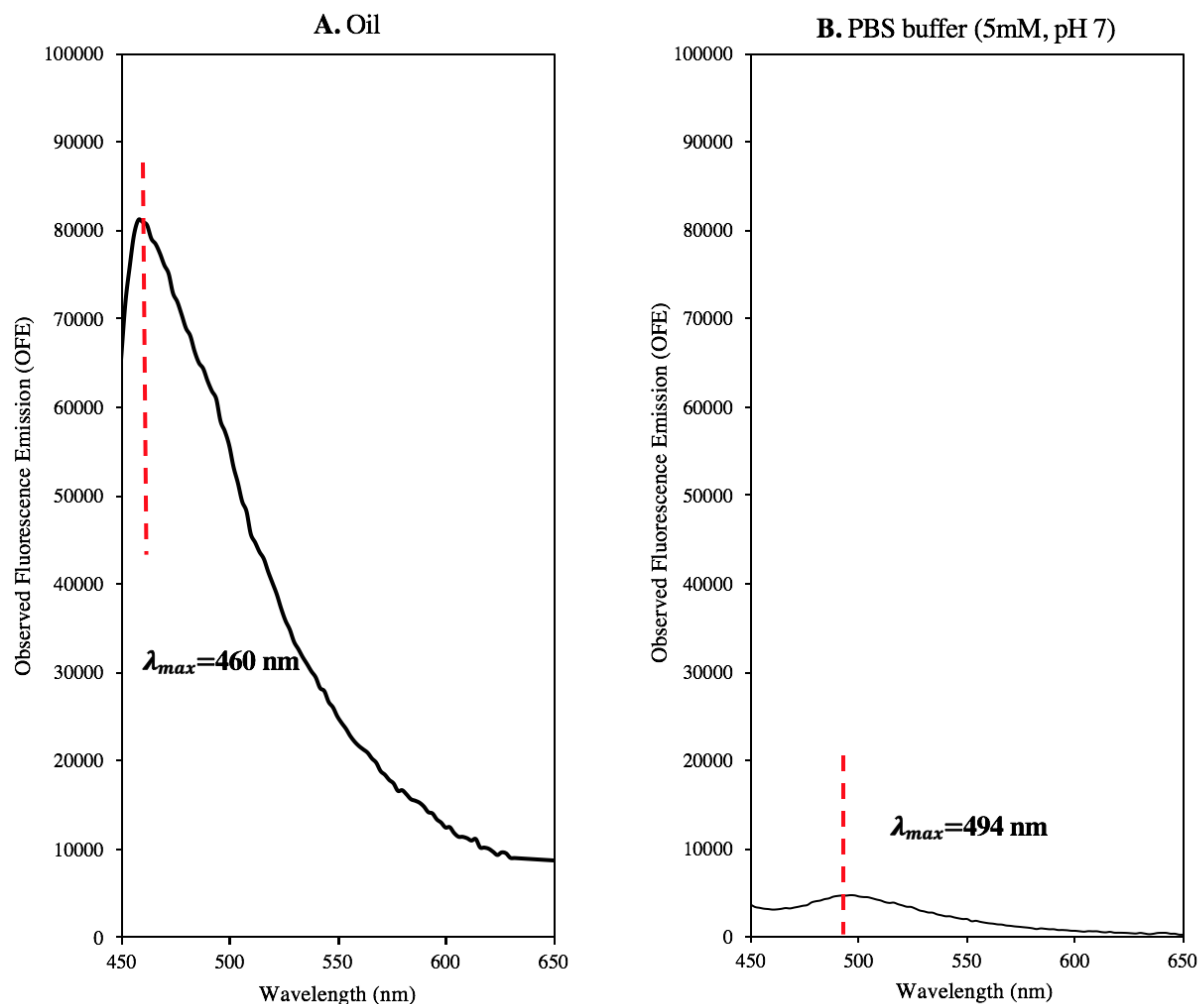


Figure 6.2 The observed fluorescence emission spectra of CCVJ at concentrations of 5  $\mu\text{M}$  in oil (A) and PBS (B) are shown. Each well of 96 plate contained 100  $\mu\text{L}$  of oil or PBS.

In oil, the emission intensity of CCVJ was  $\sim 80000$  OFE, which was 17 times higher than that in PBS ( $\sim 4500$  OFE). In addition, the peak maximum ( $\lambda_{max}$ ) of CCVJ emission located at 460 nm in oil and 494 nm in PBS, respectively.

The viscous nature of oil delayed the relaxation of twisted intermolecular charge transfer, leading to high fluorescence intensity. In contrast, the low fluorescence emission in PBS was due to the strong fluorescence quenching by water molecules. In more polar solvent like water, there is a quenching effect, that played an important role in the stabilization of TICT states, retarded the fluorescence emission from the excited state, and thus enhanced the non-fluorescence relaxation from the TICT states (Haidekker & Theodorakis, 2010).

The blue-shift in oil was induced through changes in solvent polarity or hydrogen bonding. As indicated by Haidekker et al. (2005), after photo-excitation of CCVJ molecule, a dipole moment between the ground and excited state is generated. The energy expended for polar solvent molecules to align with the dipole moment of CCVJ leads to the red-shift of fluorescence emission (Pavlovich, 2016; Haidekker et al., 2005).

The large difference in emission intensity and the difference of peak location between oil and aqueous system allowed for high-sensitivity detection of the local polarity of the biopolymer.

Preliminary experiment showed that CCVJ preferentially stayed in the aqueous phase rather than the oil phase due to its hydrophilicity. In emulsion, the adsorption of biopolymer onto the oil-water interface would increase the exposure of CCVJ molecules to the oil phase, which is reflected by the increased CCVJ fluorescence signal and blue-shift.

### **6.4.3 CCVJ fluorescence spectra of biopolymer aqueous dispersions**

The fluorescent emission spectra of CCVJ in OSA-starch, gum arabic, and sodium caseinate dispersions were shown in Figure 6.3. In general, biopolymer concentration and biopolymer type had appreciable impacts on both fluorescence emission intensity and the peak maximum.

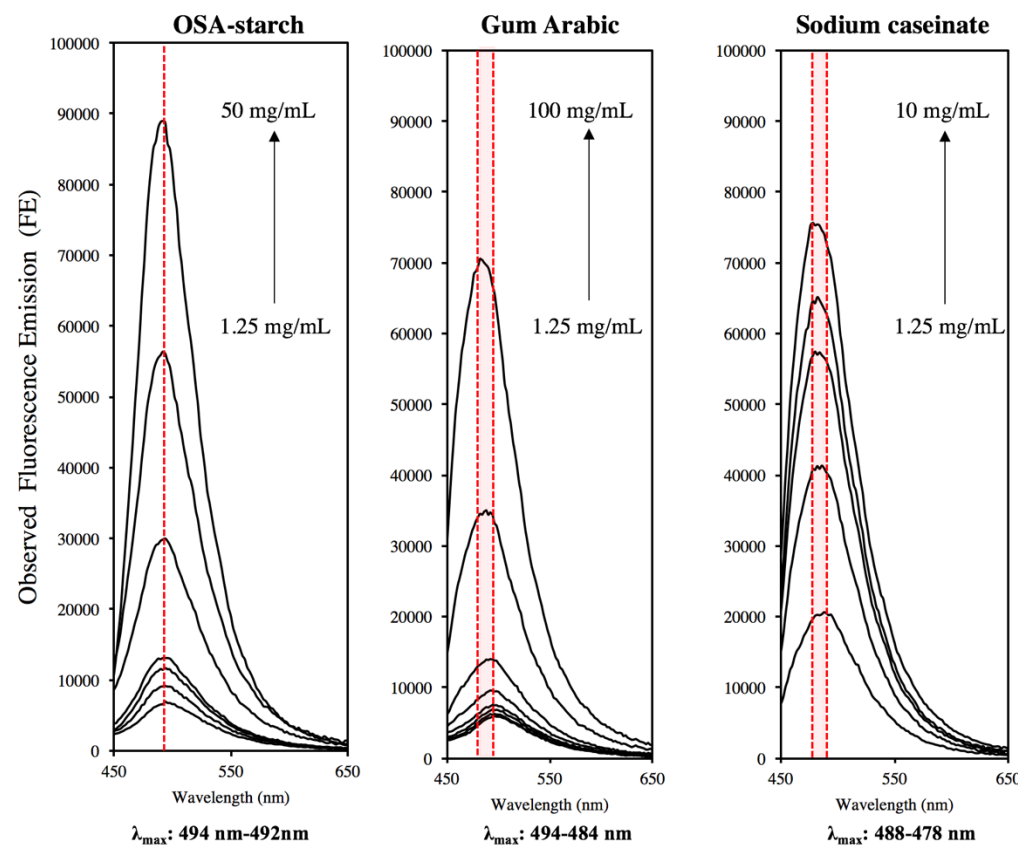


Figure 6.3 The observed fluorescence emission spectra of CCVJ in OSA-starch, gum arabic, and sodium caseinate aqueous dispersions. For each biopolymer, only emission spectra within detectable emission intensity range are displayed in the figure. In each group, from bottom to top, the concentrations of biopolymer were: (1) 1.25, 2.5, 3.75, 5, 10, 20, and 50 mg/mL for OSA-starch, (2) 1.25, 2.5, 3.75, 5, 10, 20, 50, and 100 mg/mL for gum arabic, and (3) 1.25, 2.5, 3.75, 5, and 10 mg/mL for sodium caseinate. Arrow indicates the direction of increasing concentration of biopolymer. The red shaded area/line indicates the change of the peak maximum ( $\lambda_{max}$ ), with its value provided at the bottom of graph for each biopolymer.

Firstly, the impact of biopolymer type and concentration on CCVJ fluorescence intensity was examined and the results were shown in Figure 6.4. A strong dependency of peak emission intensity on the biopolymer concentration can be observed in both Figure 6.3 and 6.4. As the concentration of biopolymer increased, their fluorescence emission intensity increased progressively.

In addition, the increase rate of emission intensity was affected by the type of biopolymer dispersion. For example, for every 1 mg/mL increase in concentration, nearly up to ~ 8000, ~ 1900, and 700 OFE increase in emission intensity was observed in sodium caseinate, OSA-starch, and

gum arabic, respectively. CCVJ exhibited the highest increase rate of emission intensity for sodium caseinate, and the lowest for gum arabic. The results indicated that the sodium caseinate dispersion yield the highest level of spatial restriction for CCVJ, followed with OSA-starch, and gum arabic dispersions (Peng & Yao, 2020).

In addition, the embedded graph in Figure 6.4 showed that the emission intensity increased linearly with the increasing biopolymer concentration in the diluted dispersion (1.25 ~ 5 mg/mL). The trend-line slopes of biopolymers were in the order of, sodium caseinate (slop= $1.37 \times 10^7$ ,  $R^2=0.99$ ) > OSA-starch (slop= $1.66 \times 10^6$ ,  $R^2=0.99$ ) > gum arabic (slop= $4.58 \times 10^5$ ,  $R^2=0.96$ ). The difference among slopes highlighted the sensitivity of CCVJ as a structural probe for biopolymer differentiation at very low concentration

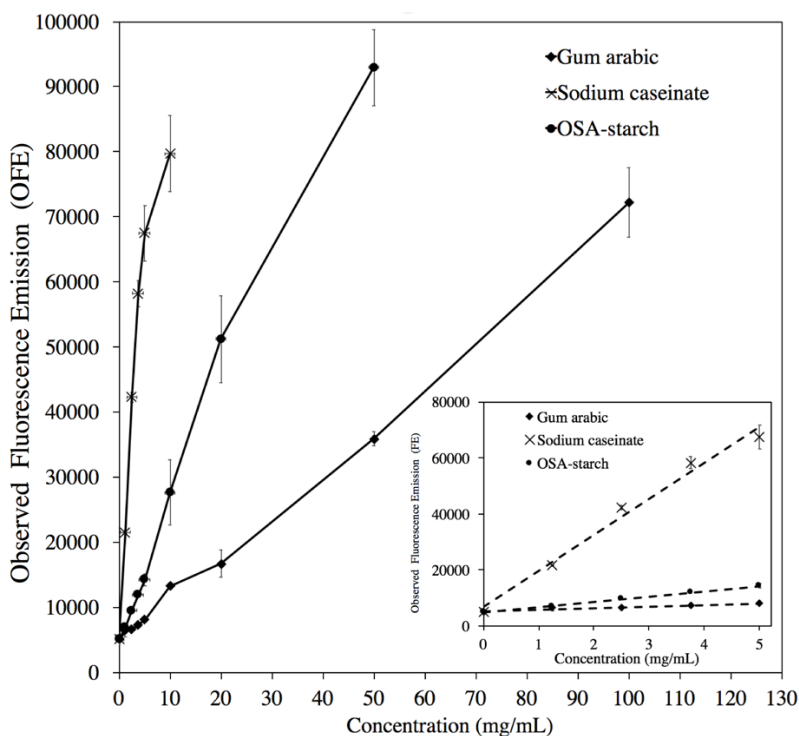


Figure 6.4 The observed emission intensity (OFEs were obtained at  $\lambda_{max}$  of each biopolymer) as a function of biopolymer concentration (mg/mL) in aqueous dispersion. For each biopolymer, the concentrations of ranges were: (1) 1.25~ 50 mg/mL for OSA-starch; (2) 1.25~ 100 mg/mL for gum arabic, and (3) 1.25~ 10 mg/mL for sodium caseinate. The embedded figure displayed the observed fluorescence emission intensity (OFE were obtained at  $\lambda_{max}=494$  nm for OSA-starch, and gum arabic dispersions, and  $\lambda_{max}=488$  nm for sodium caseinate dispersions) at biopolymer concentration of 0~5.0 mg/mL, and the fitted curves were shown in dotted lines.

The impact of biopolymer concentration and biopolymer type on the blue-shift of peak maximum ( $\lambda_{max}$ ) was examined, and the results were displayed in Figure 6.5. In general, all biopolymers exhibited blue-shift compared to PBS buffer, and the blue-shift increased as concentration increased. For example, the spectra of OSA-starch, gum arabic, and sodium caseinate dispersions at 2.5 mg/mL exhibited peaks at 494, 494, and 486 nm, respectively. For more concentrated dispersions (10 mg/mL), the emission spectra of OSA-starch and PG-OS were blue-shifted to 492, 492, and 478 nm, respectively. The changes in blue-shift indicated that more concentrated biopolymer provided more non-polar domains for CCVJ.

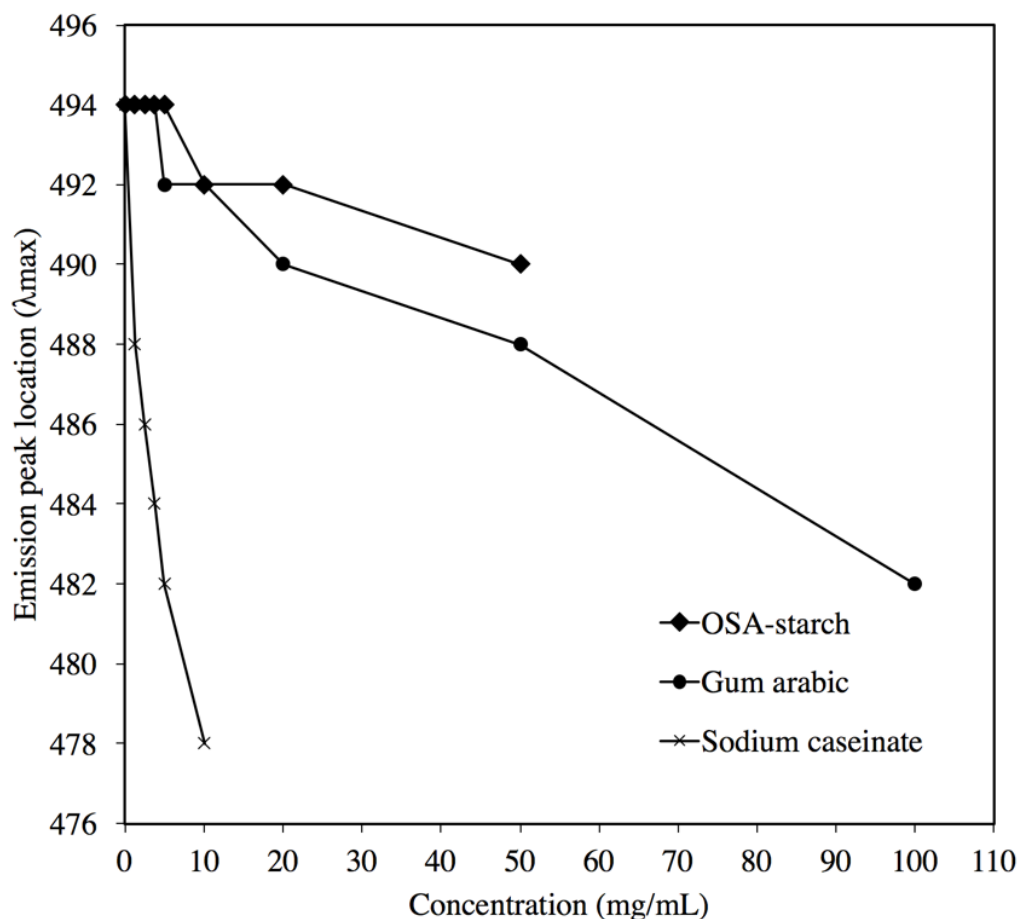


Figure 6.5 Wavelength of emission peak location ( $\lambda_{max}$ ) as a function of biopolymer concentration (mg/mL) in aqueous dispersion. For each biopolymer dispersion, the concentrations of ranges were: (1) 1.25~ 50 mg/mL for OSA-starch; (2) 1.25~ 100 mg/mL for gum arabic, and (3) 1.25~ 10 mg/mL for sodium caseinate.

In Figure 6.5, we further found that the rate of blue-shift for all biopolymers was in the order of OSA-starch < gum arabic < sodium caseinate. For example, at concentration of 5 mg/mL,  $\lambda_{max}$  was 482 nm for sodium caseinate, 492 nm for gum arabic, and 494 nm for OSA-starch. The order indicated that sodium caseinate brought the largest amount of non-polar domain for CCVJ, which were mostly contributed by protein ‘nano-pockets’ and aggregates. In contrast, the glucan chains in OSA-starch were only able to provide slightly hydrophobic nano-pockets, thus produced the least blue-shift. The peak shift in gum arabic dispersions indicated that CCVJ might be associated with the glycoprotein region which produced non-polar domain for CCVJ to reside. Due to the low percentage of protein component (2-3% protein in gum arabic), the amount of the non-polar region in gum arabic was possibly less than sodium caseinate (Akers & Haidekker, 2004; Hawe, et al., 2010).

The spectra of biopolymer dispersions provided the reference for the emulsion analysis. In addition, the CCVJ fluorescence response of biopolymer dispersions provided information about the structure features, *e.g.* the accessible hydrophobic areas in biopolymer (protein/glucan chain formed nano-pockets, etc.), molecule aggregation, and spatial restriction, can be obtained from the analysis of emission intensity and peak maximum.

#### **6.4.4 CCVJ fluorescence spectra of biopolymer emulsions**

The CCVJ fluorescence emission spectra (excitation wavelength = 420 nm, emission wavelengths = 450 ~ 650 nm) of oil-to-polymer 1:2, and 1:1 emulsions of gum arabic (10 mg/mL), OSA-starch (10 mg/mL), and sodium caseinate (5.0 mg/mL) recorded were shown in Figure 6.6. No significant change in emission fluorescence spectra was observed between high-pressure homogenized (HPH) aqueous polymer dispersions and un-processed aqueous polymer dispersion.

As shown in Figure 6.6, the  $\lambda_{max}$  of all emulsion spectra showed blue-shifts compared with their respective biopolymer aqueous dispersions, and the blue-shift was found to be affected by oil-to-polymer ratios and polymer type.

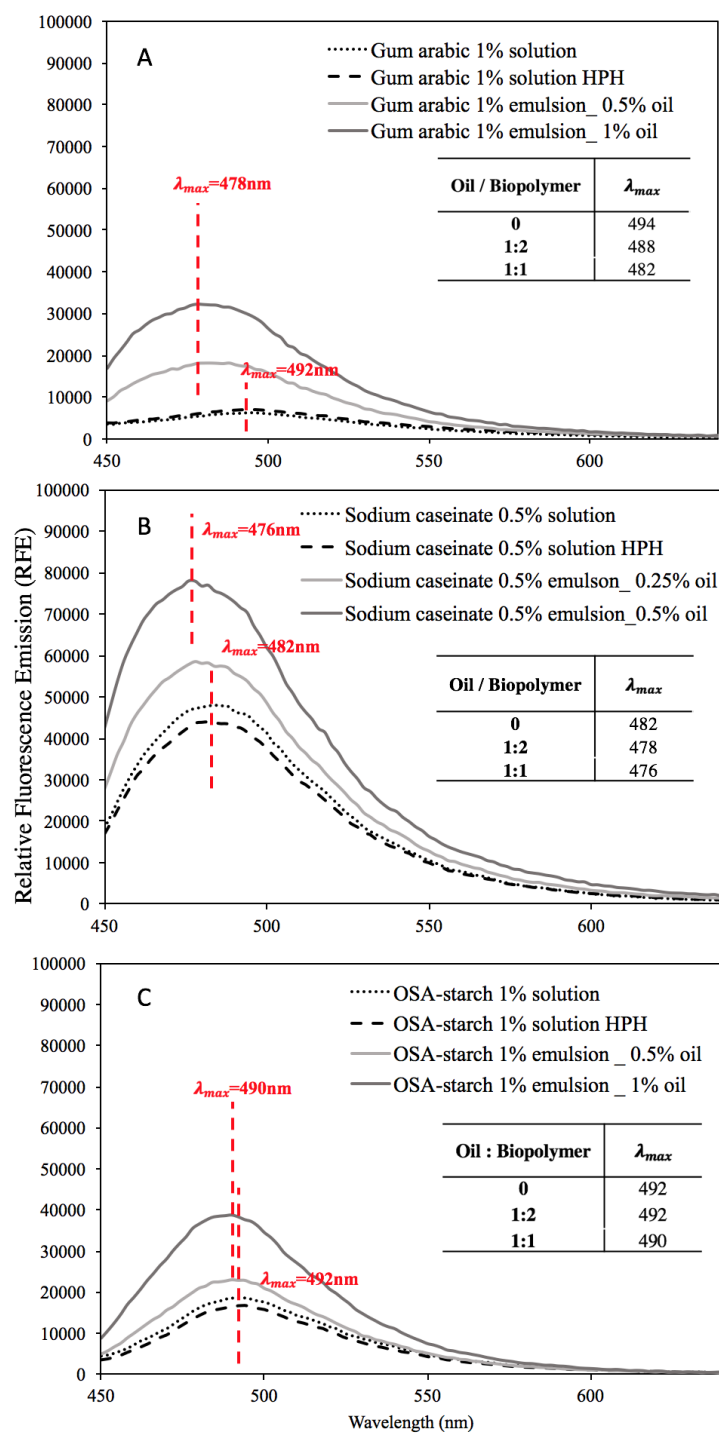


Figure 6.6 Fluorescence emission spectra of: A. gum arabic, B. sodium caseinate, and C. OSA-starch aqueous dispersions and their corresponding emulsions at oil-to-polymer ratios of 1:2, and 1:1. Emission spectra were shown in solid lines, polymer aqueous dispersion (dotted lines), and high pressure homogenization (HPH) processed polymer aqueous dispersion (dashed lines).  $\lambda_{max}$  of polymers dispersions and their corresponding emulsions were highlighted in red dashed lines. Spectra are measured in triplicates. The impact of oil-to-polymer ratio on the fluorescence emission peak ( $\lambda_{max}$ ) of emulsion were shown in the embedded table in each graph.

Firstly, the impact of oil-to-polymer ratios on the blue-shift was examined and the results were displayed in Figure 6.6. In aqueous dispersions, gum arabic (1%), sodium caseinate (0.5%), and OSA-starch (1%) showed peaks at 492 nm, 482 nm, and 492 nm, respectively. In emulsion of oil-to-polymer ratio at 1:2,  $\lambda_{max}$  of gum arabic (1%), sodium caseinate (0.5%), and OSA-starch (1%) emulsions were blue-shifted to 488, 478, and 492 nm, respectively. The  $\lambda_{max}$  of peaks were further blue-shifted to 482, 476, and 490 nm, respectively, as the oil concentration increased to oil-to-polymer ratio of 1:1.

Prior research already demonstrated that in oil-water system, majority of CCVJ molecules partitioned into the aqueous phase. In addition, as a hydrophilic molecule, CCVJ tend to associate with the biopolymer molecules that are dissolved in the aqueous phase. Due to the interplay of multiple solvent (oil and PBS) and biopolymer oil-water interface adsorption in emulsion system, CCVJ molecules were localized at several different sites. Therefore, in emulsion system, CCVJ molecules either preferentially associated with the un-adsorbed biopolymer in the bulk aqueous phase, or located at the oil-water interfacial layer due to the interaction with the interface adsorbed biopolymer. As a result, the adsorption of biopolymer displaced some CCVJ molecules to a more hydrophobic location, leading to blue-shift of  $\lambda_{max}$ .

The proposed mechanism for the impact of oil concentrations on blue-shifts was shown in Figure 6.7. At low oil concentration, the mechanical processing didn't generate enough interfacial area for all the biopolymer to adsorb, therefore, the biopolymer was present in excess amount (Figure 6.7B). Higher oil content provided larger interfacial surface area, and increased the total amount of interfacial adsorbed biopolymer as the newly created interface was immediately covered by the available biopolymer in the bulk aqueous phase (Figure 6.7C). The increased amount of adsorbed biopolymer would bring more CCVJ to the oil-water interface, leading to a stronger blue-shift. Consequently, the progressive blue-shift of  $\lambda_{max}$  along with increasing oil concentration in the emulsion can be related to the increased interface-adsorbed biopolymer/total biopolymer ratio (AP%). As a result, the blue-shift of  $\lambda_{max}$  in emulsion can be utilized to qualitatively analyze the interfacial adsorption of biopolymer in emulsion system.

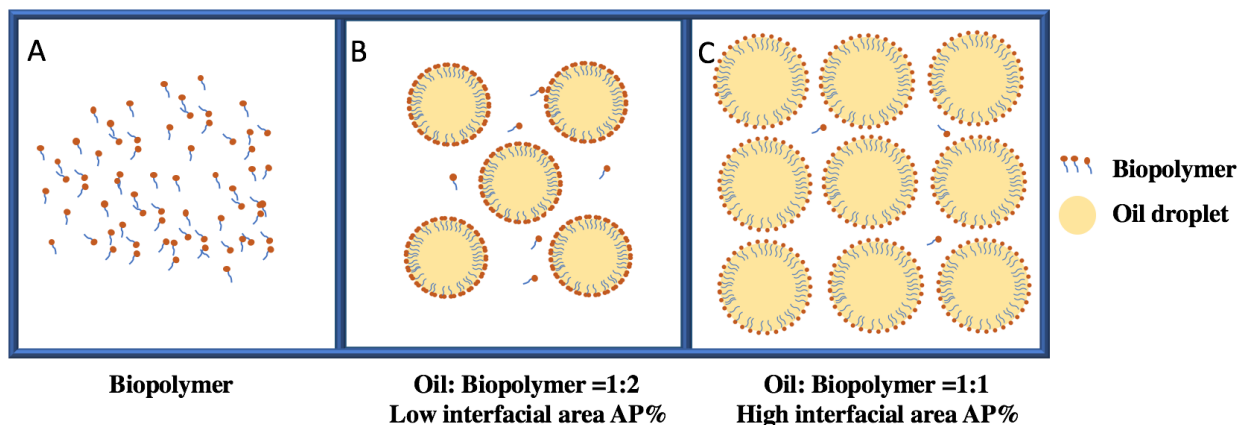


Figure 6.7 The impact of oil concentration on oil-water interface-adsorbed biopolymer/total biopolymer ratio (AP%) in emulsions. Biopolymer adsorption percentage (AP%) was calculated as:  $AP (\%) = \frac{\text{interface adsorbed biopolymer}}{\text{total biopolymer}}$ . Blue tail represented the hydrophobic region and the dark red circle represented the hydrophilic region of the biopolymer.

In addition, the impact of biopolymer type on the blue-shift was investigated and the results were shown in Figure 6.6. For example, the aqueous dispersion of OSA-starch (10 mg/mL) showed  $\lambda_{max}$  at 492 nm, the  $\lambda_{max}$  shifted to 492, and 490 nm for emulsion of oil-to-polymer ratio at 1:2 and 1:1, respectively (Figure 6.6C). In gum arabic, the  $\lambda_{max}$  of its aqueous dispersion was 492 nm. The  $\lambda_{max}$  shifted to 488, and 482 nm for emulsion of oil-to-polymer ratio at 1:2 and 1:1, respectively (Figure 6.6A). The strong blue-shift from 492 nm to 482 nm observed in gum arabic dispersion and emulsion may be resulted from the association between CCVJ and the glycoprotein fraction in gum arabic. When gum arabic adsorbed onto oil-water interface, the glycoprotein residue moved into the oil phase, thereby, increased the hydrophobicity of the local environment of the glycoprotein associated CCVJ (Padala et al., 2009). The increased hydrophobicity of CCVJ environment subsequently led to a significant blue-shift. In contrast, a minimal blue-shift observed in OSA-starch dispersion and emulsions. The lipophilic octenylsuccinate group in OSA-starch was responsible for oil-water interface adsorption. However, the octenylsuccinate chains failed to incorporate the CCVJ into oil layer as the negatively charged COO<sup>-</sup> group in octenylsuccinate repelled the anion form of CCVJ (Rumble et al., 2012; Dokić et al., 2008). Therefore, CCVJ molecules maintained significant contact with the glucan chains in the aqueous phase instead of oil, resulting in an insufficient increase in the hydrophobicity of CCVJ local environment.

Table 6.2 Normalized fluorescence intensity measured at  $\lambda_{max}$  of OSA-starch (1% w/v), gum arabic (1% w/v) and sodium caseinate (0.5% w/v) emulsions.<sup>a</sup>

	Sodium caseinate 0.5% (w/v) <sup>b</sup>	OSA-starch 1% (w/v) <sup>b</sup>	Gum arabic 1% (w/v) <sup>b</sup>
	52978.66 ±4495.64		
<b>Aqueous dispersion</b>	a	20657.66±602.05 a	6841.33±333.96 a
<b>Aqueous dispersion processed by HPH</b>		19605.66±1576.23	
	47200±1304.42 a	a	7555.66±188.02 a
	62677.66±1381.86		18791.33±1255.35
<b>Emulsion oil-to-polymer ratio at 1:2</b>	b	25032.66±341.83 b	b
	79663.33±4566.73	45395.33±2929.63	32726.66±1907.36
<b>Emulsion oil-to-polymer ratio at 1:1</b>	c	c	c

<sup>a</sup> Data expressed as mean±SD (n = 3).

<sup>b</sup> Significant differences within OSA-starch, sodium caseinate, or gum arabic containing group are denoted by different letters (p<0.05).

Simultaneously to  $\lambda_{max}$  displacement, the fluorescence intensity increased in emulsion compared with its respective aqueous dispersion, and the results were summarized in Table 6.2. Our finding showed that the fluorescence intensity was significantly higher in emulsions than in aqueous solution, and the intensity increased as oil concentration increased.

As a turbid medium, the light scattering effects of the emulsion droplets, *e.g.* ‘inner filter’ effects (Castelain & Genot., 1996; Rampon et al., 2004; Stelmaszewski, 2011; Jerlov, 1976) was the major reason for the increased quantum yield of emulsions. The incident and emitted lights were scattered by the large spherical emulsion droplets, which changes the intensity of the radiation reaching the fluorescence detector. Nevertheless, the correlation between the emission intensity and oil concentration or emulsion droplets cannot be established, since many factors contributed to the quantum yield of the emulsion. For example, the hydrophobic residues associated CCVJ in biopolymer at interface were in direct contact with oil, leading to an increase in the environment hydrophobicity and quantum yield of the biopolymer; the aggregation of biopolymer at interface produced more spatial restricted cavities for CCVJ that induced an increase in quantum yield. However, these potential fluorescence contributions cannot be extracted from the fluorescence emission spectrum for separate analysis.

## 6.5 Conclusion

In this study, we demonstrated that molecular rotor---CCVJ fluorescence measurements for non-disruptive monitoring of biopolymer in oil-in-water emulsion. This method was sensitive to the structure and local environment of the biopolymer molecules in the system, thus manifesting their adsorption-desorption at oil-water interface. The result suggested that the adsorption of biopolymer on the oil-water interface of emulsion led to a blue-shift in the fluorescence emission spectra with respect to their aqueous dispersions, indicating the exposure of CCVJ to the oil phase. The extent of blue-shift was affected by oil concentration. As oil concentration increased (from oil-to-biopolymer ratio of 1:2 to 1:1), the interface area intended to increase, which allowed higher amount of biopolymer to be adsorbed at interfacial layer, leading to a stronger blue-shift. This study facilitated a better understanding of biopolymer at oil-water interface, and the application of molecular rotor to emulsion-based food matrix. Key advantage of the molecular rotor is that it is a non-disruptive approach that can be used to study concentrated emulsions *in-situ*.

## 6.6 Reference

- Akers, W., & Haidekker, M. A. (2004). A molecular rotor as viscosity sensor in aqueous colloid solutions. *J. Biomech. Eng.*, 126(3), 340-345.
- Bonomi, F., Mora, G., Pagani, M. A., & Iametti, S. (2004). Probing structural features of water-insoluble proteins by front-face fluorescence. *Analytical Biochemistry*, 329(1), 104-111.
- Castelain, C., & Genot, C. (1996). Partition of adsorbed and nonadsorbed bovine serum albumin in dodecane-in-water emulsions calculated from front-face intrinsic fluorescence measurements. *Journal of agricultural and food chemistry*, 44(7), 1635-1640.
- Dapčević Hadnađev, T., Dokić, P., Krstonošić, V., & Hadnađev, M. (2013). Influence of oil phase concentration on droplet size distribution and stability of oil-in-water emulsions. *European journal of lipid science and technology*, 115(3), 313-321.
- Dokić, P., Dokić, L., Dapčević, T., & Krstonošić, V. (2008). Colloid characteristics and emulsifying properties of OSA starches. In *Colloids for nano-and biotechnology* (pp. 48-56). Springer, Berlin, Heidelberg.
- Eftink, M. R. (2002). Intrinsic fluorescence of proteins. In *Topics in fluorescence spectroscopy* (pp. 1-15). Springer, Boston, MA.

- Guo, Y., Huang, W. C., Wu, Y., Qi, X., & Mao, X. (2019). Conformational changes of proteins and oil molecules in fish oil/water interfaces of fish oil-in-water emulsions stabilized by bovine serum albumin. *Food chemistry*, 274, 402-406.
- Haidekker, M. A., & Theodorakis, E. A. (2010). Environment-sensitive behavior of fluorescent molecular rotors. *Journal of biological engineering*, 4(1), 11.
- Haidekker, M. A., Akers, W., Lichlyter, D., Brady, T. P., & Theodorakis, E. A. (2005a). Sensing of flow and shear stress using fluorescent molecular rotors. *Sensor Letters*, 3(1-2), 42-48.
- Hawe, A., Filipe, V., & Jiskoot, W. (2010). Fluorescent molecular rotors as dyes to characterize polysorbate-containing IgG formulations. *Pharmaceutical research*, 27(2), 314-326.
- Jerlov, N. G. (1976). *Marine optics*. Elsevier. pp. 231.
- Lakowicz, J. R. (Ed.). (2013). *Principles of fluorescence spectroscopy*. Springer Science & Business Media.
- Leiske, D. L., Shieh, I. C., & Tse, M. L. (2016). A method to measure protein unfolding at an air-liquid interface. *Langmuir*, 32(39), 9930-9937.
- Li, K., Fu, L., Zhao, Y. Y., Xue, S. W., Wang, P., Xu, X. L., & Bai, Y. H. (2020). Use of high-intensity ultrasound to improve emulsifying properties of chicken myofibrillar protein and enhance the rheological properties and stability of the emulsion. *Food Hydrocolloids*, 98, 105275.
- Miriani, M., Iametti, S., Bonomi, F., & Corredig, M. (2012). Structural changes of soy proteins at the oil-water interface studied by fluorescence spectroscopy. *Colloids and Surfaces B: Biointerfaces*, 93, 41-48.
- Padala, S. R., Williams, P. A., & Phillips, G. O. (2009). Adsorption of gum Arabic, egg white protein, and their mixtures at the oil-water interface in limonene oil-in-water emulsions. *Journal of agricultural and food chemistry*, 57(11), 4964-4973.
- Pavlovich, V. S. (2006). Solvent polarity effect on excited-state lifetime of carotenoids and some dyes. *Biopolymerbiopolymers: Original Research on Biomolecules*, 82(4), 435-441.
- Peng, X., & Yao, Y. (2020). Molecular rotor as a structural probe of glucan polymers: Amylopectin, phytoglycogen, and their  $\beta$ -limit dextrins as models. *Carbohydrate Polymers*, 250, 116859.

- Rampon, V., Brossard, C., Mouhous-Riou, N., Bousseau, B., Llamas, G., & Genot, C. (2004). The nature of the apolar phase influences the structure of the protein emulsifier in oil-in-water emulsions stabilized by bovine serum albumin.: a front-surface fluorescence study. *Advances in colloid and interface science*, 108, 87-94.
- Rumble, C., Rich, K., He, G., & Maroncelli, M. (2012). CCVJ is not a simple rotor probe. *The Journal of Physical Chemistry A*, 116(44), 10786-10792.
- Shanmugam, A., & Ashokkumar, M. (2014). Ultrasonic preparation of stable flax seed oil emulsions in dairy systems–physicochemical characterization. *Food Hydrocolloids*, 39, 151-162.
- Stelmaszewski, A. (2011). The contribution of fluorescence to measurements of light scattering in oil-in-water emulsions. *Oceanologia*, 53(2), 549-564.